INSTITUTO SUPERIOR TÉCNICO
Universidade Técnica de Lisboa

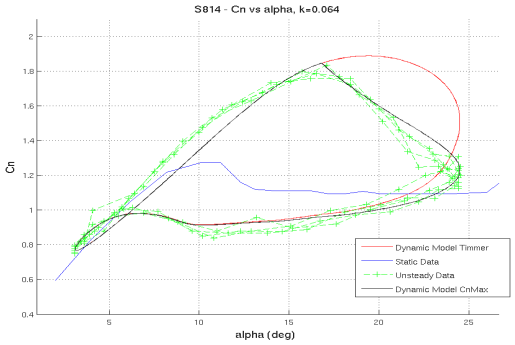

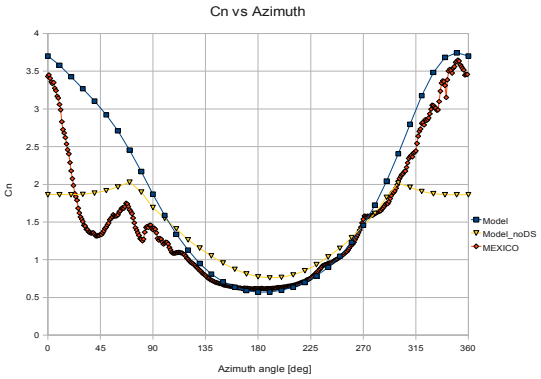

Validating the Beddoes-Leishman Dynamic Stall Model in the Horizontal Axis Wind Turbine Environment

Ricardo Balbino dos Santos Pereira

Master Thesis on

Aerospace Engineering

Jury

President: Prof. Fernando José Parracho Lau

Supervisor: Prof. João Manuel Melo de Sousa

Examiner: Prof. Luís Rego da Cunha de Eça

September 2010

Acknowledgements

I am sincerely grateful to everyone who made this master thesis possible. My formation as an engineering student started almost eight years ago at Lisbon's Instituto Superior Técnico. I have learned so much in this university , and I have many fond memories from the good teachers and colleagues I have had.

In 2007 I went to the Netherlands, to study at the TUDelft. This was a great experience, which gave me a different perspective and the opportunity to learn a lot about wind energy engineering. Also, I was lucky enough to do my internship at the Energy Center of the Netherlands. This institute does research in wind energy, which allowed me to get in contact with scientists who work in this field for decades. I am especially thankful to my internship supervisor, Ir. Gerard Schepers, for his insightful advise and fruitful discussions.

I must also thank my master thesis coordinator, Prof. João Melo de Sousa, for allowing me to be his graduation student and for the help and good advice he gave me. Also, he was my Aerodynamics professor and contributed to my decision of studying this difficult but very interesting field of science.

Last, but definitely not least, I must thank my family and friends for their everlasting patience and support.

Abstract

Keywords: Horizontal Axis Wind Turbine, Dynamic Stall, Beddoes-Leishman, MEXICO

Less expensive design solutions are sought in the wind energy industry, nevertheless any structure that is put forward must be robust. The dynamic stall (DS) phenomenon imposes large amplitude loading on airfoil sections and since it occurs in horizontal axis wind turbine (HAWT) operating envelope, accurate load prediction when DS is present becomes essential. The European Union developed a project named MEXICO, providing a database of aerodynamic data for a HAWT.

The aim of this master thesis was to choose and implement a DS model and to compare it with the MEXICO data obtained at high wind speeds in the presence of yaw misalignment.

It was chosen to implement the DS model in a Blade-Element Momentum (BEM) code, and consequentially two BEM approaches were compared with MEXICO data obtained at moderately high wind speeds.

Posteriorly the Beddoes-Leishman DS model was tailored to the HAWT environment, and validated against unsteady airfoil wind tunnel data. Different leading edge stall criteria were tested and good agreement was found. The rotational augmentation of the aerodynamic coefficients was also investigated using an inverse BEM method and empirical rotational corrections have been applied.

Finally the rotational corrections and the DS model were implemented in the BEM code, and the results were compared with high wind speed yawed flow MEXICO data. Reasonable to good agreement was found, and it was clear that including the dynamic stall model improved the computational results. The experimental trends observed were not always captured by the model, but the magnitude of the loads occurring over a revolution was well predicted.

For future research it is suggested to test the performance of other DS models, as well as to validate these models under higher excitation frequencies.

Resumo

Palavras-chave: turbina eólica de eixo horizontal, perda dinâmica, Beddoes-Leishman, MEXICO

A indústria de Energia Eólica procura designs menos dispendiosos, no entanto a integridade estrutural das turbinas eólicas deve necessariamente ser assegurada. A perda dinâmica (DS) é um fenómeno que provoca grandes amplitudes no carregamento a que um perfil alar está sujeito, e dado que ocorre frequentemente em turbinas eólicas de eixo horizontal (HAWT), é essencial prever com precisão o impacto deste fenómeno. A União Europeia desenvolveu um projecto denominado MEXICO, no âmbito do qual foi criada uma extensa base de dados duma HAWT.

O objectivo desta tese de mestrado foi seleccionar e implementar um modelo de DS, e compará-lo com os resultados experimentais do MEXICO obtidos a velocidades de vento elevadas e com a HAWT desalinhada.

Optou-se por conjugar o modelo de DS com a modelação *Blade-Element Momentum* (BEM), tendo sido validados dois códigos BEM utilizando dados do MEXICO obtidos a velocidades de vento moderadas.

Posteriormente o modelo de DS Beddoes-Leishman foi adaptado ao ambiente das HAWT e validado utilizando dados experimentais de perfis aerodinâmicos em regime não-estacionário. Foram testados dois critérios de perda de bordo de ataque, tendo-se obtido bons resultados. A influência que a rotação das pás tem na característica dos coeficientes aerodinâmicos dos perfis alares foi também investigada utilizando um método de BEM invertido.

Finalmente as correcções devidas à rotação das pás e o modelo de DS foram implementados no código BEM, e utilizaram-se para comparação os dados experimentais do MEXICO a velocidades de vento elevados e com a HAWT desalinhada. A concordância obtida entre os resultados do modelo e os dados experimentais foi razoavelmente boa, e a inclusão do modelo de DS melhorou os resultados computacionais. Embora os resultados do modelo não tenham correspondido aos dados experimentais em todas as posições azimutais, a magnitude do carregamento a que as secções da pá estão sujeitas numa revolução foi calculada correctamente.

Sugere-se para futuras investigações que outros modelos de DS sejam implementados, e também que estes modelos sejam validados a frequências de excitação mais elevadas.

List of Symbols

A - Area swept by the rotor [m2]

$A_{1,2}$ - Function used in the induced velocities empirical model [-]

$A_{1,2}$ - Constants used in the empirical approximation to the indicial response [-]

B - Number of blades [-]

C_d - Drag force coefficient [-]

C_l - Lift force coefficient [-]

C_N - Normal force coefficient [-]

C_{N0} - Normal force coefficient at an angle of attack of 0 deg [-]

C_N^f - Normal force coefficient including the pressure lag and viscous lag [-]

C_{N_α} - Derivative of the normal force coefficient with respect to the angle of attack [/deg]

$C_N^{'}$ - Normal force coefficient including the pressure lag [-]

$C_{N,I}$ - Critical normal force coefficient [-]

C_N^V - Vortex contribution to the normal coefficient [-]

C_P - Pressure coefficient [-]

C_T - Thrust coefficient [-]

C_{tg} - Tangential force coefficient [-]

C_V - Vortex lift [-]

D - Rotor diameter [m]

D - Deficiency function used in the Beddoes-Leishman dynamic stall model [-]

F - Force [N]

F - Flow expansion function [-]

F_1 - Correction factor for tip-loss [-]

K - *W*ake shape function [-]

K_α - Non-circulatory factor [-]

P - Pressure [Pa]

$P_{1,2}$ - Function used in the induced velocities empirical model [-]

R - Radius of the rotor disk [m]

Re - Reynolds number [-]

S - Semi-chords of an airfoil [-]

T_I - Non-circulatory time constant [-]

T_P - Pressure lag time constant [-]

T_f - Viscous lag time constant [-]

T_v - Vortex lag time constant [-]

T_{vl} - Vortex position time constant [-]

U - Wind speed [m/s]

V - Velocity [m/s]

X -Deficiency function used in the Beddoes-Leishman dynamic stall model [-]

Y - Deficiency function used in the Beddoes-Leishman dynamic stall model [-]

a - Axial induction factor [-]

a' - Tangential induction factor [-]

$b_{1,2}$ - Constants used in the empirical approximation to the indicial response [-]

c - Airfoil chord [m]

f - Frequency [Hz]

f - Non-dimensional separation point [-]

f' - Non-dimensional separation point including the pressure lag [-]

f'' - Non-dimensional separation point including the pressure lag and the viscous lag [-]

g - Function of number of blades and tip loss ratio [-]

k - Reduced frequency [-]

r - Local radius [m]

t - Time [s]

t - Airfoil thickness [m]

u - Axial induced velocity [m/s]

Greek Symbols

α – angle of attack [deg]

α_f - Equivalent leading edge pressure angle of attack [deg]

β - Yaw-misalignment angle [deg]

ϕ - Inflow angle [deg]

θ - Pitch angle [deg]

ψ - Azimuth angle [deg]

μ - Fraction radius [-]

χ - Wake skew angle [deg]

λ – Tip speed ratio [-]

Δ – Increment in quantity [-]

τ_v - Non-dimensional vortex time parameter [-]

Ω - Rotor's angular velocity [rad/s] or [rpm]

ω - Frequency [rad/s]

Indices

C – Circulatory

Eff - Effective

I – Impulsive

OSC – Oscillation

Press – Pressure

P – Unsteady attached

Tot- Total

n – Time sample

p – Pitch

r – Rotating

sep - Separation

visc – Viscous

tw – Twist

Abbreviations

2D – Two dimensional

3D – Three dimensional

AOA – Angle of attack

BEM – Blade Element-Momentum

BL – Beddoes-Leishman

CFD – Computational Fluid Dynamics

DS – Dynamic stall

DNW – German Dutch wind tunnel

ECN – Energy Research Center of the Netherlands

FFA - Flygtekniska Forsoksanatalten (Swedish Aeronautical Research Institute)

HAWT – Horizontal axis wind turbine

LE – Leading edge

LLF – Large scale low speed facility

MEXICO - Model rotor experiments under controlled conditions

OSU – Ohio state university

PIV – Particle image velocimetry

RPM – Revolutions per minute

TE – Trailing edge

TSR - Tip-speed-ratio

List of Figures

List of Tables

Table of Contents

1) Introduction

One can not deny the growing concern in decreasing the cost of energy in recent years, which has naturally also had an impact in the wind energy community. It is also true that it is common engineering practice to opt for conservative designs, which in the wind energy industry usually brings about heavier, more expensive rotor blades. In order to be able to push through cheaper, lighter structures it is necessary to ensure that such designs are able to withstand the loads expected to occur over the life time of a wind turbine.

One of the main requirements which must be met when certifying a wind turbine's structural integrity is that of fatigue damage resistance; a material's fatigue damage is especially related with the cyclic loading it is subjected to, and consequentially it is very important to accurately estimate the load variation a component will undertake.

For the same angle of attack range, the phenomenon of **dynamic stall** (DS) is characterized by imposing a very large load amplitude on the airfoil section, when compared to the static loading characteristic. This brings about significant hysteresis, which also affects the aerodynamic damping of a wind turbine. Since one expects dynamic stall to occur in wind turbine operation, especially when yaw misalignment is present at high wind speeds, it is clear that it is crucial to be able to predict the magnitude of the aerodynamic loads taking place when this phenomenon is present. In the last decades several models have been proposed to predict the aerodynamic loads occurring during DS in rotary wings, with a wide range of complexity and using distinct approaches.

The European Union developed a project with the main goal of providing a database of aerodynamic measurements of a horizontal axis wind turbine (HAWT), so that computational models could be validated. This project was named **MEXICO**, which stands for Model Rotor Experiments under Controlled Conditions. For this purpose, an extensively instrumented 4.5m diameter HAWT model was tested in December 2006 in the German-Dutch Wind Tunnel, under several flow conditions. The Energy Center of the Netherlands (ECN) was the coordinator of this project, even though several international entities participated, and the calculation rounds are still taking place.

1.1) Project Goals & Methodology

Based on a literature study conducted, the main goal of this master thesis is to **select a dynamic stall model** and to **assess the load predicting capabilities** of the method in a **real HAWT environment**. Data from the MEXICO project is especially suited to conduct a validation of the implemented model, and consequentially these measurements will be used to evaluate the performance of the model's predictions. It is thus also an objective of this master thesis to **process and analyse the MEXICO data**, namely the one used in the model's validation, to ensure that the comparison with the implemented model is trustworthy.

To assess the performance of the DS model, it was chosen to implement the model in a **Blade-Element Momentum** (BEM) code. Accordingly, it was necessary to firstly validate the BEM model in attached flow conditions. Posteriorly the DS model was tailored to the HAWT environment and validated against wind tunnel test

data from the Ohio State University (OSU) database. Finally the DS model was included in the BEM code so that a comparison with the MEXICO data could be carried out.

1.2) Report Layout

The body of this report is divided in 7 chapters. After this introduction, the theoretical background of the work carried out is given in **chapter 2**. The phenomenon of Dynamic Stall is addressed, explaining its relevance within the HAWT's environment, and the MEXICO experiment is also introduced. In **chapter 3** a preliminary analysis of the MEXICO data is carried out, with the objective of identifying possible incoherences in the pressure data. **Chapter 4** describes the implementation of two distinct BEM codes for yaw-misaligned HAWTs, and validates these models against MEXICO data obtained at moderately high wind tunnel speeds. In **chapter 5** the Beddoes-Leishman DS model is explained, and validated against wind tunnel test data from oscillating airfoils. The model is tailored for HAWT application with different leading edge (LE) stall criteria being assessed. **Chapter 6** discusses the influence of rotational augmentation on the static aerodynamic force coefficients; three dimensional (3D) corrections are implemented and compared with the MEXICO data using an inverse BEM method. In **chapter 7** the results obtained implementing the DS model and the rotational corrections in the BEM code are presented, and compared with the MEXICO data obtained at high wind tunnel speeds. Finally **chapter 8** states the most important conclusions drawn in this assignment and suggests topics of possible future investigation.

2) Theoretical Framework

Increasing concern in reducing the costs associated with energy production in recent years has naturally impacted the wind energy community, and consequentially cheaper design solutions are strived for. However, less expensive designs usually also mean lighter and less resistant structures, which nevertheless must be able to withstand the loads expected to occur over the life time of a wind turbine.

Fatigue resistance is a main requirement when certifying a wind turbine's structural integrity, and it is known that unsteady aerodynamic loading has a considerable impact on the total fatigue damage a wind turbine will undertake. It is thus clear that accurate unsteady aerodynamic load prediction is crucial if more cost-effective design solutions are to be achieved.

Usually the unsteady effects taking place in wind turbine aerodynamics can be divided in three "contributions"[1]:

1. **Dynamic inflow** is an inviscid effect on the induced velocity, and it is usually caused by a change in blade pitch angle or in rotor speed. It has a time scale in the order of D/U, where **D** stands for the diameter of the rotor and **U** represents the incoming wind velocity.
2. The **Theodorsen effect** is also of non-viscous nature, and it refers to the change on the airfoil characteristics while in fully attached flow conditions, namely the delay of the airloads with respect to the angle of attack when it varies rapidly. This effect has a time scale in the order of c/V_{Eff}, where **c** stands for the airfoil's chord and V_{Eff} represents the effective local velocity, which is the velocity the airfoil experiences.
3. **Dynamic stall** is a viscous effect on the airfoil characteristics at stalled conditions which is known to yield transient force coefficients of much larger magnitude than experienced in the static case. This effect involves a rather complex set of interlinked phenomena and it is also characterized by a time scale in the order of c/V_{Eff}.

In HAWT's normal operating regimes the **two time scales** of the unsteady effects mentioned above will have very **different orders of** magnitude, and consequentially, it is usual to study the effects of dynamic inflow and of the airfoil unsteady aerodynamics separately. One can also understand that, if dynamic stall is expected to occur, the Theodorsen effect must also be taken into consideration, since these phenomena are intrinsically related and describe the airfoil unsteady aerodynamics.

This chapter will start by **describing the dynamic stall phenomenon** and the several aspects which it is influenced by, together with an overview of some **"engineering" models** which have been developed, in section 2.1. Section 2.2 frames the occurrence of dynamic stall within the **HAWT environment** and normal operating envelope, from a qualitative point of view. Finally in section 2.3 the **MEXICO project** itself is addressed, by mentioning its **main characteristics** and relevant data for the present assignment.

2.1) The Dynamic Stall Phenomenon

When an airfoil undergoes a flow regime in which its angle of attack (AOA) changes rapidly the aerodynamic resulting forces and moments will differ from their static value, since obviously the flow regime and consequent pressure distribution do not adapt instantaneously.

As long as the flow remains attached and the airfoil is not very thick, the aerodynamic loading can be computed with the "elegant" Theodorsen's theory, which was developed considering a 2D oscillating flat plate. However, when the flow initiates separation, a complex set of interlinked phenomena occur, usually referred to as **dynamic stall .**.

Physical Description

If the airfoil experiences an oscillation in angle of attack in which it goes beyond the static stall angle DS may be present. This means that several subsequent different phenomena take place, with a fairly complex overall behaviour of the airfoil loading, yielding aerodynamic forces very different from those obtained in static conditions.

Dynamic stall is characterized by an accumulation of vorticity near the leading edge of the airfoil as the angle of attack is increasing, causing an overshoot in lift. This is followed by an abrupt decrease in the normal force when the built up vortex is convected downstream of the airfoil as the angle of attack is decreasing, together with very large pitching moment variations due to centre of pressure movements. To better grasp this sequence of events it is useful to divide the DS phenomenon in 5 stages, illustrated in the figure below from [2].

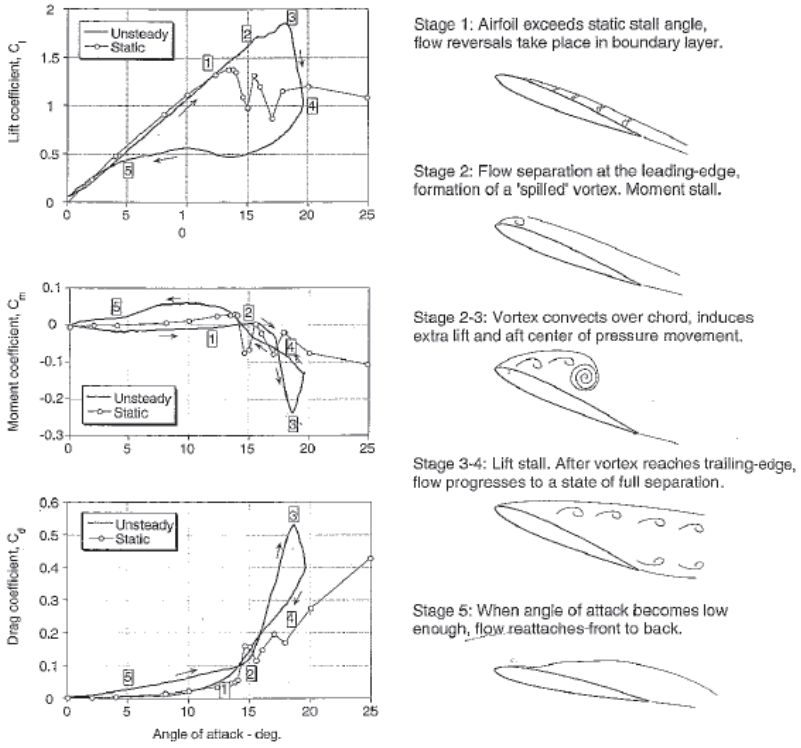

Figure 2.1 1: Dynamic Stall stages from [2]

As the value of angle of attack increases rapidly in **stage 1** there is a reduction in adverse pressure gradients along the chord, compared to what one would obtain in the quasi-steady case for the same angle of attack, and the onset of separation is delayed. Further augmenting the angle of attack, and as the separation point approaches the leading edge, there is a build up of vorticity in that region of the airfoil, which brings us to **stage 2**. At some point, the vortex disturbance will be cast off from the leading edge and swept downstream across the chord, which will cause an aft movement of the centre of pressure and consequently a very large nose-down pitching moment, usually referred to as **moment stall**. Still, as long as the vortex disturbance stays over the upper surface it will provide additional lift.

Stage 3 is characterized by a sudden break in the lift coefficient, which will take place at a higher angle of attack than the abrupt decrease in the pitching moment. That is to say, the moment stall will occur at the onset of vortex shedding, while the **lift stall** will happen only when the vortex passes into the wake.

The flow on the upper surface then becomes fully separated, as the vortex disturbance passes the trailing edge of the airfoil, which is common to designate by **stage 4**. Afterwards, the reattachment of the flow is significantly lagged, and full reattachment is postponed to configurations in which the airfoil is well below its normal static stall angle, as denoted by **stage 5**.

The concept of Reduced Frequency

Previously it was mentioned that dynamic effects can be noticeable in the aerodynamic loading when the angle of attack changes "rapidly", but how exactly can one quantify this? The response of an airfoil to changes in the local flow, as well as many other systems, is not solely dependent on the **frequency** of the excitation, ω. It is also related with the local **velocity,** V, and **chord,** c, since, obviously, the speed of propagation of a perturbation is finite. Thus, it is common to characterize the response of an airfoil undergoing oscillations by the **reduced frequency, k,** defined as

$$k = \frac{\omega c}{2V} \tag{2.1.1}$$

since this quantity is indeed representative of the system's dynamics. We should notice that the factor 2 in the expression above was introduced by historical reasons[1].

According to Leishman [2], one can consider that if **k<0.05** the problem is **quasi-steady,** i.e. the unsteady effects are generally small and can be neglected; if a problem is characterized by a reduced frequency **k> 0.05** it is considered **unsteady**, and the unsteady terms in the equations cannot be neglected if a realistic analysis is to be conducted. Moreover, if we have **k>0.2**, the unsteady terms will begin to dominate the behaviour of the airloads, and consequentially the problem is highly unsteady.

Effect of forcing conditions on Dynamic Stall

It is clear that dynamic stall involves a complex set of phenomena which may be extremely sensitive even to small perturbations, since turbulence and flow separation are most likely present, and so it is easy to understand that by changing the **forcing conditions** the aerodynamic loading may have large variations. A qualitative description of

[1] The original work of Theodorsen on airfoil unsteady aerodynamics used the profile's semi-chord as length scale, and subsequently nearly all investigation conducted in the same topic adopted his convention

what changes can be expected in the airloads when different forcing parameters are varied will be given now as:

- **Mean angle of attack ,** $\bar{\alpha}$ **-** when considering an oscillating airfoil, and assuming the other parameters remain constant, the mean AOA of the periodic motion can dictate the degree of stall penetration in a cycle. If the mean angle of attack is **small** (considerably smaller than the static stall angle), it is expected that the airfoil will undergo **"light"** dynamic stall, meaning that the $C_l \ vs \ \alpha$ curve will resemble the ellipses characteristic of attached flow, and that the oscillations of the moment coefficient, C_m will have a small amplitude. On the other hand, when the mean angle of attack of the oscillation is **large** (as large as the static stall angle or greater), one usually will encounter **"deep"** dynamic stall, where there will be a larger lift overshoot relatively to the static behaviour. In this case, it is also verified that a very significant nose-down pitching moment occurs, indicative of larger vortex shedding. However, the angle of attack at which the flow over the airfoil reattaches seems insensitive to changes in the mean angle of attack of the oscillation.

- **Reduced Frequency, k** – As mentioned before, the reduced frequency can be interpreted as the degree of unsteadiness of an oscillation; it is thus easy to understand that as one **increases** the reduced frequency, the system will have "less time" to adapt to the changes, or in other words, it takes longer until it "becomes aware" of the changes in angle of attack, and thus the **vortex shedding** is **delayed**, as well as the reattachment. By further increasing the reduced frequency, it is even possible to prevent flow separation from initiating in any point of the cycle, according to [2].

- **Mach Number, M –** Analogously to what happens in the static case, the effects of **compressibility** cause the stall angle to be **decreased**, meaning that there will be more stall penetration and a larger amount of hysteresis in the whole cycle. If the free stream velocity is large enough that the local Mach number approaches the sound barrier, dynamic stall onset may involve a shock wave, and there will be complex centre of pressure movements.

3 Dimensional Effects on Dynamic Stall

The brief qualitative explanation of the features of the dynamic stall process given above, as well of most of the experimental data available, refers to oscillating airfoils, either pitching or heaving[2], tested on wind tunnels in 2D flows. However it is clear that real-life engineering situations are usually not completely described simply by considering 2 dimensions of a problem, and consequentially typical 3D situations will now be addressed:

- **Sweep** – If one imposes high sweep angles on a 2D airfoil on a steady regime the onset of stall will be delayed and the maximum lift coefficient will be larger than the one obtained at an aligned configuration, because of the favourable effects of the spanwise development of the boundary layer. However, according to [2], when pitch oscillations are imposed in a swept airfoil, it appears that the maximum **normal** force coefficient is **not increased** when compared with the unswept dynamic case. Still, it is clear that the sweep angle has an influence, since the dynamic stall lift is delayed to a higher angle of attack, and also since the lift curve shows less hysteresis, because it is narrower. Now minding the pitching **moment** behaviour, experiments [2] show that the moment stall occurs approximately at the same angle of attack, but that its **slope** is **smaller.** This is possible to understand if one admits that the shed vorticity will be convected in the direction of the flow, and thus it will take more time to reach the trailing edge since the local chord is at an

[2] A heaving airfoil by definition has a forcing normal cyclic velocity, and it is not pitching, thus there is a periodic angle of attack variation imposed on the airfoil. It is also referred to as "plunging".

angle with the flow, since the wing is swept.

- **Finite Wing** – Since all the wings are finite, there will necessarily be a vortex at the tip, with intensity comparable to the circulation of the wing sections in its vicinity. This concentrated vorticity induces a downward velocity on the wing's sections near the tip, thus decreasing the actual angle of attack they are operating at. According to [3], the influence of the finiteness of the wing does **not** greatly **affect** the **dynamics** of the stall occurring when angle of attack oscillations are imposed. The tip vortex will indeed have an influence on the more outboard wing sections, but it is identical to the one obtained when the mean angle of attack of the oscillation is decreased, which was discussed previously. We can thus expect a reduction in the average lift-curve-slope when moving outboard towards the tip, but this is a quasi-steady effect. However, when one is considering sections extremely close to the tip the results are less transient, which suggest that leading edge vortex shedding does not occur because the tip-vortex alone dominates the flow field.

Rotational Effects

Besides the 3D effects mentioned above, the fact that a blade is rotating will bring about noticeable changes, and since it is necessarily the case in helicopters and wind turbines, it is relevant to consider it.

Blade rotation will originate a centrifugal force which, together with the radial pressure gradient , provokes an outwards spanwise flow component. Because this velocity is in a rotating reference frame, there will be a Coriolis force which acts to accelerate the fluid from the leading edge to the trailing edge of the airfoil, thus postponing separation.

Because the separation is delayed to higher angles of attack, the maximum lift the airfoil will experience may be significantly increased, which is why this effect is usually termed as **rotational augmentation**. It has also been verified [4] that the amount of lift added depends on the value of the chord to radius ratio (**c**/**r**), thus increasing at the blade's root.

The effect described above, even though it necessarily implies movement since the blade is rotating, is usually regarded as steady phenomenon; when an **unsteady regime** is imposed in a rotationally augmented blade section, according to [5], [6] the average lift coefficient in a cycle is somewhat larger, but the hysteresis is of a smaller magnitude, when compared to the 2D case. A figure of this effect is shown below:

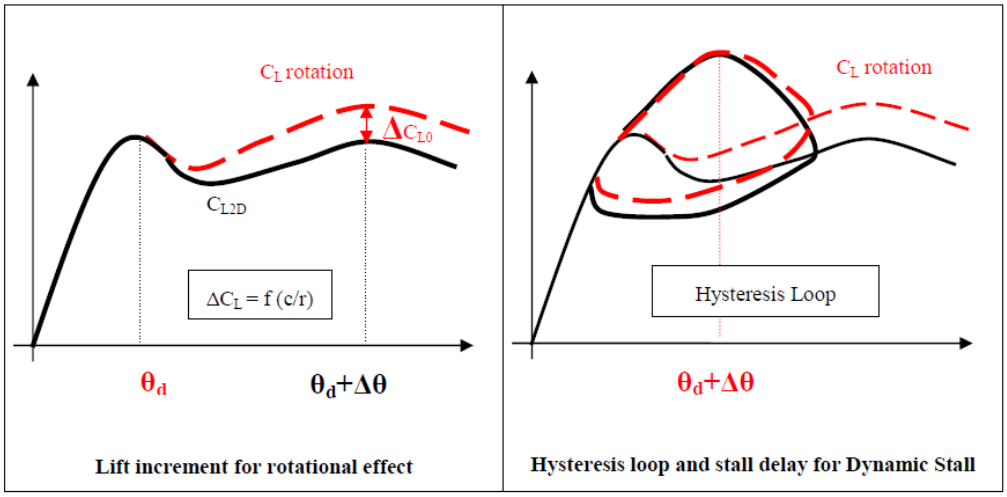

Figure 2.1 2: Classical rotational corrections from [6]

From the brief discussion above, it is clear that rotational effects play an important role in the blade sections where dynamic stall is expected to occur, and consequentially this matter will be posteriorly addressed in greater depth.

Modelling Dynamic Stall

From the explained above, it is obvious that dynamic stall encompasses a complex set of phenomena, and thus attempting to model its effects is not straight forward at all. Aerodynamicists, especially people involved in helicopter design and analysis have been working on this task since the 1960's, and currently the models that try to predict the effects of dynamic stall range from fairly simple empirical or semi-empirical models to complex computational fluid dynamics (CFD) methods.

Proper CFD simulation can only be obtained using the full Navier-Stokes equations with an adequate turbulence model, given the nature of the phenomena present in Dynamic stall; according to [7], [8], these models show some promise in predicting 2D and 3D dynamic stall events, however the quantitative predictions of the airloads are not yet satisfactory. Also because the computational resources for these CFD solutions are prohibitive, and will not be further addressed to in this assignment, we will now concentrate on more approximate models of the dynamic stall phenomenon.

Engineering Models

Some of the "Engineering Models" developed to predict the effects of dynamic stall are a form of resynthesis of the measured unsteady airfoil airloads, i.e. they simply try to "rebuild" the trends observed experimentally. On the other hand, the so-called "Semi-Empirical" models contain simplified representations of the physical processes taking place, by using sets of linear and non-linear equations to simulate the aerodynamic loads. Still, these models always require a significant number of empirical parameters, usually both from steady and unsteady experiments, and their application is limited to the airfoil and Mach number they were developed for. Some of these models will now be

considered:

- **UTRC α, A, B Method:** This is a resynthesis method developed around 1970, and its approach is described in [9], [10] ; It tries to isolate the dynamic contributions to the airloads by subtracting the static coefficients, and it has known some success, but it has the inconvenient that extensive data tables must be generated for each airfoil and Mach Number.
- **Boeing-Vertol 'gamma' Function Method:** In this method the influence of the airfoil motion is taken into account by computing an effective angle of attack The influence of the pitching and plunging effects is determined from the forcing conditions, and a second correction is applied from an empirical function dependent on airfoil and Mach Number. This final value is then used to obtain values from the static airload curves. This methods yields good predictions of the unsteady airloads, but it is not so accurate predicting situations with little stall penetration. More details are available in [11].
- **Time Delay Method:** This is a semi-empirical model developed in 1978, which is based in the time domain, and it is described in [12],[13]. This method actually tries to simulate, even though in a simplified manner, the basic physics of the dynamic process; the behaviour of the airloads in the attached flow regime are obtained using the Wagner indicial response function, and then two non-dimensional time delays are used, the first representing the delay in the onset of separation, and the second accounting for the time during which leading-edge vorticity shedding takes place. These time delays were obtained from a large amount of airfoil tests at different Mach numbers, and the method has given good predictions, and also has the advantage that it requires relatively few empirical coefficients.
- **Gangwani's Method:** It is a synthesized method, also time-based, where the airloads in attached flow are modelled in a very similar way as the time-delay method mentioned above. For the non-linear part of the model, a large set of equations with several empirical coefficients are used to represent the forces produced by the airflow. This model has shown credible predictions of the unsteady airloads, even though it seems to have some difficulties predicting flow reattachment. More details are available in [14].
- **Johnson's Method:** This is a fairly simple method, further developed in [15], where the static stall lift and pitching moment are corrected as a function of the pitch rate, and where vortex shedding is assumed to occur just above the static stall angle. In this model, vortex shedding produces increments in lift and nose-down pitching moments to a peak value, which then decay back to the static loads. This model yields reasonable predictions for the normal force coefficient, although less satisfactory estimates are obtained for the moment oscillations.
- **Leishman-Beddoes Method:** This method is capable of assessing the unsteady lift, pitching moment and drag, and it characterized by having a more complete physical representation of the unsteady aerodynamic problem, having been extensively validated with experimental data. It is comprised of **three subsystems**, namely, an **attached flow** model for the unsteady linear airloads, also referred to as the Theodorsen effect, a **separated flow model** for the non-linear airloads, and a **dynamic stall model** for the airloads induced by the leading edge vortex. The loads in the attached flow regime are obtained through indicial functions, where compressibility is taken into account; for the aerodynamic effects associated with separated flow, this method calculates an equivalent point of separation based on the angle of attack history, according to Kirchhoff/Helmholtz theory, which is then used to reconstruct the non linear loads; finally, to represent the

effects of dynamic stall, the dynamic effects of a concentrated leading-edge vortex passing across the upper surface and being convected downstream are taken into account. This method assumes that the **dynamic stall** process is **initiated** when an equivalent **leading-edge pressure** parameter reaches a critical value. This method yields indeed quite good results, and it has the important advantage that it requires relatively few empirical coefficients, most of which derived from static airfoil data, and this explains why it is so popular and has been extensively used in helicopter rotor loads prediction. It can be found in [16].

- **ONERA Method:** This model uses a set of nonlinear differential equations to describe the unsteady airfoil behaviour in both attached flow and during dynamic stall, and the coefficients in the equations are exclusively determined by comparison with experiments on oscillating airfoils. Being so, the later version of the model, described in [17], uses **18** empirical coefficients, and it also adapts the trailing-edge separation approach from Kirchhoff/Helmholtz theory. With this model one generally obtains reasonable predictions of the unsteady airloads, even though it behaves less satisfactorily predicting flow reattachment.

2.2) Dynamic Stall on Horizontal Axis Wind Turbines

In the current work aerodynamic data obtained from an instrumented wind turbine rotor model tested in a wind tunnel section will be analysed, and consequentially it becomes important to frame the occurrence of dynamic stall in the HAWT's envelope of normal operating regimes.

However, firstly it is necessary to describe the geometry convention normally used in wind engineering as far as airfoil aerodynamics is concerned.

HAWT Airfoil Aerodynamics

When in presence of a rotating blade it becomes easier to grasp the characteristic flow a local airfoil section is subjected to by considering the following representation :

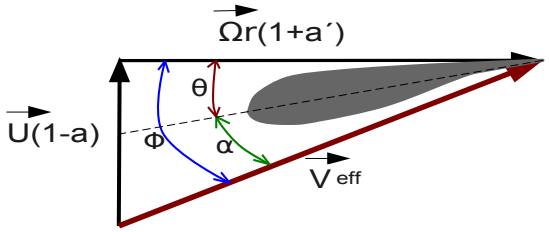

Figure 2.2 1: Rotating Blade Airfoil Section Convention

This sort of analysis is usually termed **blade element method**, and the entities represented in the figure above are thus:

- $\vec{U}$ is the incoming wind speed
- $\vec{\Omega}$ represents the blade's angular velocity
- $\vec{V}_{eff}$ is the effective velocity the airfoil experiences

- a is the axial induction factor
- a´ represents the tangential induction factor
- Φ is the inflow angle
- θ is the pitch angle
- α represents the angle of attack
- r is the radius of the considered section

In figure 2.2 1 one can see that the effective velocity the airfoil section is working at will have a component in the rotor plane[3] and in the direction orthogonal to the rotor plane. These velocity components are influenced respectively by the **tangential** induction factor , ***a'***, and **axial induction factor**, ***a***. These induction factors are introduced to compensate for the fact that the air stream is "aware" of the rotating blades before the rotor plane is reached, and consequentially the effective flow velocity at the rotor plane is substantially different from the unperturbed conditions.

Still minding figure 2.2 1 it is clear that **increasing wind speed** while keeping the angular velocity constant will **increase the angle of attack** the airfoil section is working at, since the incidence is proportional to the ratio of the wind speed to the angular velocity. From geometric considerations, one can see that the angle of attack is thus given by

$$\alpha = \phi - \theta = atan\left(\frac{U(1-a)}{\Omega r(1+a')}\right) - \theta \tag{2.2.1}$$

One should also notice that the pitch angle illustrated above refers to the **total pitch angl**e, which is a combination of both the **blade's local twist** and the **pitch angle** the blade is working at, according to

$$\theta = \theta_p + \theta_{tw} \tag{2.2.2}$$

Thorougher characterizations of typical wind turbine airfoil section aerodynamics can be found in wind engineering manuals, such as [18], together with expected trends for the induction factors as different wind turbine operating regimes are considered. Still, it is clear that these induction factors will have a large impact on the angle of attack experienced by the blade element, and thus may define whether DS phenomena are present in a given airfoil section. Consequentially, the determination of these factors will posteriorly be addressed in more depth.

Dynamic Stall occurrence

Almost every process occurring in a real wind turbine will have a dynamic nature; the wind is stochastic, and especially considering the trend to increase the size of wind turbine rotors, a **wind gust** may not be felt evenly throughout the rotor; since the blades are spinning, this wind speed spatial gradient will obviously cause a **local angle of attack variation**.

[3] Following common practice in wind engineering literature, in this report the expression "rotor plane" refers to the plane perpendicular to the HAWT's axis. Moreover, since the blades of the MEXICO rotor had no cone angle and no pre-bend, this designation leaves no room for ambiguity.

Also, and again minding the very **large size of modern wind turbines**, simply considering the atmospheric boundary layer, there will be angle of attack variations over a complete rotation, between the lower and higher azimuthal positions due to **wind shear**.

One should also keep in mind that in recent years attempts to **actively control tower and blade vibrations** has led to very **large pitch velocities** of up to 20 °/s, according to [19], which obviously may also bring about unsteady airfoil aerodynamic effects

However, and more importantly, a rotor **yaw-misalignment,** frequently present in real life operating regimes, can yield very significant cyclic angle of attack variations, and is often the main "responsible" for the occurrence of DS phenomena. It is also a configuration which can be easily simulated in a wind tunnel, and for which experimental results are available and will be used for comparison, and so we will concentrate on it further in the next section. It is noted that such measurements are done at a constant and known yaw angle where the tunnel flow is without turbulence and wind shear, which makes the excitation precisely known, opposite to the situation in the field.

From the considered above, one can thus see it is interesting and useful to study the problem of dynamic stall and to consider it in the Wind Turbine framework.

Wind Turbine in Yawed Flow

To gain a greater understanding of the problem at hand it is firstly necessary to define the **working reference frame**, and the **geometric parameters** which are important when a HAWT is operating under yawed conditions. The convention shown in the figure below will be adopted throughout the whole text:

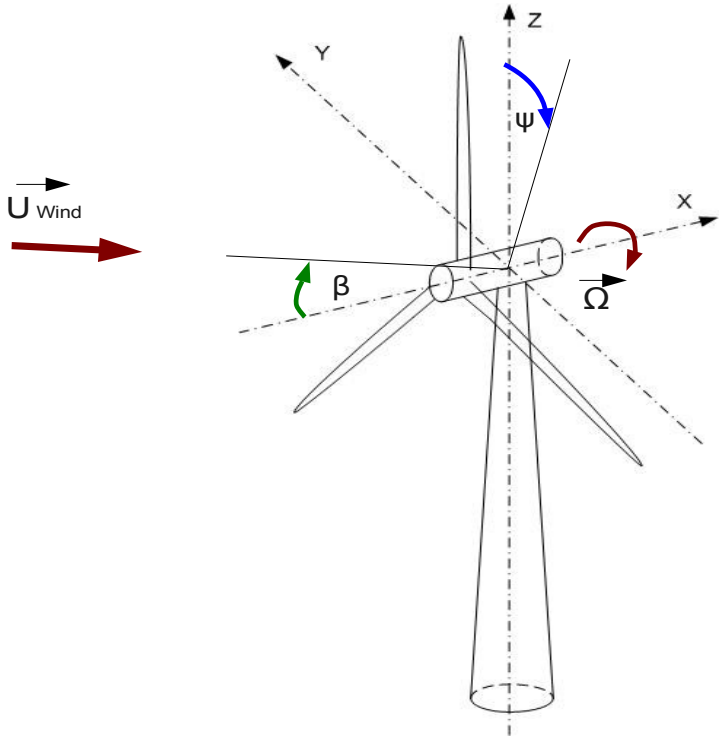

Figure 2.2 2: Convention for a Wind Turbine in Yaw

In figure 2.2 2 the following variables are represented:

- ***X*** is the axis perpendicular to the rotor plane, and pointing in the downstream direction.
- ***Y*** is the horizontal axis in the rotor plane, and is defined such that the third axis of the right hand Cartesian reference frame is pointing vertically upwards.
- ***Z*** is the vertical axis in the rotor plane, considered to be positive in the vertically upward direction.
- Ψ is the **blade azimuth angle**, measured from the vertical upward position, and in clockwise manner, when looking in line with the wind.
- β is the **yaw angle**, i.e. the angle the incoming wind is at with the vector normal to the rotor plane, assume to be positive if, when seen from upstream, the wind blows from the left-hand side.
- $\vec{U}_{Wind}$ is the incoming wind speed, assumed in this case to have no vertical component.
- $\vec{\Omega}$ is the angular velocity, which vector in this case coincides with the ***X*** axis.

It is not straight-forward to predict the loads a wind turbine blade will experience over a whole revolution when it is yawed, but according to [20] it is possible to identify two more or less distinct characteristic phenomena:

1. The so-called **Advancing/Retreating Blade Effect** can be understood simply from considering the geometry of the problem; if the wind is not blowing perpendicular to the rotor plane, we will necessarily have an extra in-plane velocity component, which will be even throughout the rotor plane. However this component will have a positive/negative contribution to the total in-plane velocity when the rotor blades are in the downward/upward position, depending on the convention. Taking figure 2.2 2 as reference, if $\beta > 0$, we will have a minimum in-plane velocity, and thus a maximum angle of attack, at the vertically upward position, i.e. $\Psi = 0^{o}$, and a maximum in-plane velocity and thus a minimum angle of attack at the vertically downward position, i.e. $\Psi = 180^{o}$. The expression to quantify the inflow angle as a function of the azimuth angle, keeping the convention defined above, is given by

$$\phi = atan\left(\frac{[U_{Wind}\cos(\beta)](1-a)}{[\Omega r - U_{Wind}\sin(\beta)\cos(\psi)](1+a')}\right) \qquad (2.2.3)$$

   Considering the expression above, and also minding that the axial induction factor's magnitude decreases with decreasing tip-speed-ratio [18], it is also understandable that **this effect is mainly 'felt' at high wind speeds and low tip-speed-ratios**[4]. This means that at these conditions the angle of attack becomes large, and so one often encounters dynamic stall phenomena. Being so, it is clear that the load variation from the advancing/retreating blade effect is very important for accurately predicting the damping characteristics and fatigue loads of wind turbine blades.

2. The fact that the wake is not being convected perpendicularly to the rotor's plane brings about an azimuthal variation of the induced velocities and consequentially of the aerodynamic loads, which is usually referred to as the **Skewed Wake Effect**. A correct prediction of this type of loads is very important, not only for fatigue

[4] The tip-speed-ratio (TSR) characterizes the regime the wind turbine is working at, and it is given by the ratio between the velocity due to blade rotation at the tip and the undisturbed wind speed, TSR=ΩR/U

calculation but also because this effect induces a load unbalance between the 'upwind' and 'downwind' side of the turbine, and thus causes yawing moments. Naturally, it is desirable that the overall yawing moment tends to align the turbine with the incoming wind, and thus has stabilizing character.

It is easy to understand that **this effect is mostly relevant when there are large induced velocities**, which happens when the wind turbine is working at relatively **high tip speed ratios and low wind speeds**. It is also important to mention that this effect yields more complex load variations over the rotor plane than the advancing-retreating blade effect, since usually the induced velocities greatly change both with the azimuthal position and with the radial station. For example, again taking the convention of figure 2.2 2 and assuming $\beta > 0$, the downwind side of the turbine would be for $\Psi \in [0,180]$, and the upwind side would correspond to $\Psi \in [180,360]$, and at the spanwise positions **near the tip** the influence of the convected tip vortices would be greater at the downwind side of the rotor than at the upwind side. This means that at $\Psi = 90º$ the induced velocity would be larger than at $\Psi = 180º$, and thus the local angle of attack will be greater at the upwind side of the rotor than at the downwind side. However, for spanwise positions **near the root** it is the root vorticity which has a greater influence on the induced velocities, and so we have the opposite trend, that is, at the downwind side of the rotor plane the angles of attack are larger than at the upwind side.

Reduced frequencies of operation

Based on the previously introduced concept of reduced frequency, it is now possible to have an idea of the **unsteadiness of the flow** one may encounter in a **yaw-misaligned wind turbine**.

Naturally, one expects that the flow in a given rotating blade section will have a periodic behaviour over time, with identical characteristics obtained for similar azimuthal positions. In other words, this means that one can assume that the **frequency of excitation** of this problem matches the **angular frequency** of the blade's rotation, which is usually also termed **1P** .

Now noticing that the incoming wind speed is of small magnitude when compared to the rotational speed, one can assume that the **magnitude of the local effective velocity** a blade element will experience is given by the **in-plane velocity component**.

Introducing these two approximations in (2.1.1), we come to:

$$k \approx \frac{\Omega c}{2\Omega r} = \frac{c}{2\mathrm{r}} \tag{2.2.4}$$

In the expression above, as in the influence of rotational effects, one can see again the term of the local **chord to radius ratio**, which is usually also termed **local solidity**. According to [21], typical values of the discussed variables found in wind turbine blades are:

r/R	c/r	k (1P)
0.3	0.25	0.12
0.5	0.15	0.075
0.75	0.07	0.035

Table 2.2.1- Typical reduced frequencies found in wind turbine's operation

It should also be mentioned that, in wind engineering it is common to consider the unsteady effects of an excitation if it is expected to have a reduced frequency greater than **0.02** ; this threshold is somewhat smaller than the value indicated by Leishman, but wind tunnel experiments with pitch oscillating airfoils show some hysteresis even when such low frequency excitations are imposed, also according to Snel [21].

Modelling Dynamic Stall in Wind Turbines

The dynamic stall models addressed before were developed mostly with the intention of being used in the prediction of aerodynamic loads present during dynamic stall phenomena occurring in **helicopters**, namely, during forward flight.

In a **wind turbine** the characteristic airflow may significantly differ, since the normal operating regime **Mach number** and **rotational frequency** will be considerably **lower**; moreover, the **airfoils** used in wind turbine blades are usually **thicker**. Consequentially specific dynamic stall engineering models "tuned" for wind turbines have been developed:

- **Øye Model:** In this method it is assumed that the motion of the separation point on the suction side of the airfoil can be computed with a simple-linear first order filter, and it uses this variable to introduce the dynamic effects under dynamic stall. This model defines 2 parameters, which do not vary with the airfoil, and requires two other profile dependent coefficients. Because of its simplicity and reasonable results this method has been popular, however it does not predict dynamic effects under attached conditions, and thus it yields less satisfactory results when there is little stall penetration. More information can be obtained in [22]

- **Larsen-Nielsen-Krenk Model:** This method combines memory delay effects under attached flow with reduced lift due to flow separation under dynamic stall conditions, and it is described in [19]. In this model only the lift coefficient is computed, and since it was developed specifically with Wind Turbine application in mind, it does some simplifications relatively to the previously mentioned models, like neglecting compressibility effects and including the non-circulatory effects as an added mass contribution. This model requires relatively few empirical coefficients deriving from unsteady experiments, and it is fairly simpler than other semi-empirical models, but according to [19] it performs at least equally better.

- **ECN Model:** This method computes solely the lift coefficient, and comparably with the ones previously mentioned, it is relatively simple to implement, as can be consulted in [21]. It accounts for the dynamic effects on the lift coefficient by adding two terms to the steady value, a **first order** part that describes the response to the excitation frequency, following that same frequency, and a **second order** part that is essentially nonlinear, allowing for self-excited force fluctuations, with a certain Strouhal number. This model is based on the need to reproduce the measurements and does not implement a criterion for the stall onset, requiring simply one non-steady empirical coefficient. The results obtained with this method are quite satisfactory, and the subsequent ECN investigations will unite it with the Theodorsen model in the rotating environment.

- **Sheng-Galbraith-Coton Model:** This is a very sophisticated method for Dynamic Stall Load prediction, specifically designed for low Mach Numbers, as elucidated in [23]. It is a modification of the Beddoes-Leishman model, including 3 relevant improvements, namely a **different stall-onset criterion**, new modelling from the **returned stalled state** and a new formula for the **chordwise force**. This model can be

considered complex and computationally heavier then the ones previously mentioned for wind turbine dynamic stall modelling, and it requires several empirical coefficients. However, it yields very accurate airload predictions for normal and chordwise forces and moment coefficients, especially when thin airfoils are analysed.

2.3) The MEXICO project

The MEXICO acronym stands for Model Rotor Experiments under Controlled Conditions, and it is a EU project with the main goal of providing a database of aerodynamic measurements. The project started in January 2001 and ended in December 2006. In this international effort an extensively instrumented 4.5 diameter HAWT model has been tested in the Large Scale Low Speed Facility (LLF) of the German Dutch Wind Tunnel (DNW), under several flow conditions. A figure of the experiment is given below:

Figure 2.3 1: The MEXICO experiment

Model Specifications

The wind turbine model was equipped with **148 pressure sensors**, distributed over 5 **spanwise sections** of

the blade, which had a **sampling frequency** of **5.5 kHz**. At the root of the blade, the edgewise and flatwise bending moments have been measured with **strain gauges**, and also **stereo Particle Image Velocimetry (PIV)** measurements have been made to measure the velocity field. The table below shows some of the main features of the wind turbine model:

ROTOR		
Rotation direction	**[-]**	Clockwise (facing the upwind part of the rotor)
Number of blades	**[-]**	3
Power regulation	**[-]**	Not present, speed control by motor/generator
Rotor speed	**[rpm]**	324.5 - 424.5
Swept area	**[m2]**	15.9
Rotor diameter	**[m]**	4.5
Hub height	**[m]**	5.49
Tilt angle	**[◦]**	0
BLADES		
Blade length	**[m]**	2.04
Cone angle	**[◦]**	0
Prebend	**[-]**	No prebend
Roughness	**[-]**	Zig-zag tape at 5% chord (0.25 mm thick, 10 mm wide, pressure and suction side)
Material	**[-]**	Aluminium 7075-T651 Alloy
TOWER		
Type	**[-]**	Tubular
Height including base	**[m]**	5.120
Diameter	**[m]**	0.508
Wall thickness	**[m]**	0.011
Roughness	**[-]**	Spiral flange to provoke transition
Material	**[-]**	Steel
PITCH SYSTEM		
Type	**[-]**	Linear actuator
Range	**[◦]**	[-5,90]

Table 2.3.1: MEXICO model main specifications

It should also be noted that the MEXICO blades are comprised of **three** different **airfoil sections**, a **DU 91-W2-250** in the **root** region, a **RISØA1-21** at **mid span** sections and a **NACA 64-418** nearing the **tip** of the blade. A figure of the airfoil distribution over the span is given below:

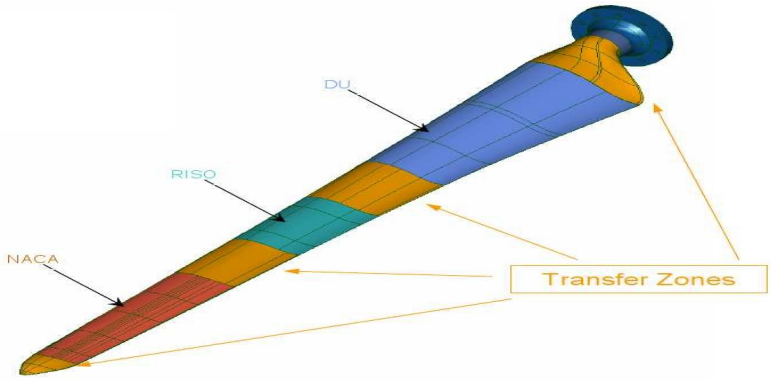

Figure 2.3 2: Airfoil section distribution over the MEXICO blades

The specific geometry of the MEXICO blade's airfoil sections is presented later in section 5.7. One should also mention that the spanwise sections instrumented with pressure sensors are located at relative radius of **25, 35, 60, 82** and **92%**, which was made with the intention of capturing the characteristic flow regions occurring in a wind turbine blade. For further information on the MEXICO model the reader is referred to [24].

Trial Cases

As mentioned before, several flow conditions were imposed on the model, both **steady** and **unsteady regimes**, namely axial flow, yawed flow, parked rotor, step in pitch angle and step in rotor speed. Some of the main characteristics of the regimes imposed are displayed in the table below:

Upstream Velocity [m/s]	[5; 30]
Yaw Angle [º]	{−30; 0; 15; 30; 45}
Rotor Speed [rpm]	{0; 324, 5; 424, 5}
Pitch Angle [º]	[−5, 3; 90]

Table 2.3.2 - Range of parameters considered in MEXICO trials

For further information on the MEXICO trials the reader is referred to [24] and [25].

3) Preliminary Analysis of MEXICO Pressure Data

One of the aims of the current thesis project is to take advantage of the very high sampling rate of the sensors in the MEXICO experiment and investigate dynamic effects occurring on the wind turbine's flow. As hinted previously, one will be namely interested in the MEXICO data points where a **yaw misalignment** is present, so that a posterior comparison with dynamic stall modelling can be conducted. Unfortunately, previous analysis on the MEXICO measurements by Pascal [26] and Micallef [27] indicated that the **pressure data** does **not** always seem to be **coherent**. Consequentially, and since one wishes to interpret the aerodynamic phenomena at dynamic, yawed flow, it seemed appropriate to start by analysing simpler cases, namely the MEXICO results obtained in **axial**, **steady flow**.

This chapter will start by indicating how the data from the MEXICO was processed, in section 3.1. Section 3.2 shows the experimental pressure distribution obtained for all spanwise stations, and finally conclusions are drawn on the MEXICO data's reliability in section 3.3.

3.1) Data Processing

This section will only consider the **pressure measurements** from the MEXICO experiment. The used pressure data corresponds to the '*Reduced Pressure Files*' and was taken from the MEXNEXT site [28]. The data in these files has already been **calibrated** for the **drift** in pressure sensors. and it represents the **gauge pressure**, i.e. the pressure measured with respect to the local atmospheric pressure. More information on the calibration procedure and on the data files themselves can be obtained in [26].

In this preliminary data analysis it was chosen to plot the **Pressure Coefficient**, C_p, and to compute this quantity the pressure registered by each sensor is divided by the maximum pressured measured over the airfoil, i.e.

$$C_p(i) = \frac{p(i)}{p_{max}} \tag{3.1.1}$$

One should notice that the denominator in the expression above should be the stagnation pressure, p_{stag}, and that $p_{stag} \geq p_{max}$. However, the leading edge area is heavily instrumented and consequentially this approximation should be enough to yield results where the main trends can be observed.

Once the pressure coefficient was calculated for each pressure sensor at each time instant, the results have been **averaged over the azimuth**, since in axial flow trials one expects very little azimuthal dependence. Each MEXICO trial lasted approximately 5 seconds, which means it includes approximately 27 revolutions for the low rotational speed case and 35 revolutions for the high rotational speed trials.

Finally, the pressure coefficient distribution over the airfoil's chord was plotted, for each of the instrumented spanwise sections of the MEXICO rotor blades.

Selected Data

With the intention of covering a wide range of flow conditions, it was chosen to plot the pressure coefficient distributions, at all spanwise stations, considering 6 different trials with distinct governing parameters. The selected trials were chosen to be representative of both low and high rotational speeds, at low, moderate and high wind tunnel velocities, and are displayed in the table below:

Trial Nr	Wind Speed (m/s)	Rotational Speed (r.p.m)	Pitch (deg)	Yaw Angle (deg)
84	7.5	324.5	- 2.3	0
63	15	324.5	- 2.3	0
78	24	324.5	- 2.3	0
92	10	424.5	- 2.3	0
99	15	424.5	- 2.3	0
135	24	424.5	- 4.3	0

Table 3.1.1 - Data points considered in the preliminary data analysis

A remark should be made that sensors **51** (25% span), **77** (60% span) and **111** (82% span), corresponding respectively to signals **53**, **74** and **110** have not been included in the plots, since, as indicated in [29], these were not properly functioning when the experiment was carried out.

3.2) Results and Discussion

The MEXICO data obtained for each of the spanwise positions are now shown and discussed, and the results at different rotational speeds are plotted in different figures.

25% Span

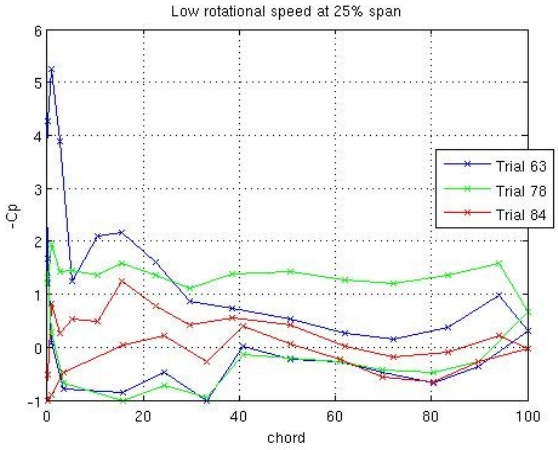

Figure 3.2 1: Cp distribution with chord in the low rotational speed cases (324.5 rpm) at the 25% spanwise station

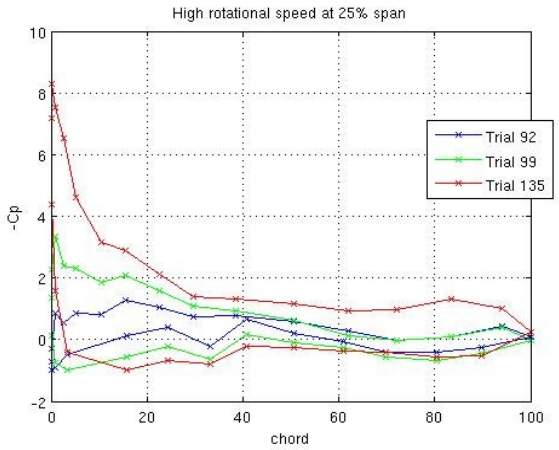

Figure 3.2 2: Cp distribution with chord in the high rotational speed cases (424.5 rpm) at the 25% spanwise station

Minding the figures above one can see that at this spanwise location the distribution of the pressure coefficient on the upper surface is somewhat odd, since unexpected peaks take place, especially when the low rotational speed case is considered.

At the highest rotational speed one can witness that the pressure distribution is more coherent; one also sees that this airfoil section will experience a larger lift coefficient at higher wind speeds, indicated by the greater gap between the upper and lower surface pressure distribution. This is to be expected since, as mentioned before, increasing wind speeds increase the local angle of attack.

Specifically regarding the lower surface pressure distribution it is possible to see that in every case the pressure sensor located around 35% of the chord seems to be off. In fact, the C_p curve in the lower surface follows the expected distribution, except for this pressure sensor where one can always observe kinks.

35% Span

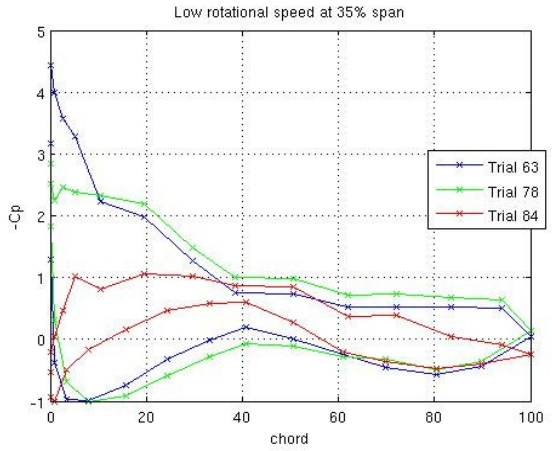

Figure 3.2 3: Cp distribution with chord in the low rotational speed cases (324.5 rpm) at the 35% spanwise station

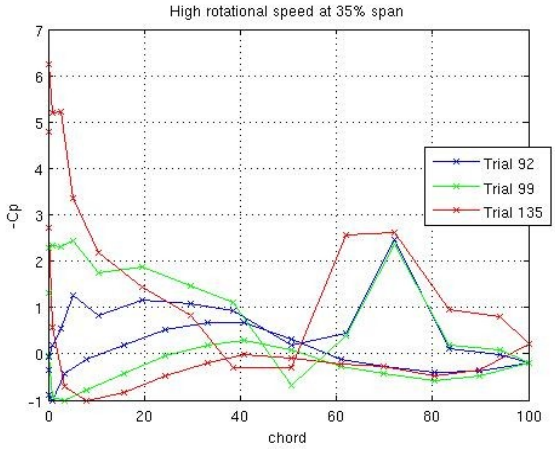

Figure 3.2 4: Cp distribution with chord in the high rotational speed cases (424.5 rpm) at the 35% spanwise station

From the figures above it is clear that for the 35% spanwise section the C_p chordwise distributions obtained at low rotational speed are coherent. As for the highest rotational speed cases, on the upper surface and approaching the trailing edge, the C_p distribution are very atypical. Unexpected large amplitude oscillations are observable, which are not attributable to common aerodynamic phenomenon. Consequentially one is led to believe that in these trials there was probably some kind of sensor malfunction in this region of the airfoil, as already indicated in [26].

One should notice that at high wind speeds, on the upper surface and near the leading edge there is often a small kink, locally decreasing the suction force, which can probably be related with the transition device placed at the 5% chord.

60% Span

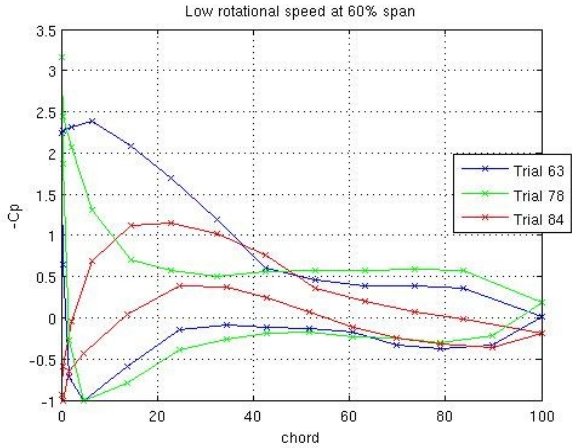

Figure 3.2 6: Cp distribution with chord in the low rotational speed cases (324.5 rpm) at the 60% spanwise station

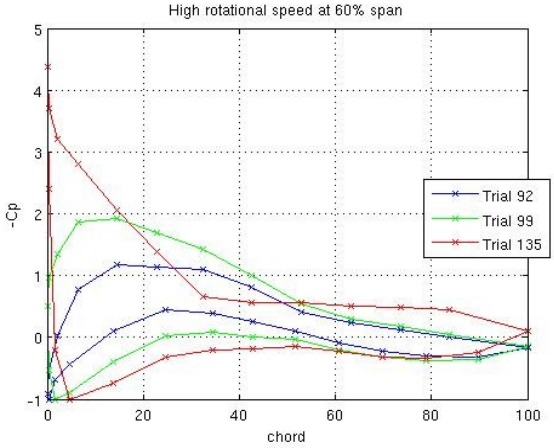

Figure 3.2 5: Cp distribution with chord in the high rotational speed cases (424.5 rpm) at the 60% spanwise station

In the figures above it is clear that for this spanwise section the distribution of the pressure coefficient over the chord follows the usual trends. Smooth curves were obtained, both for the upper and lower surface, and at both high and low rotational speeds.

One can clearly witness that as the wind speed (and hence angle of attack) increases the distance between the upper and lower surface's pressure coefficient increases as well, which means a larger normal force is produced. One can also see that for the highest wind speeds the pressure coefficient curve on the upper surface becomes constant near the trailing edge, which is indicative of stall.

82% Span

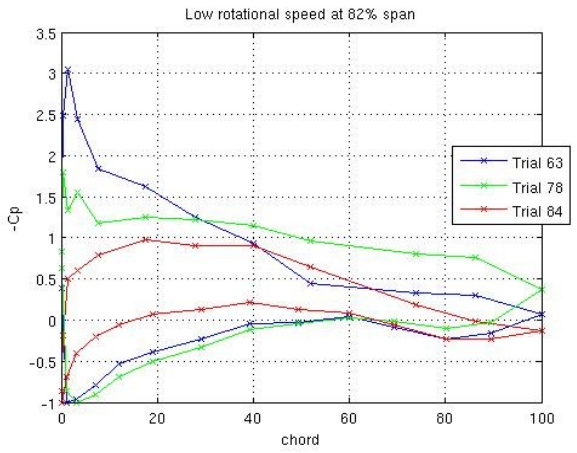

Figure 3.2 7: Cp distribution with chord in the low rotational speed cases (324.5 rpm) at the 82% spanwise station

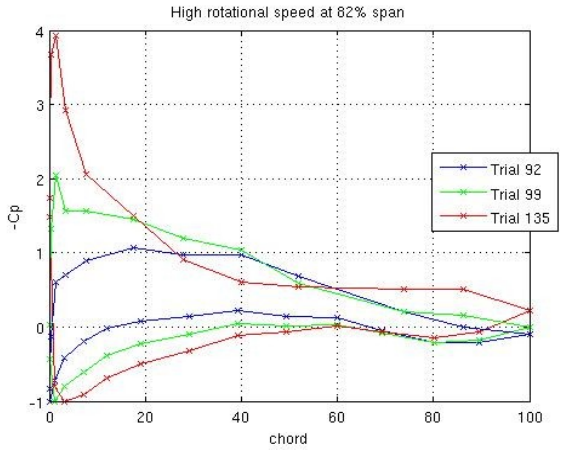

Figure 3.2 8: Cp distribution with chord in the high rotational speed cases (424.5 rpm) at the 82% spanwise station

At the 82% spanwise section all the pressure coefficient's distributions yield quite smooth curves, following the expected trends. Still, one can see a small localized suction drop near the leading edge in figure 23, probably caused by the transition device placed in that region.

92% Span

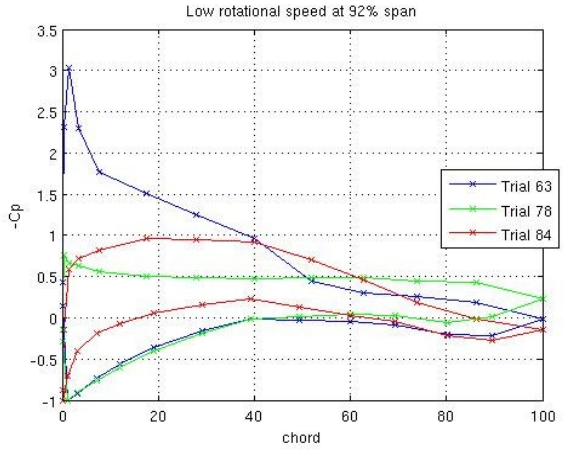

Figure 3.2 9: Cp distribution with chord in the low rotational speed cases (324.5 rpm) at the 92% spanwise station

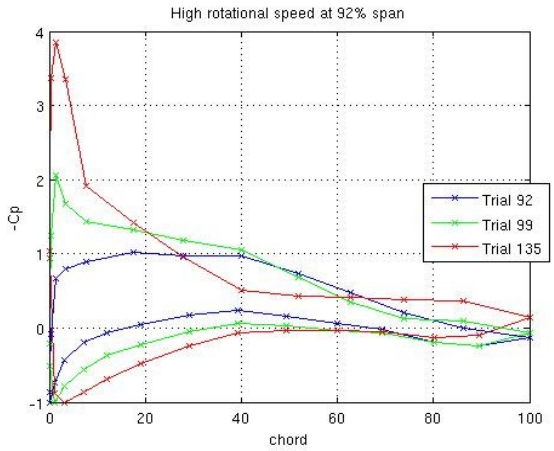

Figure 3.2 10: Cp distribution with chord in the high rotational speed cases (424.5 rpm) at the 92% spanwise station

As can be seen in the figures above, the distribution of the pressure coefficients at this radial coordinate is identical to what was found for the 82% span, with smooth curves and following the expected trends.

3.3) Conclusions and Recommendations

Analysing the data displayed above, one can conclude the following:

- For the **25% spanwise** station, the data often yields an unusual C_p distribution over the **upper surface** of the airfoil section. As for the pressure distribution obtained in the **lower surface** of the airfoil, one can see there is a pressure **sensor** yielding a 'kink' in all considered trials, located approximately at the 35% chord position. Consequentially it will **not be included** in posterior computations of the aerodynamic forces on the blade.
- For the **35% spanwise** station the **lower surface** pressure distribution seems to be according to what was expected. However, at the **upper surface**, near the trailing edge and for the high rotational speed cases there are very atypical peaks in the C_p distribution. These irregularities seem to indicate there was some sensor malfunctioning at this region of the airfoil. Having this in mind, and since at this radial stations the C_p distributions are often very odd, but not in every trial, it is recommended to **check the distribution** for any given trial. Only if smooth, 'regular' curves are obtained one should compute the aerodynamic forces.
- For the **60%**, **82%** and **92% spanwise** stations the distributions of the pressure coefficient are coherent and yield smooth curves, and thus, in principle, should be reliable to compute aerodynamic forces from.
- In some trials and for some spanwise sections, in the upper surface, it appears that the transition device may be causing a localized drop in suction.

4) Development and Validation of Blade Element-Momentum codes

A comparative study will now be performed between two distinct Blade Element-Momentum (BEM) codes and the pressure measurements from the MEXICO obtained at **yawed flow conditions**. One of the calculation methods is termed "**Classical BEM**" and is based on the algorithm suggested in [18]; it was mainly adapted from the previous work of Micallef et al. [30]. The other approach is referred to as "**Empirical BEM**" since it uses an empirical model for the axial induced velocities from Schepers et al.[31]. The objective of this chapter is thus to test these calculation methods so that posteriorly the DS model is included in the computation.

This chapter starts be giving a general description of the BEM method and justifying why it was used in this assignment. In section 4.3 both implemented BEM models are introduced, and in section 4.4 the MEXICO data used for the validation is addressed. The results obtained are then shown and discussed in section 4.5 and finally section 4.6 states the conclusions drawn.

4.1) The Blade Element-Momentum Method

A BEM approach is very often used for predicting aerodynamic loads on wind turbine blades. As hinted by its designation, this method combines both the **blade element** approach and the **balance of momentum** of the air inside the stream tube which contains the wind turbine's rotor.

This method assumes that there is no radial interaction between the flow through adjacent annuli, which is only true if the induction factor does not vary radially. Described simply, this approach states that the forces acting on the blades are responsible for the loss of momentum of the air which passes through the area swept by the rotor. To compute the airloads an iterative procedure is used, which is illustrated below:

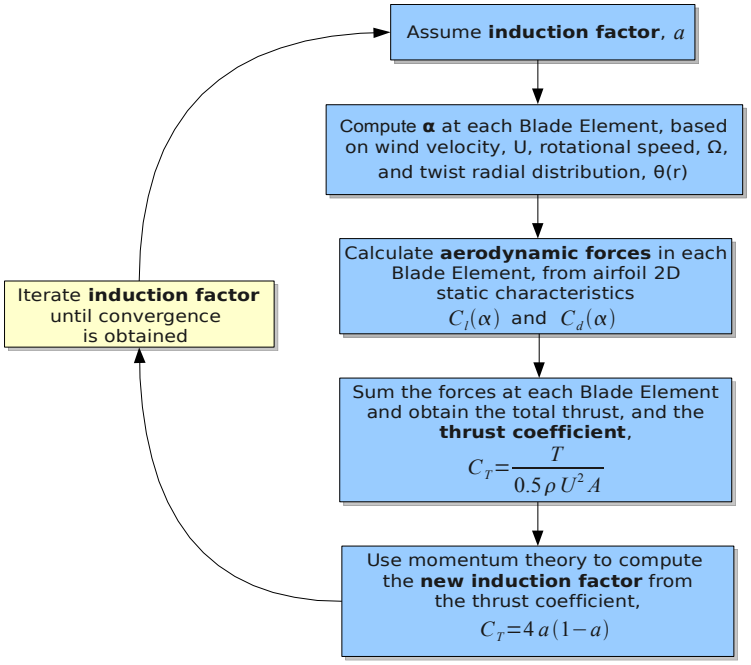

Figure 4.1 1: BEM method Calculation Procedure

One should bear in mind that only a very brief description of the BEM method was given above; much more detailed explanation can be found in several references of wind turbine aerodynamics, such as [18].

4.2) Why use the BEM method?

One of the main goals of this master thesis is to assess the performance of a DS model in the prediction of the loads wind turbines under yawed flow conditions will experience. As discussed before, usually semi-empirical dynamic stall models require the **angle of attack history** as an input, i.e., $C_l=f(\alpha)$ with $\alpha=f(t)$.

First of all it is necessary to understand exactly what 'angle of attack' signifies; traditionally the 'angle of attack' is defined as the angle which an airfoil's chord makes with the stream velocity. However, in the wind turbine environment the local velocity greatly varies when different rotor positions are considered, since the blades indeed "slow down" the incoming wind. The incidence angle at each spanwise section will thus depend on the local velocities at the rotor plane, and not directly on the stream velocity. Particularly in yawed conditions this fact makes the 'angle of attack' concept rather unclear.

Still, it is possible to compute the angle of attack at different spanwise stations and azimuthal positions of a wind turbine using both BEM and lifting-line codes. In his work, Micallef et al. [32] used an inverse free wake code to compute the local angles of attack throughout the rotor of the MEXICO. Inverse free wake codes use loads as input, and considering the influence of bound, shed and trailed vortices they compute, locally, what should be the bound circulation such that the Kutta-condition is met with. From this circulation, the angle of attack is then calculated, and

based on its method of computation, let us call this quantity the **'circulatory'** angle of attack.

However, DS models are generally based on wind tunnel measurements, where the angle of attack is usually taken as the angle the airfoil's chord is instantly at with the stream velocity. Based upon how it is defined, let us call this value the **'geometric'** angle of attack. The direction of the stream velocity is well defined in wind tunnel testing where most of the data used to derive the semi-empirical dynamic stall models was taken from, leaving no room for ambiguity.

Naturally, if there is some shed vorticity in wind tunnel tests, the local velocity at the airfoil will be influenced by it, and the bound circulation necessary to meet the Kutta condition will be associated with an instantaneous 'circulatory' angle of attack which is different from the usually taken 'geometric' angle of attack.

Thus it is understood that using the **angle of attack history**, α=f(t), computed with an **inverse free wake method**, as an input to DS models is **not expected to yield good predictions** of the aerodynamic loads, since we are indeed in presence of two different ways to tackle and simulate the problem at hands.

The DS model will posteriorly be implemented **inside** the BEM code. This allows the instantaneous loads to be calculated considering the angle of attack history, α=f(t), instead of using the static airfoil characteristics.

One should notice that BEM codes often incorporate a dynamic inflow model, which is introduced because the stream tube velocities do not adapt instantaneously to a change in blade loading. Such models act to damp the variation of the induction factors, and are normally used to improve the aerodynamic modelling performance when calculating unsteady loads arising from a step in the blade's pitch or rotor's angular speed. However such a model will not be introduced in the present implementation.

4.3) Description of the BEM models considered

The two Blade Element-Momentum models are now considered, and will be referred to as **'Classical BEM'** and **'Empirical BEM'**. Before addressing the models though, it is important to notice that both approaches prescribe a radial and azimuthal distribution for the **axial induced velocity**, ***u***. This quantity is assumed to be **positive** in the direction **opposite to the wind** speed, i.e. in -x direction defined in figure 2.2 2.

In case yaw-misalignment is present, this local axial induced velocity is given by:

$$u = U_{Wind}\cos(\beta)\,a \tag{4.3.1}$$

Classical BEM

This designation refers to the algorithm for BEM method code in the presence of yaw-misalignment suggested in [18], and was mainly adapted from the previous work of Micallef et al. [30].

This model assumes the axial induced velocity to be given by:

$$u = u_{avg}\left(1 + K(\chi)F(\mu)\sin(\psi)\right) \tag{4.3.2}$$

where:

- ***K*** is a function of the wake shape
- χ represents the wake skew angle
- ***F*** is a flow expansion function
- μ represents the fraction radius, $\frac{r}{R}$

This codes iterates the induction factors at each radial position by averaging over the azimuth, using vortex cylinder theory for the thrust forces, and computes both **azimuthally averaged axial** and **tangential induction** factors.

In this model the **flow expansion** is assumed to follow the simple model of Oye. The **tip** and **root loss** are taken into account using the Prandtl/Glauert correction, and the **wake rotation** is computed considering the influence of a single vortex being trailed from the centre of rotation. Once the azimuthally averaged inductions are computed this model calculates the load variations, and the azimuthal variations can be found by using the thrust and torque gradients. A more detailed description is given in [30] and [18].

Once the iterating procedure of the BEM method is finished, one wishes to derive the force coefficients in the direction **normal** and **tangential** to the **airfoil chord**, at each spanwise section. These quantities are required because one can thus compare the results directly with the MEXICO measurements. These coefficients are derived from the computed lift and drag coefficients, using also the calculated angles of attack, according to he system of equations:

$$\begin{aligned} C_n &= C_l . \cos(\alpha) + C_d . \sin(\alpha) \\ C_{tg} &= C_l . \sin(\alpha) - C_d . \cos(\alpha) \end{aligned} \tag{4.3.3}$$

Empirical BEM

Axial Induction Velocities

This method of computation uses the **empirical model** from Schepers et al. [31] of the **axially induced velocities** in a yawed flow wind turbine; it was derived from a wind tunnel experiment performed at TUDelft, where the velocity distribution was measured at several spanwise and azimuthal positions and fit with a second harmonic Fourier series. According to this model, the induced axial velocities are given by:

$$u = u_{avg}(1 - A_1 \cos(\psi - P_1) - A_2 \cos(2\psi - P_2)) \tag{4.3.4}$$

where A_1, A_2, P_1, P_2 are functions of the **relative radius**, of the **azimuth angle** and of the **empirically derived constants**.

It should be noted that this empirical model of the axial induction velocities was derived only for the **design condition** of the wind turbine, and that measurements only covered **spanwise** stations up to **80%.** For positions closer to the tip the results were simply extrapolated from the azimuthally averaged induction, which means that the tip-loss was not taken into account.

As explained in [31], this empirical model has been previously extensively validated, having been used to compute the expected yawing and flatwise moments in a yaw-misaligned wind turbine. Comparison with measurements has shown this empirical solution performs very often better than other models, and never worse.

'Empirical BEM' Implementation

Now regarding the BEM model implemented, the inplane velocities simply consider the skewed inflow, which can be derived from geometric considerations; this means that in this approach the **induced tangential velocities are neglected**. However it is not expected that this will greatly affect the force's calculation since the magnitude of the tangential induced velocities is very small when compared with the velocities due to the blade's rotation.

From the inplane and axial velocities, the angle of attack at each spanwise position is derived, and using static $C_l vs\,\alpha$ and $C_d vs\,\alpha$ functions, the forces on each blade element are calculated.

To account for the **tip loss effects**, this model uses the correction suggested by Shen et al. [33], which takes the form:

$$C_n^r = F_1 C_n \quad and \quad C_{tg}^r = F_1 C_{tg} \tag{4.3.5}$$

The correction factor is given by

$$F_1 = \frac{2}{\pi}\cos^{-1}\left[\exp\left(-g\frac{B(R-r)}{2R\sin\phi}\right)\right] \tag{4.3.6}$$

where ***g*** is an empirically derived function of the number of blades, ***B,*** and tip-speed ratio, λ, according to:

$$g = \exp\left|-0.125(B\lambda - 21)\right| + 0.1 \tag{4.3.7}$$

The total thrust is then obtained by integrating over the span and summing the contribution of all blades. Finally, the thrust coefficient in a yaw-misaligned configuration is computed with:

$$C_T = \frac{T}{0.5\rho.(U_{Wind}.\cos\beta)^2.A} \tag{4.3.8}$$

And the average axial induction coefficient is iterated using momentum theory according to:

$$C_T = 4a_{avg}(1 - a_{avg}) \tag{4.3.9}$$

Once the process converges, the **normal** and **tangential force coefficients** are computed in an identical way as in the 'Classical' BEM method.

Discretization Parameters

The same level of discretization was imposed in both BEM codes, so that a valid comparison could be performed. Following the recommendations from Micallef et al. [30], it was chosen to use **azimuthal increment of 10 degrees** and **15 elements in the spanwise direction**.

The convergence of the BEM code including the DS model will posteriorly be assessed.

4.4) MEXICO data used for validation

It is important to state that the BEM models will be validated against MEXICO measurements obtained at **relatively high wind speeds**; this is justified by the fact that at **low wind speeds** it is likely that the turbine is working in the turbulent wake state, which means that the trailed vortices will have a major influence in the flow field and consequentially in the observed loading. Bearing in mind that the goal is to use the BEM codes to simulate dynamic stall, which is expected to occur at high wind speeds, it is understandable that the validation at low wind speeds is not very relevant.

When **high wind speeds** are considered the airfoil is expected to stall, at least in some portion of the blades, and as discussed before this stall will have a dynamic nature. Since the BEM codes under consideration use static $C_l vs\, \alpha$ functions, it is not expectable that good agreement is found between calculations and measurements at these high wind speeds, and so it makes little sense to compare such results.

Finally, one should also keep in mind that at **high wind speeds**, i.e. at low tip speed ratios, the induction factors will have a smaller magnitude [18], which means that the advance/retreating blade effect will be dominant. As mentioned before, BEM codes iterate on the induction factors, but since these factors will have a smaller magnitude their contribution to the angle of attack 'seen' by the blade will also be small compared to the geometric effect. Consequentially the accurate computation of these induction factors becomes less important in the prediction of the unsteady loads the wind turbine blades will experience.

Minding the discussion above, the following data points will be considered in this validation:

Trial Nr	Wind Speed (m/s)	Rotational Speed (r.p.m)	Pitch Angle (deg)	Yaw Angle (deg)
158	15	424.5	-2.3	15
151	15	424.5	-2.3	30
165	15	424.5	-2.3	45
159	18	424.5	-2.3	15
152	18	424.5	-2.3	30
166	18	424.5	-2.3	45

Table 4.4.1 - MEXICO data points considered in the BEM codes' validation

Following the recommendations issued in the previous chapter, a preliminary visual inspection of the chordwise pressure distribution was conducted on the MEXICO data points, at all spanwise sections. The table below shows the outcome of this procedure:

Trial Nr	25% Span	35% Span	60% Span	82% Span	92% Span
158	Accepted	Accepted	Accepted	Accepted	Accepted
151	Accepted	Accepted	Accepted	Accepted	Accepted
165	Accepted	Accepted	Accepted	Accepted	Accepted
159	Accepted	Rejected	Accepted	Accepted	Accepted
152	Accepted	Rejected	Accepted	Accepted	Accepted
166	Accepted	Accepted	Accepted	Accepted	Accepted

Table 4.4.2: Preliminary analysis of the yawed flow trials

Derivation of the experimental aerodynamic coefficients

The aerodynamic force coefficients C_n and C_{tg} of the MEXICO will be plotted for comparison with the BEM methods implemented, and are taken as a reference to compute the associated error. Consequentially it is necessary to explain how the experimental coefficients were obtained from the MEXICO data.

A **cubic interpolation** of the **pressure** measured by each sensor was performed over the airfoil surface. This pressure distribution was integrated over a cubic interpolation of the airfoil surface, yielding the **normal** and **tangential forces**.

To obtain the force coefficients[5], the computed forces were divided by the maximum pressure occurring over the airfoil, taken as the **maximum of the cubic interpolation** of the pressure sensors, according to

$$C_{n,MEXICO} = \frac{F_{n,Interp}}{c.P_{max,Interp}} \quad and \quad C_{tg,MEXICO} = \frac{F_{tg,Interp}}{c.P_{max,Interp}} \tag{4.4.1}$$

Following this approach the computed force coefficients are expected to yield results which are accurate enough to compare models against.

Viscous Contribution

It should also be stated that simply by integrating the pressure distribution over the airfoil and considering the chordwise force component one is not computing the actual tangential force, since obviously there is also a viscous contribution.

When **small angles of attack** are considered, the tangential force coefficient will very approximately match the drag force coefficient. Consequentially one can have an idea of the viscous contribution to the tangential force by computing the difference between the total and pressure drag. According to [25], for the airfoil sections used in the MEXICO's blades and at similar Reynolds numbers, wind tunnel 2D tests show that:

[5] These are section force coefficients, i.e. per meter span, and thus the maximum pressure in the denominator should be multiplied by the local chord of the airfoil.

$$C_{d,Visc} = C_{d,Tot} - C_{d,Pres} < 0.01 \quad (4.4.2)$$

The magnitude of this contribution is not very large, but it is significant especially for the thinner airfoils where pressure drag is of less importance.

However if **large angles of attack** are imposed it is likely that some **flow separation** takes place. In this case one expects smaller boundary layer velocities, and consequentially reduced shear stresses to occur at the airfoil's surface. This means that the viscous contribution to the tangential force will not be significant when compared to the contribution of the pressure forces.

Since one is mainly interested in analysing large angle of attack situations, and also since it was not measured in the MEXICO and would be intricate to determine, the **viscous contribution** will **not be taken into account** in this assignment.

4.5) Results and Discussion

The **normal** and **tangential force coefficients'** variation with the **azimuth angle** will now be plotted, both from MEXICO data and using the BEM methods addressed. The wind tunnel speeds considered are **15** and **18 m/s**, at which one expects to encounter predominantly attached flow regimes.

The results obtained are shown for all spanwise stations, and considering a **yaw misalignment** of **30 degrees**.

25% Spanwise

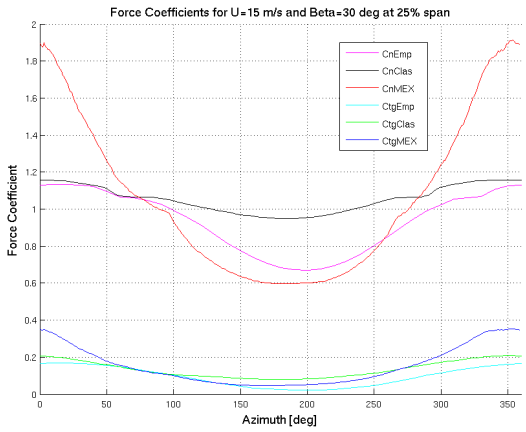

Figure 4.5 1: BEM models comparison for U=15 m/s at 25% spanwise station

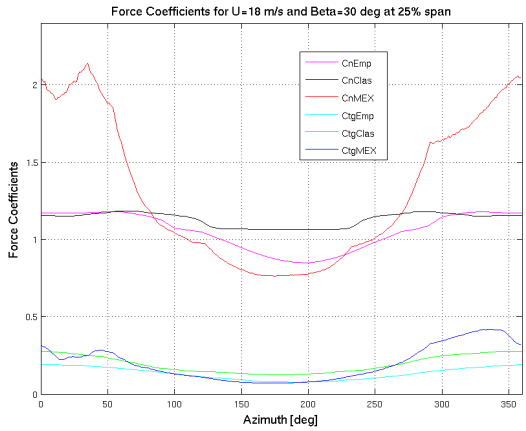

Figure 4.5 2: BEM models comparison for U=18 m/s at 25% spanwise station

Regarding the general variation of the experimental normal force coefficient with the azimuth angle, the figures above show that this quantity peaks at the 0 degrees position, and has a minimum at approximately 180 degrees. This variation is consistent with a strong **advance/retreating blade effect**, which was to be expected given the inboard position of the considered section.

Minding figures 4.5 1 and 4.5 5 one also notices that all force coefficients from experimental data have larger magnitudes in the larger wind tunnel speed case. This is not surprising since with increasing wind speed the angle of attack is expected to increase, and consequentially so does the magnitude of the aerodynamic loading.

Now addressing the implemented models' performance, it is clear that both BEM methods fail to predict the large experimental normal force coefficient values taking place at azimuth angles in the region of 0 degrees.

Because this is an inboard section, and given the geometry of the problem, at an azimuthal position of 0 degrees one expects the greatest values of local angles of attack to occur, according to [20]. Also because of its spanwise location strong rotational augmentation should be present, and separation is likely to be delayed. However, and as mentioned before, the implemented methods use **2D lift and drag coefficient** characteristics, and consequentially one understands that both models underpredict the actual aerodynamic loads at these azimuthal positions.

Specifically comparing the implemented models, results indicate that the empirical model captures the experimental trend better than the classical method. This is observable at azimuthal positions near 180 degrees, where one expects a smaller angle of attack and consequentially no rotational augmentation.

35% Spanwise

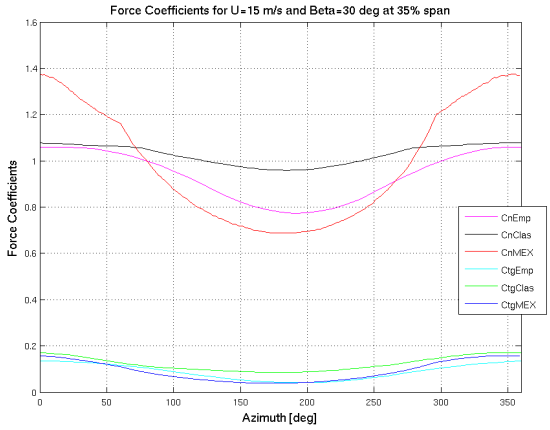

Figure 4.5 3: BEM models comparison for U=15 m/s at 35% spanwise station

Firstly it is necessary to mention that, according to table 4.4.2, at this spanwise station the data point with a wind tunnel speed of 18 m/s and a yaw-misalignment of 30 degrees was rejected, and so only the lower wind tunnel speed case is shown.

The figure above shows similarities with the results obtained at the 25% spanwise station. Rotational augmentation is expected to also be important in this section, and consequentially the magnitudes of the normal force coefficient are once again underpredicted by the implemented models.

Now comparing both computational approaches, the empirical BEM method seems to capture the aerodynamic loading trend better than the classical BEM model at this spanwise station. One may say this improved performance is observable both for the normal and tangential force coefficients.

60% Spanwise

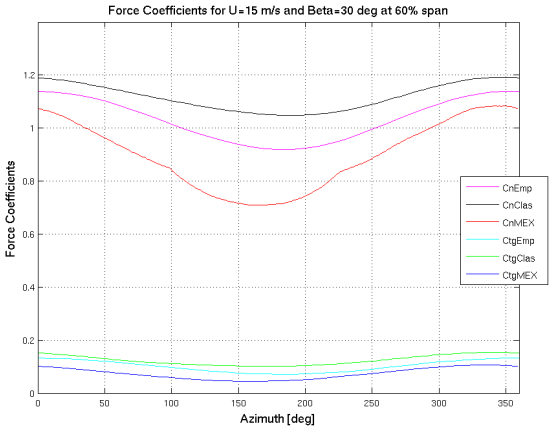

Figure 4.5 5: BEM models comparison for U=15 m/s at 60% spanwise station

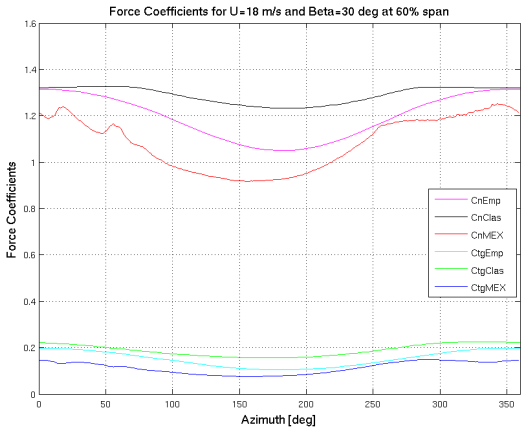

Figure 4.5 4: BEM models comparison for U=18 m/s at 60% spanwise station

At this spanwise section one expects very little rotational augmentation, and so one understands that the implemented models are able to predict the aerodynamic loading trends more accurately than at the inboard stations.

Comparing both methods of calculation the results from empirical BEM show better agreement with the MEXICO data; this can be seen at the two considered wind tunnel speeds and both for the tangential and normal force coefficients. As for the classical BEM method, it leads to a significant overprediction of the aerodynamic loading magnitude in the considered cases.

82% Spanwise

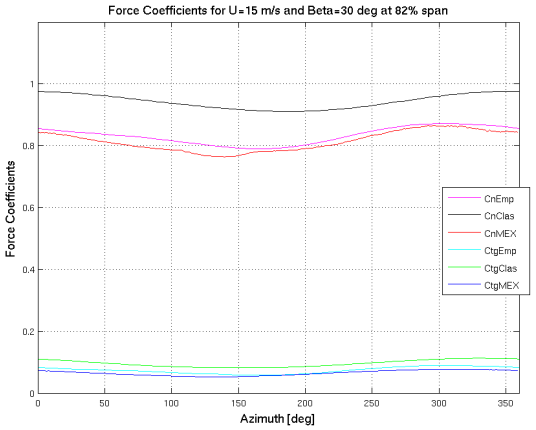

Figure 4.5 7: BEM models comparison for U=15 m/s at 82% spanwise station

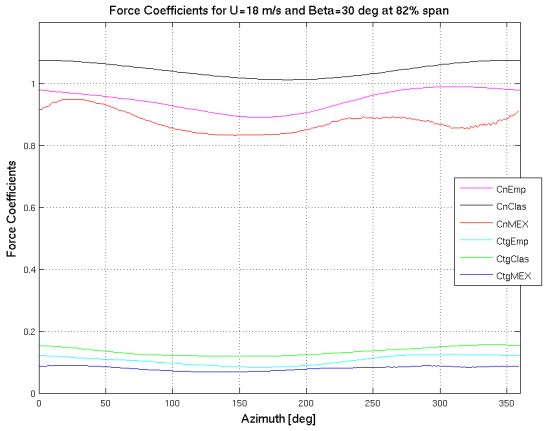

Figure 4.5 6: BEM models comparison for U=18 m/s at 82% spanwise station

At this spanwise station the normal force coefficient variation with azimuth angle is qualitatively different from the sections analysed up to this moment; specially at the lower wind speed case, one can notice that the minimum value of the normal force coefficient is shifted towards the 90 degrees position, and that the maximum is shifted towards 270 degrees azimuth. This behaviour can be understood since this is an outboard section of the blade, and

consequentially at low wind tunnel speeds the **skewed wake effect** will have a significant influence.

Regarding the implemented calculation methods, the results show that the empirical BEM model has a better agreement with the MEXICO data at the considered wind tunnel speeds and both for normal and tangential force coefficients. Similarly to the results from the 60% spanwise station, the classical BEM predicts significant larger magnitudes of the force coefficients than experimentally measured.

92% Spanwise

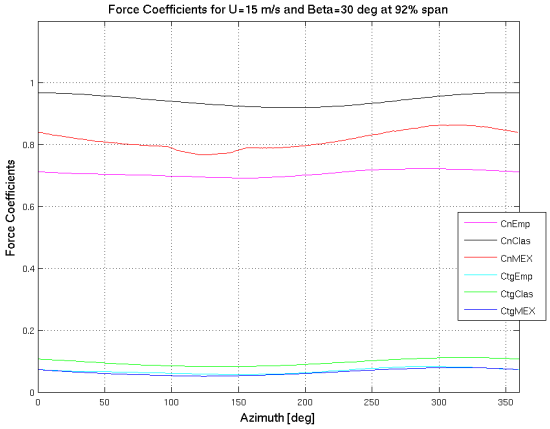

Figure 4.5 8: BEM models comparison for U=15 m/s at 92% spanwise station

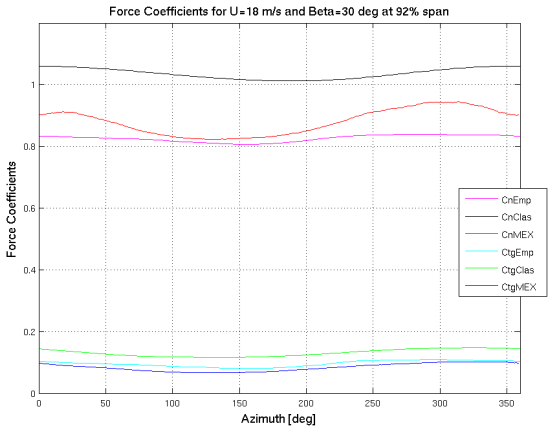

Figure 4.5 9: BEM models comparison for U=18 m/s at 92% spanwise station

The results show that at this spanwise position the variation of the experimental force coefficients with the azimuth angle is similar to what was obtained for the 82% spanwise position; this was expected since the skewed wake effect should also have a strong influence at the current spanwise coordinate.

Since this is the most outboard blade section which was instrumented in the MEXICO blades, one expects to tip-effects to be present. However, the tip-correction introduced in the empirical BEM model appears to be excessive, since the normal force coefficient values are underpredicted; still, this method performs at least equally as well as the classical BEM approach. For the latter model, and similarly to the other spanwise stations, overpredictions of the force coefficients were obtained in the considered data points.

Influence of the Yaw angle

All results shown before were obtained with a "representative" yaw-misalignment angle of 30 degrees. To assess the influence of this quantity, data points with **yaw angles of 15 and 45 degrees** are now analysed, considering a spanwise station of 60% and a wind tunnel speed of 18 m/s.

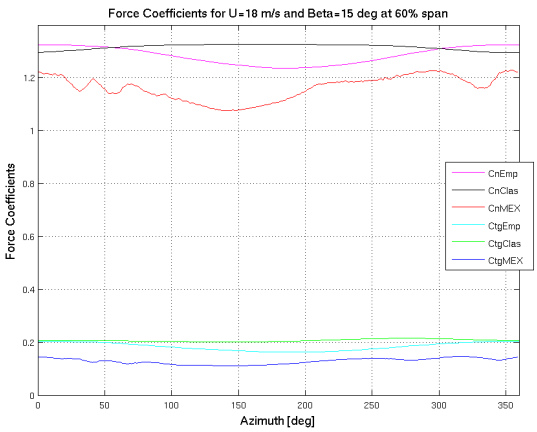

Figure 4.5 11: BEM models comparison for U=18 m/s at 60% spanwise station and yaw angle of 15 deg

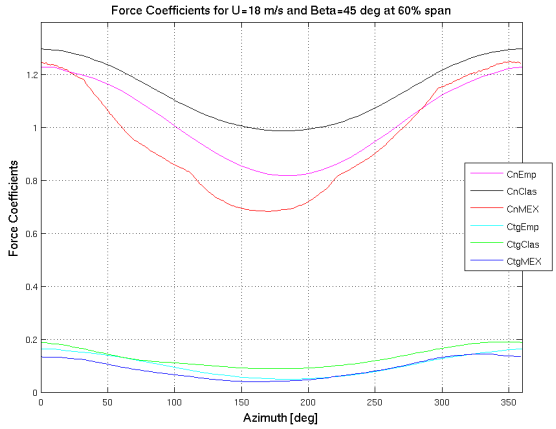

Figure 4.5 10: BEM models comparison for U=18 m/s at 60% spanwise station and yaw angle of 45 deg

When considering the smaller yaw angle one can see that the experimental force coefficients will have a larger magnitude but a smaller amplitude of variation with the azimuthal position. As for the larger yaw-misalignment, it is clear in the figure above that the magnitude of the experimental force coefficients is decreased, while the amplitude of azimuthal variation is increased. These trends can be understood by considering the geometric effect of skewed inflow, expressed by equation 2.2.3 which is shown again for convenience:

$$\phi = atan\left(\frac{[U_{Wind}\cos(\beta)](1-a)}{[\Omega r - U_{Wind}\sin(\beta)\cos(\psi)](1+a')}\right)$$

Minding the expression one can see that if the yaw-misalignment is decreased, the numerator will increase, and consequentially the inflow angle and the angle of attack will increase; This will bring about larger magnitudes of the force coefficients. On the other hand, if the yaw angle increases, it is clear that the term associated with the azimuthal position will increase. Thus the variation of the magnitude of the force coefficients over a revolution will also become greater.

As for the performance of the implemented models, the figures above indicate that the empirical BEM method yields a better agreement with experimental data, when considering different yaw-misalignment angles. As for the classical BEM method, and similarly to what was obtained before for other data points, it seems there is an overprediction of the force coefficients.

Quantitative Comparison

With the objective of quantitatively assessing the performance of the implemented calculation methods, the **average relative error** in the **normal force coefficient** was computed for both the empirical and the classical BEM models. The uncertainties associated with the chordwise forces are not addressed since these are expected to be of much smaller magnitude, and also since some of the dynamic stall models previously considered do not include chordwise loading computation.

The magnitude of the error was calculated by averaging the relative error of each model over the azimuth, assuming the MEXICO data to be the exact solution. For each of the wind tunnel speeds, the results were averaged

over every yaw angle, using the data points from table 4.4.2. The expression used to compute the average relative error in the normal force coefficient at each spanwise station and wind tunnel speed is thus:

$$\frac{1}{3}\sum_{\beta}\ \frac{1}{360}\sum_{\psi=1}^{360}\ \frac{\left|C_{n,Model}(\psi)-C_{n,MEXICO}(\psi)\right|}{C_{n,MEXICO}(\psi)} \qquad , \qquad \beta=\{15\,;30\,;45\}\ \ deg \tag{4.5.1}$$

For the wind tunnel speed of **15 m/s** the following results were obtained:

Avg Rel Error (%)	25% span	35% span	60% span	82% span	92% span
Classical BEM	30.4	18.1	23.3	20.7	16.9
Empirical BEM	18.6	14.5	12.2	6.1	14.5

Table 4.5.1 - Average Normal Force coefficient relative error for U=15 m/s

And for the **18 m/s** case:

Avg Rel Error (%)	25% span	35% span	60% span	82% span	92% span
Classical BEM	25.8	16.6	13.9	19.6	18.7
Empirical BEM	21.1	13.1	9.3	8.9	9.2

Table 4.5.2 - Average Normal Force coefficient relative error for U=18 m/s

Analysing the tables above it is clear that the **empirical BEM method performs better than the classical model**, at both wind tunnel speeds and all spanwise stations. The tables also show that the relative errors are larger at the more inboard stations, which had already been noticed in the azimuthal plots and is believed to be due to the unaccounted rotational augmentation.

As for the magnitude of the expected uncertainty in the empirical BEM model, one can see that for the sections where rotational augmentation is negligible, the average relative error in the normal force coefficient is approximately **10%**; this is particularly noticeable at the higher wind speed trials.

4.6) Conclusions and Recommendations

From the discussion above, one can draw the following conclusions:

- It is necessary to implement a correction on the aerodynamic force coefficients to account for rotational augmentation, since both implemented BEM models fail to predict the experimental loading at the inboard sections.
- At spanwise sections where rotational effects are not significant, generally the BEM models are able to

capture the observed experimental trends. Reasonable agreement is found for the different wind tunnel speeds and yaw angles considered.

- Comparing the performance of both implemented methods, clearly the empirical BEM model yields more accurate load predictions than the classical method. Better results were found for all spanwise stations and data points considered, and consequentially the empirical model should be preferred when implementing the DS model.
- Regarding the magnitude of the expected error in the empirical BEM method at outboard spanwise sections, for the highest considered wind speed case it is approximately **10 %**. Still this value is expected to decrease with increasing wind speeds, as the advance/retreating blade effect becomes more important and the induced velocities smaller.
- In all considered data points the classical BEM method overpredicts the aerodynamic loading, which is consistent with what was found in previous comparisons of MEXICO data with BEM models, such as [26].

5) Selection, Implementation and Validation of the Dynamic Stall Model

It has been previously explained that the DS model needs to be included in the BEM iteration loop, so that the unsteady effects can be simulated and the calculated loads compared with the MEXICO results. However, it is good practice to firstly be certain that the DS model is properly implemented before introducing it in the BEM code. It is thus the objective of this chapter to describe the implementation and to verify the DS model.

This chapter starts by presenting a qualitative discussion on the DS models used in the HAWT framework, and selecting the model for implementation. In section 5.2 the assumption of incompressibility is verified, and in section 5.3 the Beddoes-Leishman (BL) DS model is thoroughly described, and its implementation is discussed. Section 5.4 addresses the influence of thick airfoils on the BL DS model, and section 5.5 puts forward two different approaches to denote LE separation. In section 5.6 the values used in the empirical constants of the DS model are discussed. The experimental data used for validation of the implemented model is mentioned in section 5.7, and then the results obtained are shown and discussed in section 5.8. Finally in section 5.9 the conclusions drawn in this chapter are presented, together with some recommendations.

5.1) The choice of a Dynamic Stall Model

Ideally one would prefer to implement various DS models and compare their load prediction performance with the results from the MEXICO; initially it was thought that such an analysis could be conducted in this master thesis, but soon it was clear that implementing and validating a DS load prediction model alone required a considerable amount of time. Consequentially, and also since there were other objectives set for this assignment, it was chosen to analyse the load prediction capability of a single DS model in a yaw-misaligned wind turbine.

When thinking of modelling DS in a wind turbine environment, and based on the literature study conducted, it is this author's opinion that the following methods should be considered:

- ECN's 1st order model [21]
- Larsen et al. [19]
- Beddoes-Leishman [16]
- Sheng et al. [23]

The methods indicated above are ordered from top to bottom with increasing complexity, i.e. ECN's model is

the least complicated approach while the method of Sheng et al is the most complex; a brief qualitative description of each model was given previously, and for further details the indicated references can be consulted.

Naturally, when increasing the degree of complexity of a given model, the main goal is to obtain a better level of agreement with experimental results than simpler methods can provide; however, one must always keep in mind what is the scope of application of the model.

The DS load prediction methods mentioned above have been created based on the interpretation of 2D airfoil wind tunnel test data; consequentially several of the constants introduced in these models rely on some "empirical feel" of the unsteady physical phenomena taking place during pitching or heaving oscillations.

However, the main goal of this master thesis research is to simulate the aerodynamics of a wind turbine in a yawed configuration, which is far more complicated than the one the DS models were derived with. Because of this, it is understandable that a very complex DS load prediction method might not perform well when compared with the MEXICO results.

On the other hand, it would be preferable to implement a DS model which simulates, at least to some degree, the physical phenomena of unsteady airfoil aerodynamics; in other words, one would ideally opt by a model which entails more than a simple re-synthesis of experimental data.

From the discussion above, and also since the method is widely used in commercial applications, it was chosen to implement the **Beddoes-Leishman DS model**. One can thus expect the unsteady airfoil aerodynamic physical phenomena to be simulated, while keeping the amount of empirical "tuning" parameters to a reasonably simple degree.

5.2) The Assumption of Incompressibility

It is important to mention that in the scope of Wind Engineering the compressibility of air is usually neglected, since one is in presence of small magnitude velocities; in the MEXICO project the highest rotational speed trials were carried out with Ω=44.4 rad/s and the largest tunnel speed tested was 30 m/s, resulting in a maximum local speed at the tip of

$$V_{eff_{MAX}} = \sqrt{(44.4 \times 2.25)^2 + 30^2} \approx 104\, m/s \tag{5.2.1}$$

The speed of sound in dry air at 15º C and atmospheric pressure is approximately $a_{air} \approx 343\, m/s$, and so it is clear that also within the cases considered in the MEXICO the compressibility of air is negligible, since $V_{eff_{MAX}} < a_{air}/3$.

Being so, in the implementation of the dynamic stall model **incompressibility** was assumed, and in the following sections the equations presented implicitly assume that condition.

5.3) The Model Explained

Even though the various phenomena involved in the dynamic stall process are intrinsically related, Beddoes and Leishman managed to split it in **modules.** The unsteady loads are thus computed by considering each module sequentially, in the following manner:

- In the **attached flow** module, and using the AOA history, α(t), as input, the unsteady attached force coefficients are computed.
- These coefficients are then used as input in the **trailing edge separation** module, where both the peak pressure lag and the boundary layer lag are included. The force coefficients are thus recalculated incorporating the effects of the unsteady trailing edge separation point.
- The criterion to determine whether **leading edge separation** has occurred is based on a critical pressure, and so this module uses the normal force coefficient including the pressure lag (not the viscous lag) to compute the vortex time; this last variable keeps track of the time from which the leading edge pressure vortex is detached.
- Finally, the **vortex lift** module is used, with the vortex time variable as input, and the outcome is added to the result from the trailing edge separation module to yield the total, instantaneous normal force coefficient on the airfoil.

Each module will now be addressed more thoroughly, and the expressions used and assumptions made will be explained.

Attached Flow Module

The approach used to determine the instantaneous loads when there is no separated flow formulates the problem in terms of a superposition of indicial aerodynamic responses, as mentioned in [16]. In unsteady attached flow the aerodynamic forces acting on an airfoil can be divided in two components, circulatory and impulsive, and in this module each of these contributions will be considered separately.

Circulatory Component

As indicated by the name, the circulatory loading is related with the vorticity, both bound and shed, that the flow is imposing on the airfoil, and it builds up quickly to the steady state value; the circulatory normal force arising from an accumulating series of step inputs in the angle of attack can be obtained using an **equivalent angle of attack**, according to [16]

$$C^{C}_{N,n} = C_{N_\alpha} \alpha_{Eq,n} = C_{N_\alpha}\left(\alpha_n - X_n - Y_n\right) \tag{5.3.1}$$

where ***n*** denotes the current sample; clearly, the delayed response with respect to the steady case is introduced with the deficiency functions, X_n and Y_n , which are given by the set of equations:

$$X_n = X_{n-1}\exp\left(-b_1 \Delta S\right) + A_1 \Delta\alpha_n \exp\left(-b_1 \Delta S/2\right)$$
$$Y_n = Y_{n-1}\exp\left(-b_2 \Delta S\right) + A_2 \Delta\alpha_n \exp\left(-b_2 \Delta S/2\right) \quad (5.3.2)$$

where ΔS is the distance travelled by the airfoil in semi-chords over a sample interval Δt , and where $\Delta\alpha_n$ is the corresponding change in the angle of attack over the time interval.

The coefficients $A_{1,}\, A_{2,}\, b_1, b_2$ are constants which come from the empirical approximation to the indicial response, in terms of the exponential function; their values are given in [16] and shown in table 5.6.1 in section 5.6.

When the contribution of the deficiency functions is included all the information of the previously shed wake's effects on the airloads is taken into account.

Impulsive Component

Whenever an airfoil undergoes a rapid motion there will be an initial non-circulatory loading, caused by local pressure variations, according to piston theory [34], which quickly tends to vanish. The magnitude of the impulsive normal force can be obtained with [16] :

$$C^I_{N,n} = \frac{3c}{V_{eff}}\left(\frac{\Delta\alpha_n}{\Delta t} - D_n\right) \quad (5.3.3)$$

Where V_{eff} is the effective velocity the airfoil is working at and ***c*** represents the airfoil chord. In this case the deficiency function is given by:

$$D_n = D_{n-1}\exp\left(\frac{-\Delta t}{K_\alpha T_I}\right) + \left(\frac{\Delta\alpha_n - \Delta\alpha_{n-1}}{\Delta t}\right)\exp\left(\frac{-\Delta t}{2K_\alpha T_I}\right) \quad (5.3.4)$$

where $T_I = c/a$ is the non-circulatory time constant, and where the factor K_α is a function of the Mach number which, given the assumption of incompressibility, will also become a constant, with the value indicated in table 5.6.1.

Once both the circulatory and impulsive contributions have been calculated, the total normal force coefficient, for attached flow, in a given time instant, is given by:

$$C^P_{N,n} = C^I_{N,n} + C^C_{N,n} \quad (5.3.5)$$

Trailing Edge Separation Module

Even though dynamic stall necessarily encompasses stall delay and vorticity build up near the leading edge with consequent vortex detachment, there is evidence that trailing edge separation may play a significant role on the onset of dynamic stall [16]. For this reason it is considered in the present model.

Firstly, it is necessary to model the trailing edge separated flow in **steady** conditions, which can be done by using Kirchhoff theory according to:

$$C_N = C_{N_\alpha}\left(\frac{1+\sqrt{f}}{2}\right)^2 \alpha \tag{5.3.6}$$

where ***f*** is the dimensionless suction side separation point, seen from the leading edge, meaning that ***f***=1 when the flow is fully attached and ***f*** = 0 when the flow is completely separated.

By inverting the expression above and using the airfoil's static characteristic, it is possible to derive the value of the separation point as a function of the angle of attack, obtaining ***f(α)***.

For **unsteady** conditions there will be a delay in the leading edge pressure response with respect to the normal force coefficient derived in the attached flow module. Consequentially a time lag is introduced in the normal force coefficient to produce a substitute value, which for a discretely sampled system is written as:

$$C'_{N,n} = C_{N,n} - D_{P,n} \tag{5.3.7}$$

where the deficiency function is computed with

$$D_{P,n} = D_{P,n-1}\exp\left(\frac{-\Delta S}{T_P}\right) + \left(C^P_{N,n} - C^P_{N,n-1}\right)\exp\left(\frac{-\Delta S}{2T_P}\right) \tag{5.3.8}$$

The time constant T_P is a function of the Mach number and is usually determined from unsteady airfoil data; it appears that this parameter is largely independent of the airfoil shape [16], and given the narrow range of relevant Mach numbers it will be assumed constant in all considered cases. The value used in this assignment is given in table 5.6.2 in section 5.6, together with a brief discussion justifying its choice.

Once the unsteady pressure response is incorporated, it is possible to define yet another effective angle of attack, which yields the same leading edge pressure as for the equivalent quasi-steady case, computed with

$$\alpha_{f,n}(t) = \frac{C'_{N,n} - C_{N_0}}{C_{N_\alpha}} \tag{5.3.9}$$

where C_{N_0} is the normal force coefficient obtained when the angle of attack is zero. With this effective angle of attack and using the static separation point characteristic described above, it is now possible to compute the effective separation point

$$f'_n = f\left(\alpha_{f,n}\right) \tag{5.3.10}$$

As previously mentioned, the boundary layer's response is also not instantaneous, and the unsteady effects can be represented by applying a first order lag to the separation point, according to

$$f''_n = f'_n - D_{f,n} \tag{5.3.11}$$

where in this case the deficiency function is computed with

$$D_{f_n} = D_{f_{n-1}}\exp\left(\frac{-\Delta S}{T_f}\right) + \left(f'_n - f'_{n-1}\right)\exp\left(\frac{-\Delta S}{2T_f}\right) \tag{5.3.12}$$

Like in the pressure lag, T_f is time constant which should be derived from unsteady airfoil data but it will be assumed constant in all considered cases, with the value indicated in table 5.6.2.

Finally, the normal force coefficient incorporating both the pressure and viscous lag is computed with the unsteady trailing edge separation point using the Kirchhoff relation at each time instant:

$$C_{N,n}^{f} = C_{N_\alpha}\left(\frac{1+\sqrt{f''_n}}{2}\right)^2 \alpha_{Eq,n} + C_{N,n}^{I} \tag{5.3.13}$$

Leading Edge Separation

According to [16], defining the conditions under which leading edge separation takes place is the most critical aspect of dynamic stall modelling; it is however possible to mark the onset of static leading edge separation through a critical leading edge pressure criterion, which was confirmed to be valid also for unsteady conditions in [13].

Since leading edge pressures are related to the normal force coefficient, it is possible to operate in the C_n domain alone by defining a critical value, $C_{n,I}$, which corresponds to the critical pressure for separation onset at the appropriate Mach Number .

In practice this **critical value of the normal coefficient** can be obtained from the airfoil's **static characteristic** by taking the C_n value at the angle of attack that corresponds to the **break in the pitching moment**; this choice is understandable since when leading edge separation occurs there will necessarily be centre of pressure movements and consequentially abrupt changes in the pitching moment.

Since the criterion used to define whether leading edge separation has occurred is based on a critical pressure, it is logical that the unsteady normal coefficient used to assess whether this condition has been reached includes the lag in leading edge pressure response, given previously in expression 5.3.7.

In general dynamic stall encompasses the formation of a vortex in the leading edge area of the airfoil which subsequently detaches from the surface and is convected downstream. Naturally, it is very important to keep track of the position of this concentrated vorticity since it has a great impact on the total normal force acting on the airfoil. In the present model this tracking is accomplished by storing a non-dimensional vortex time parameter, in semi-chords, according to:

$$\tau_{v,n} = \tau_{v,n-1} + \frac{dt}{c/2} \cdot V_{Eff} 0.45 \quad ,if \quad C'_{N,n} > C_{N,I} \tag{5.3.14}$$

As indicated above, this vortex time will only be incremented if critical conditions have been met, and the 0.45 factor is introduced because experimental tests [16] determined the rate at which the vortex convection occurs to be somewhat less than half of the effective velocity.

Naturally, over a periodic angle of attack excitation there may be a vortex build up and separation with every oscillation, and consequentially it is necessary to reset the vortex time parameter when the vortex that originated it ceases to have a meaningful contribution. This is accomplished by imposing the condition:

$$\tau_{v,n}=0 \quad if \quad C_{N,n}<C_{N,I} \ \wedge \ \Delta\alpha_n>0 \tag{5.3.15}$$

Assuming an oscillating motion, and according to the conditional expression above, the vortex will then be assumed to have a negligible contribution to the normal force on the airfoil in the upstroke of the movement, as long as the critical conditional is not met.

We can verify the validity of this assumption by using reference values for the problem we wish to model; if there is a leading edge vortex detachment in the oscillation, we are certain that, by the time the following upstroke starts, a time interval of at least **half the oscillation period** has passed, which may be written as:

$$\Delta t_{halfstroke}=\frac{P_{OSC}}{2}=\frac{1}{2f_{OSC}}=\frac{\pi}{\omega_{OSC}} \tag{5.3.16}$$

In terms of the vortex time parameter and introducing the **reduced frequency**, ***k***, we come to

$$\tau_{halfstroke}=\frac{\pi 2 V_{Eff}}{\omega c}0.45=\frac{0.45\pi}{k} \tag{5.3.17}$$

Now assuming a high reduced frequency ***k*=0.1** (in the wind turbine environment) and subtracting the airfoil's length, we come to a representative distance travelled by a vortex, from the trailing edge, in the semi-chords:

$$\Delta S=0.45\frac{\pi}{0.1}-2=12.1 \tag{5.3.18}$$

The contribution of the vortex to the normal force in the airfoil peaks when it is situated just above the trailing edge. From the instant the concentrated vorticity is downstream of the airfoil its contribution to the total normal force coefficient is decaying according to [16]

$$C_N^V=C_N^{V_{MAX}}\exp\left(\frac{-\Delta S}{T_V}\right)=0.132\,C_N^{V_{MAX}} \tag{5.3.19}$$

Where the vortex decay constant was set to T_V =6 according to [35].

Finally, it is possible to witness that even when a high reduced frequency of 0.1 is considered, the vortex's contribution to the normal force coefficient will be reduced to approximately 13% of its maximum by the time the following upstroke starts. Keeping in mind that the vortex lift has a small magnitude when compared to the total lift the airfoil experiences, expression 5.3.15 can be considered valid.

Vortex Lift Module

In this last module, the contribution of the concentrated vorticity to the normal force coefficient is computed, based on the vortex time parameter introduced previously. According to Leishman, as long as the vortex remains attached there are no significant changes in the pressure distribution, and consequentially the forces can be described by ignoring the vortex. After the concentrated vorticity detaches, the development of stall seems to obey a basic common process since qualitatively similar results have been observed as different modes of forcing were imposed

[16].

As long as the vortex is situated over the airfoil, it is assumed that the associated contribution to the normal force coefficient will increase. This increment is determined by the difference between the instantaneous linearised value of the unsteady circulatory lift, given in 5.3.1, and the corresponding unsteady nonlinear lift as given by the Kirchhoff approximation:

$$C_{V,n} = C^{C}_{N,n}\left(1 - K_{N,n}\right) \qquad (5.3.20)$$

where

$$K_N = \frac{\left(1+\sqrt{f''}\right)^2}{4} \qquad (5.3.21)$$

Finally, the **total accumulated vortex contribution** is calculated using

$$C^{V}_{N,n} = C^{V}_{N,n-1}\exp\left(\frac{-\Delta S}{T_v}\right) + \left(C_{V,n} - C_{V,n-1}\right)\left(\frac{-\Delta S}{2\mathrm{T}_v}\right) \quad if \quad \tau_v < T_{vl} \qquad (5.3.22)$$

which, as we can see, is allowed to decay exponentially but may also be updated with a new change in the vortex lift. The empirical constant T_v represents the vortex decay constant, and was introduced in equation 5.3.19. In the expression above one should notice that the vortex lift contribution is only to be considered if the concentrated vorticity is located over the airfoil, represented by the condition $\tau_v < T_{vl}$,otherwise the expression degenerates in 5.3.19 . The value of T_{vl} is given along with the other empirical time constants in table 5.6.2 .

It is also important to mention that a restriction was imposed so that the vortex contribution to the total lift may never be negative. One can understand that, in an oscillatory motion, if the critical condition is not reached, i.e. if there is no leading edge separation, on the downstroke of the movement the angle of attack will be decreased and consequentially flow reattachment from the trailing edge will take place. According to expression 5.3.20 this means that the vortex lift would have a negative derivative in time, and thus that the total accumulated vortex contribution for the lift 5.3.22 could become negative. This however is a physically meaningless situation, and so it was chosen to apply expression 5.3.22 only when

$$C_{V_n} - C_{V_{n-1}} > 0$$

and otherwise simply use equation 5.3.19, which allows for the exponential decay of the vortex contribution to the normal force coefficient.

At last, the instantaneous total normal coefficient can be obtained by superposition of the unsteady non-linear contribution 5.3.13 and the vortex lift term:

$$C_{N,n} = C^{f}_{N,n} + C^{V}_{N,n} \qquad (5.3.23)$$

Tangential Force Coefficient

It is indicated in [16] that the unsteady tangential force coefficient, or chordwise force coefficient, can be computed according to :

$$C_{C,n} = \eta C_{N_n} \alpha_{E,n}^2 \sqrt{f_n''}$$

This value includes both the leading edge pressure and viscous lag, and it represents only the pressure contribution to the chordwise force.

In the expression above η represents the recovery factor, which is introduced to allow for the fact that the airfoil does not realize 100 percent of the chordwise force attained in potential flow. Also according to [16], this factor can be obtained empirically from static airfoil data, and a typical value is $\eta \approx 0.95$.

In the present implementation however the unsteady tangential force coefficient will not be computed. Instead, in the BEM iteration loop the chordwise force coefficient will simply be derived from the static airfoil curve using the instantaneous angle of attack.

Illustrated Calculation Procedure

A flowchart is included below which exemplifies the working methodology of the model, with the objective of clarifying whole process; even though the implemented algorithm obviously uses some of the values computed in the previous iteration, the figure below represents the open loop system:

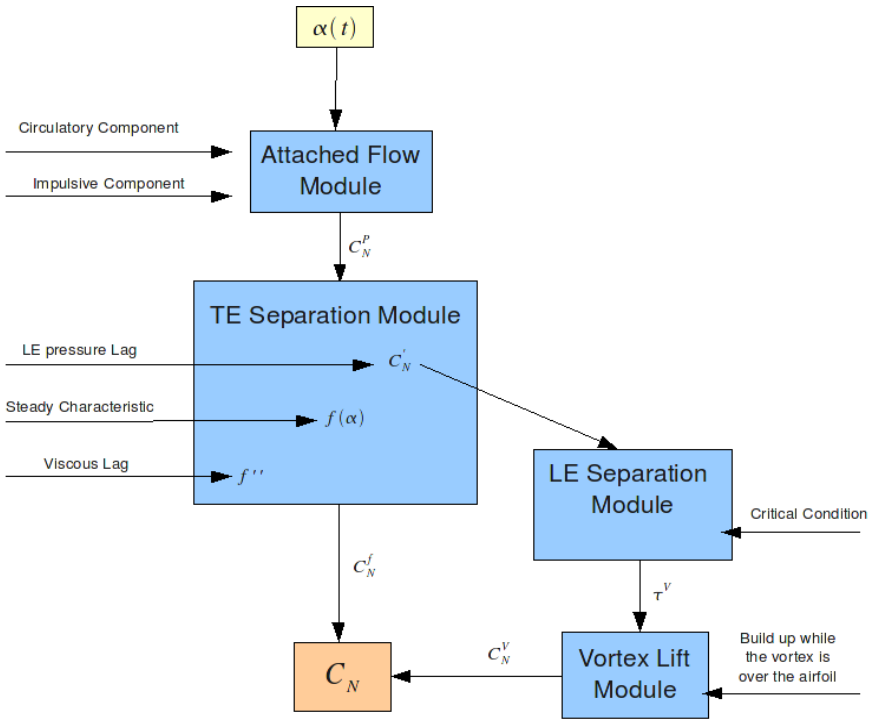

Figure 5.3 1: Flowchart of the Beddoes-Leishman DS model

5.4) The influence of thick airfoils

Mostly because of structural integrity, the airfoil sections found in wind turbine blades are usually quite thick, say larger than 15%. However, the Beddoes-Leishman DS model was originally developed for helicopter industry applications, where usually considerably thinner airfoils are used.

The stalling characteristic of a profile is mainly dependent on its relative thickness; generally speaking, in thin airfoils usually the separation point is located near the leading edge, while in thick airfoil sections typically separation occurs at the trailing edge (TE) region. Naturally the topology of stall can be more complex, if combined LE and TE separation is present, and it is also dependent on other factors, such as the Reynolds number. For more information on the topic the reader is referred to [36] and [37].

As mentioned previously, the Beddoes-Leishman DS model assumes that leading edge separation occurs when a critical normal force coefficient is reached, which coincides with the break in the static pitching moment curve of the airfoil. However, it is clear that if significant trailing edge separation occurs, the static leading edge separation point may actually correspond to a value of the normal force coefficient smaller than its maximum, i.e. $C_{N,\,LEsep} < C_{N,\,MAX}$. Taking for instance the NACA64418 airfoil experimental static characteristic from [25], which has a relative thickness of 18%:

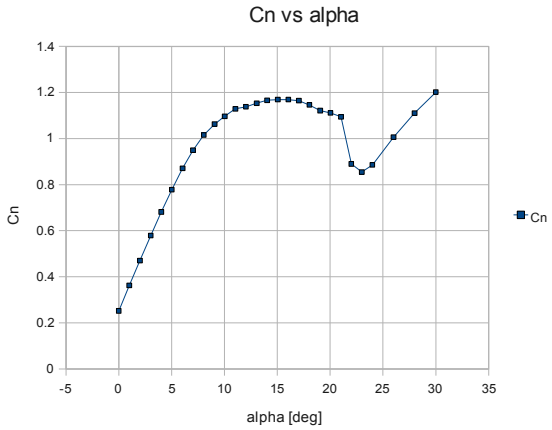

Figure 5.4 1: Normal force coefficient characteristic of the NACA64418 at Re=700 000

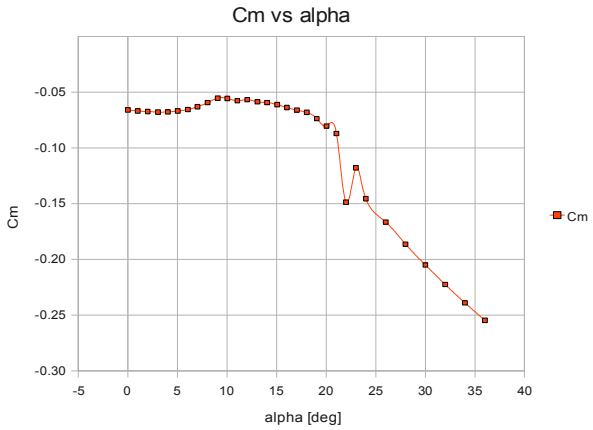

Figure 5.4 2: Pitching moment coefficient characteristic of the NACA64418 at Re=700 000

In figure 5.4 1 it is clear hat the break in the pitching moment takes place at an angle of attack of approximately 22 deg. Now minding the normal force coefficient curve, one can see that this incidence angle corresponds to a value of approximately C_N =1.1, which is smaller that the maximum value. Also, such a magnitude of the normal force coefficient is actually firstly observed at an angle of attack of roughly 10 deg.

Obviously imposing this value of the normal force coefficient for the critical condition in the DS model would yield invalid results, since leading edge stall would be predicted to occur much too soon, when the flow is still expected to be attached over the most of the airfoil's surface.

Moreover, one might actually be working with an airfoil where no abrupt drop in the pitching curve can easily be identified, if the stall characteristic is very smooth. Consequentially it is clear that another criterion is needed

to derive the critical normal force coefficient, $C_{N,I}$, when considering thick airfoils.

5.5) Leading Edge Stall occurrence Criteria

Critical Angle of Attack

In [38] Timmer suggests a relation to predict the occurrence of leading edge stall on wind turbine application airfoils based on the thickness of the nose, having obtained a very good agreement for several low speed airfoil sections, in static conditions, at a constant $Re = 1\text{x}10^6$.

In his work Timmer assumes the airfoil upper nose thickness to be represented by the **y/c** ordinate at the **x/c=0.0125** chord station, and the **leading edge separation angle of attack** is approximated by:

$$\alpha_{LEsep} = 1170.8(y/c) - 1.33 \tag{5.5.1}$$

With the result being given in degrees. Using this LE separation angle of attack, it is then possible to derive a **critical normal force coefficient**, $C_{n,I}$ by assuming the flow remains fully attached, and thus using the thin airfoil theory

$$C_{n,I} = \left(2\pi\alpha_{LEsep} + C_{l,0}\right)\cos\alpha_{LEsep} \tag{5.5.2}$$

Obviously this expression leads to extremely large normal force coefficients, which may actually never occur in reality, given the fact that considerable trailing edge separation is most certainly present at such high incidence angles. However, one must keep in mind that leading edge separation is related with a critical value of leading edge pressure [13], and since we are working in the C_n domain, this critical condition corresponds to the normal coefficient one would obtain in attached flow, i.e. the value given in expression 5.3.5 .

The validity of this methodology to determine the onset of leading edge separation will be verified subsequently, as the results from the implemented model are compared with experimental data obtained for thick oscillating airfoil sections.

Maximum Cn

Another criterion for the onset of leading edge separation will now also be considered; the dynamic stall model may also be set so that the critical C_n is assumed to correspond to the **maximum normal coefficient**.

$$C_{n,I} = C_{n,MAX} \tag{5.5.3}$$

For thin airfoils this criterion and the break in the pitching moment, suggested in [16], yield identical values for the critical normal force coefficient, since usually when leading edge stall takes place very little trailing edge separation has occurred; however, if one is in presence of **thick** airfoils, considerable trailing edge separation is expected to occur before leading edge stall takes place, and thus by using the maximum C_n as the critical value to denote the onset of leading edge separation one comes to values which may be substantially different from using the approach from[16].

5.6) Choosing the Empirical time constants

The values of the time constants used in the DS method will obviously have a large impact on the load predictions, since they directly affect the dynamics of the unsteady model; ideally, one would perform an optimization of these time constants for each of the considered airfoil sections, in which a procedure along the lines of [39] could be followed.

However, since there is no available unsteady aerodynamic data for MEXICO blade's airfoils, it was chosen to select a set of **"reference" values**, from which one can expect to obtain a reasonable load prediction capability.

The time constants related with the unsteady **attached flow** are insensitive to the Mach number and airfoil section's shape, and are given in the table below from [16]:

A_1	A_2	b_1	b_2	K_α
0.3	0.7	0.14	0.53	0.75

Table 5.6.1 - Empirical constants for attached flow

However, when there is **flow separation** the choice of the values of the time constants becomes more delicate. In [16] it is indicated that the time constants associated with the pressure lag and with the vortex lift, T_P, T_v and T_{vl}, are **mainly dependent** of the **Mach number**, and not so much of the airfoil shape. As for the viscous lag, T_f, the same reference indicates that this parameter is sensitive both to profile geometry and Mach number.

For the magnitudes of the empirical time constants, the original paper of the Beddoes-Leishman DS model refers to a document from *Westland Helicopters* [35]. In this reference, values of the empirical time constants are given for the NACA0012 airfoil based on unsteady experiments at $Re = 8 \times 10^6$, and for Mach numbers ranging from 0.3 to 0.8. Table 5.6.2 displays the values indicated in [35] for the lowest Mach number, which is of the greatest relevance in the present case. This set of parameters will be referred to as "Westland values".

The Swedish Aeronautical Research Institute (FFA) conducted an optimization of the empirical time constants in a Beddoes-Leishman DS model [39]. This was performed by comparing load predictions with experimental data, and was carried out for several airfoils at low Mach numbers. "Reference" values were put forward, which yielded reasonable agreement for the majority of the considered airfoils, and are shown also in table 5.6.2. This set of parameters will be referred to as "FFA values".

However, it is important to mention that the Beddoes-Leishman DS model implemented in [39] does not use a criterion for the start of "vortex travelling", and vortex contribution is allowed as long as the angle of attack is increasing. In other words, the approach used assumes that **no leading edge separation** takes place, based on the fact that wind turbine application airfoils are thick.

The values of the empirical time constants in the current implemented model were selected taking into account both references mentioned above:

- For the **peak pressure lag,** T_P, it was chosen to follow the trend of decreasing Mach number from [35]; this means that since $T_P(M=0.3) < T_P(M=0.4) \Rightarrow T_{P.Implemented} < T_P(M=0.3)$. This was also

done because in [39] a "reference" value for this time constant was not clearly indicated.

- Regarding the **boundary layer lag**, T_f , the "reference" value from [39] was used; this choice was motivated since this parameter is expected to be sensitive to airfoil shape, and consequentially, if one wishes to apply the DS model to different airfoil sections, it makes little sense to use the value specifically derived for a (thinner) profile from [35].
- As for the time constants related with the **vortex lift**, T_v and T_{vl} , it was again chosen to follow the trend of decreasing Mach number from [35]; this procedure was taken since the DS model implemented in [39] did not consider vortex shedding, and consequentially the value derived in the optimization is not expected to yield a good level of prediction.

The set of parameters from the references mentioned above are indicated in table 5.6.2, together with the values used in the current implementation:

Time Constants	T_P	T_f	T_v	T_{vl}
Westland (M=0.3)	1.7	3	6	7
FFA ("Reference")	0.8	5	2	-
Implemented Model	**1.5**	**5**	**6**	**5**

Table 5.6.2 - Values of the empirical time constants for separated flow

5.7) Validation Cases

To validate the implemented model it is necessary to compare the results with experimental 2D unsteady aerodynamic data, preferably using a set of parameters which simulates, at least to some degree, what is expected in the MEXICO trials. However unsteady wind tunnel aerodynamic data is not publicly available for every desired airfoil and set of parameters, and in the present case the choice was limited to the OSU database [40] of unsteady measurements.

From this database, the aerodynamic profiles were chosen to have identical relative thicknesses as the airfoils which make up the MEXICO rotor blade, that is, t/c = [0.25;0.21;0.18]. Naturally, having the same maximum relative thickness does not mean that the airfoils are identical, but should at least be representative of the behaviour one may expect to encounter in the MEXICO environment.

Having this in mind, the airfoils chosen were the **S814** for the **root region**, **S809** for the **mid-section region**, and the **S825** for the **tip region**. The figure below shows the geometry of each of these airfoil sections as well as of the

"corresponding" MEXICO profiles[6]:

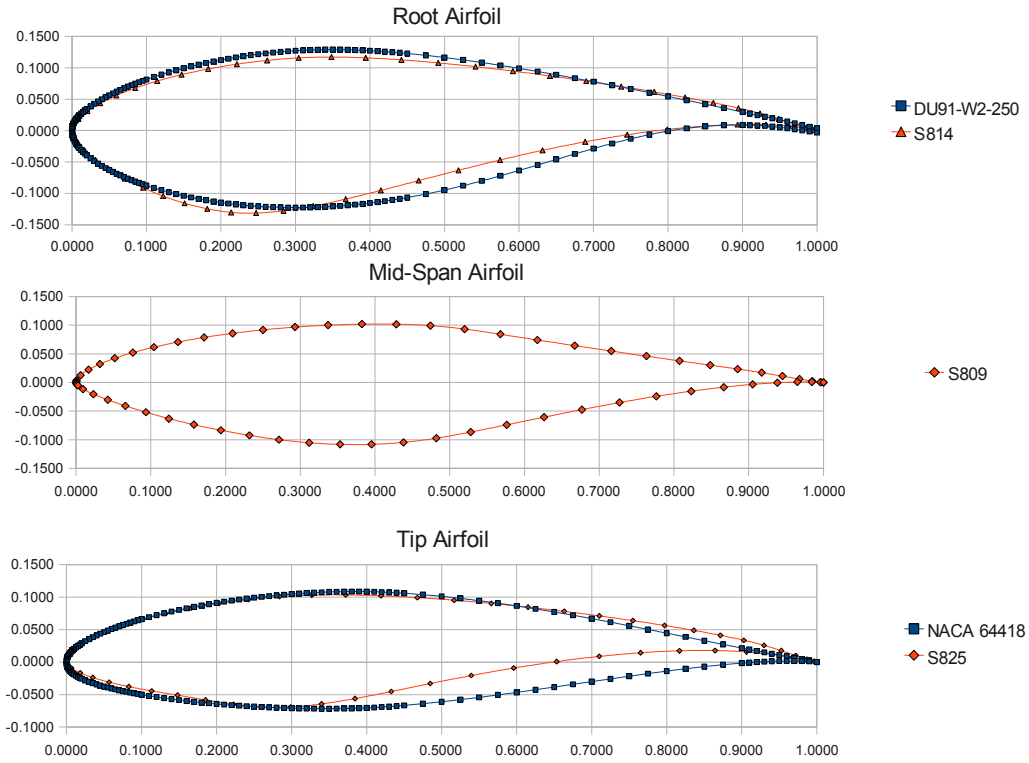

Figure 5.7 1: Geometry of airfoil sections used in the DS model validation

In the table below the relevant characteristics of each airfoil are shown, as well as the $C_{n,I}$ obtained with each of the leading edge separation criterion given above:

Airfoil	Thickness	Moment Break AOA	Timmer's LE Separation AOA	Cn_crit Timmer	Cn_Crit Cn_Max
S825	17%	21º	22.7º	2.67	1.39
S809	21%	19º	20.5º	2.01	1.03
S814	24%	25º	25.7º	2.88	1.29

Table 5.7.1: Characteristics of the airfoil sections used in the DS model validation

Experimental Unsteady Data

The Reynolds number in the experiments selected from the OSU aerodynamic database was set to $Re = 1 \times 10^6$, and the geometric **angle of attack** was varying sinusoidally with a **10 deg amplitude around a 14 deg mean**[7].

[6] The geometry of the RISOE A1-21 airfoil is not displayed due to confidentiality

[7] In the OSU aerodynamic database the AOA amplitude of the unsteady data was 5 or 10 deg, and the mean AOA was 8,14 or 20 deg.

Minding the relevant frequencies of operation, mentioned in table 2.2.1, results are shown for **high and moderately high reduced frequencies** in the **root** airfoil, **moderate reduced frequency** at the **mid-span** airfoil and **low reduced** frequency for the **tip** airfoil section.

Reduced Frequency	Root Section	Mid-Span Section	Tip Section
Low (k≈0.027)	no	no	yes
Moderate (k≈0.053)	no	yes	no
Moderately High (k≈0.064)	yes	no	no
High (k≈0.094)	yes	no	no

Table 5.7.2: Validation Cases of the Beddoes-Leishman DS model

5.8) Results and Discussion

The results obtained with the Beddoes-Leishman DS model using **both leading edge stall criteria** mentioned before are now presented, and compared with the experimental unsteady data. The results obtained at all airfoil sections and for all reduced frequencies are shown in appendix D.

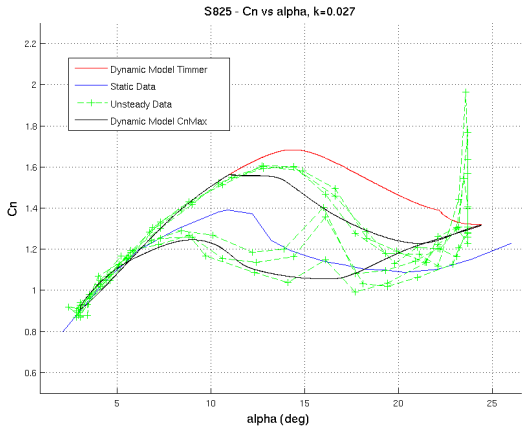

Figure 5.8 1: Tip region airfoil section at a low reduced frequency

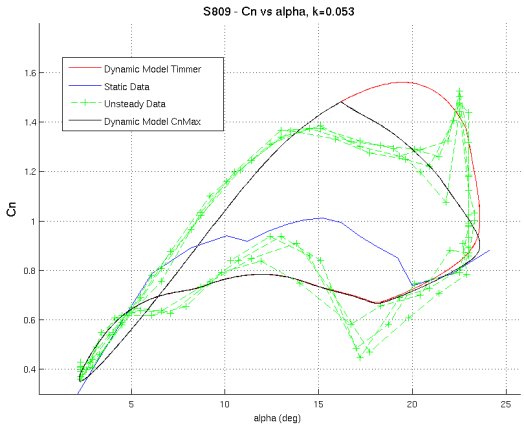

Figure 5.8 2: Mid-span region airfoil section at moderate reduced frequency

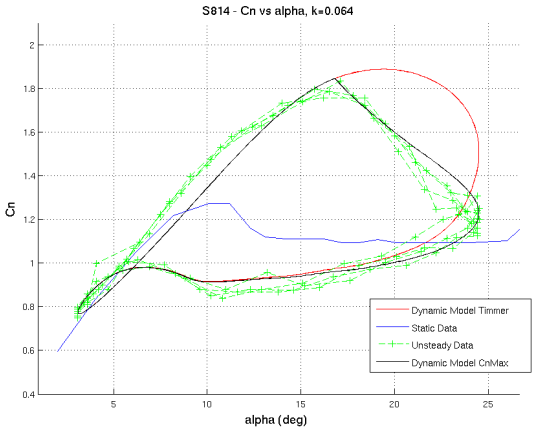

Figure 5.8 4: Root region airfoil section at moderately high reduced frequency

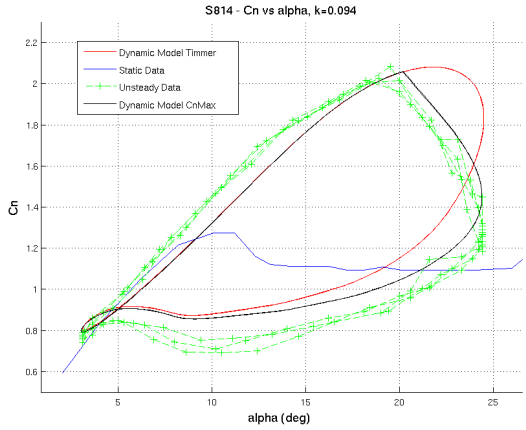

Figure 5.8 3: Root region airfoil section at high reduced frequency

Minding the results above one can say that generally reasonable to good agreement has been found between the DS model and the experimental data; in some of the loops it seems that the reattachment is not always well predicted, but this fact is to some extent expectable in Beddoes-Leishman model implementations, as discussed in [23].

It is also possible to witness what seems to be some secondary vortex shedding, especially in the thinner airfoils. This is present at the final part of the upstroke and is characterized by abrupt normal force coefficient peaks: it is also consistent with rapid pitching moment variations observed at these time instants. These phenomena are not modelled in the present implementation and, according to [23], they are specially occurring at low Mach numbers.

Now specifically addressing the two criteria used to denote the onset of leading edge separation, several aspects can be mentioned; firstly, given the very high values of the critical normal force coefficient imposed using Timmer's approach, it is assumed that there is actually no leading edge stall, which is why this criterion always yields data sets with no “kinks”.

However, and specially at higher frequencies, experimental data indicates there is leading edge stall, even for the thick airfoils, given the abrupt decay in normal force coefficient; this fact is also coherent with the break observed in the pitching moment coefficient, which occurs at a much lower angle of attack than in static conditions. Being so, it seems unrealistic to simply disregard leading edge stall in wind turbine application airfoil sections.

Comparing results obtained using the two criteria, in every case the $C_{n,MAX}$ approach yields load predictions at least as good as the ones obtained with Timmer's criterion. When higher frequencies are considered, it is clear that a better agreement is found using the $C_{n,MAX}$ criterion.

5.9) Conclusions and Recommendations

Analysing the results and the minding the discussion above, the following conclusions can be drawn:

- The Beddoes-Leishman DS model was successfully implemented, and tailored to correspond to the wind turbine environment by neglecting compressibility effects. The method was validated against unsteady 2D experimental data. Generally a good agreement was found.
- Airfoil sections similar to those comprising the MEXICO blades were chosen as input, since one intends to posteriorly compare the model's results with this experimental data.
- Since the original Beddoes-Leishman model was proposed for thin profiles, it was necessary to adapt the leading edge stall occurrence criteria for thick airfoil sections characteristic of wind turbine applications; two methods were proposed and tested, referred to as Timmer's and $C_{n,MAX}$ criteria.
- Regarding the performance of the two criteria the $C_{n,MAX}$ approach yielded load predictions at least as good as the ones obtained with Timmer's criterion. For higher frequencies clearly a better agreement was found using the $C_{n,MAX}$ criterion. This method should thus be used in the subsequent analysis of the MEXICO data.
- 2D wind tunnel experimental data indicated that, even when very thick airfoils are considered, leading edge stall may occur. Consequentially it seems unrealistic to disregard LE separation in wind turbine application profiles simply based on the fact that the airfoil sections are thick.

6) The Influence of Rotational Augmentation on the Sectional Aerodynamic Coefficients

It was made clear from the previous sections that the dynamic stall model requires static characteristics of aerodynamic force coefficient as a function of the angle of attack as input; in other words, both $C_l(\alpha)$ and $C_d(\alpha)$ steady curves must be supplied to the dynamic stall model so that the unsteady loads can be predicted. Also, as mentioned before, the blades from the MEXICO rotor are comprised of three different airfoil types, and consequentially the static $C_l(\alpha)$ and $C_d(\alpha)$ depend on the spanwise position. However, given the problem at hands, it is even more important to consider the influence of **rotational augmentation** on the aerodynamic coefficients over the spanwise positions of the blade.

This chapter starts by qualitatively describing the phenomenon of rotational augmentation in section 6.1. In section 6.2 the 3D force coefficients from the MEXICO rotor are determined, through an inverse BEM method, and in section 6.3 the results are shown. Section 6.4 discusses the aerodynamic coefficient implemented in the BEM code and finally section 6.5 states the conclusions drawn in this chapter.

6.1) Physical Description

The expression "rotational augmentation" refers to the **delay in stall occurrence** one can witness in the most inboard sections of a rotating blade, when compared to the 2D static characteristic of the airfoil. Since the separation over the airfoil is delayed for higher angles of attack, it is possible to obtain **very high maximum lift coefficients** at these spanwise sections, hence the "rotational augmentation" designation.

This phenomenon can be qualitatively understood by thinking of the parameters which influence the boundary layer present in a rotating blade; since the air in the vicinity of the blade will also be rotating, it will be pushed outwards in the spanwise direction, due to the centrifugal force and to the radial pressure gradient, and thus the flow velocity will have a cross component. Because this velocity component will be in a rotating reference frame, there will be a **Coriolis Force** acting on the air parcels, given by:

$$\vec{F}_{Cor} = -2\vec{\Omega} \vee \vec{V} \tag{6.1.1}$$

Since the linear velocity vector $\vec{V}$ has the outward direction and because the angular velocity vector $\vec{\Omega}$ is pointing in the direction perpendicular to the rotor plane, using the right-hand rule we can see that the Coriolis force acts to accelerate the fluid from the leading edge to the trailing edge of the airfoil. In other words, this contribution will make the pressure gradient over the airfoil section less adverse, and thus postpone the flow separation to higher angles of attack, allowing for very large maximum lift coefficients to be obtained.

A figure of the phenomenon is shown below, where the relevant vectorial quantities are represented:

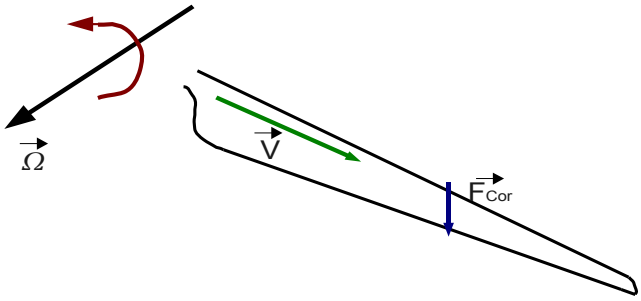

Figure 6.1 1: The rotational augmentation phenomenon

It should be noted that the rotational augmentation is **only significant at the inboard spanwise stations**; at the more outboard sections there will still be a spanwise velocity component, but the magnitude of the local effective velocity will be much larger, given the larger radius, and thus the influence of the Coriolis force becomes negligible. More information on this physical phenomenon can be found in [4].

6.2) Three Dimensional Force Coefficients Experimental Determination

In the present work it is necessary to know the dependency of the lift coefficient with angle of attack at the inboard spanwise stations of the MEXICO rotor, since rotational augmentation will most definitively be present and play an important role in the phenomena associated with dynamic stall.

Procedure

This determination was done by analysing the pressure data from several axial flow trials of the MEXICO. Following the procedure mentioned in chapter 4, for each considered trial the pressure distribution was interpolated using a cubic spline and was integrated over the surface of the airfoil section to yield both **Normal** and **Tangential** forces, F_n and F_{tg} respectively.

The convention used is again such that a positive normal force is pointing from the lower surface to the upper surface of the airfoil, while a positive tangential force is pointing from the trailing edge to the leading edge of the airfoil. One should note however that the **viscous contribution** is thus **not taken** into account.

To determine the angles of attack, and consequently the lift coefficient, a **local inverse BEM** method was used [18], according to which the local axial induction factor is determined with:

$$2a(1-a)\rho V_{wind}^2 .2\pi r\, dr = B.F_{ax}\, dr \tag{6.2.1}$$

and the tangential induction factor is computed with:

$$2a'(1-a)\rho V_{wind}\Omega r.2\pi r\, dr = B.F_{rot}\, dr \tag{6.2.2}$$

In the expressions above F_{ax} and F_{rot} represent the aerodynamic force acting on each blade element,

decomposed respectively in the axial direction and in the plane of the rotor. These components are calculated from geometric considerations using the normal and tangential forces according to the set of equations:

$$\begin{aligned} F_{ax} &= F_n \cos(\theta_{tot}) - F_{tg} \sin(\theta_{tot}) \\ F_{rot} &= F_n \sin(\theta_{tot}) + F_{tg}.\cos(\theta_{tot}) \end{aligned} \tag{6.2.3}$$

Once the induction factors have been derived, the local angle of attack is computed with

$$\alpha = \arctan\left(\frac{U(1-a)}{\Omega r(1+a')}\right) - \theta_{tot} \tag{6.2.4}$$

and the lift and drag forces are computed by inverting the set of equations :

$$\begin{aligned} F_n &= L.cos(\alpha) + D.sin(\alpha) \\ F_{tg} &= L.sin(\alpha) - D.cos(\alpha) \end{aligned} \tag{6.2.5}$$

Finally, the **lift and drag coefficient** are computed with

$$\begin{aligned} C_l &= \frac{L}{0.5\rho c V_{eff}^2} \\ C_d &= \frac{D}{0.5\rho c V_{eff}^2} \end{aligned} \tag{6.2.6}$$

where the **local effective velocity** is calculated including the induction factors according to:

$$V_{eff} = \sqrt{[\Omega r(1+a')]^2 + [U(1-a)]^2} \tag{6.2.7}$$

Considered MEXICO data

One must keep in mind that the angular velocity may influence the rotational augmentation, according to equation (6.1.1), and consequentially in all considered trials the **rotational speed** was approximately **424 rpm.** This is justified since the ultimate goal is to compare the model's results with the yawed flow trials from the MEXICO, and in all these trials the rotational velocity was set to 424 rpm. It is also important to mention that the trials considered have a wide **variety of wind tunnel speeds** and **pitch angles**. Hence the blades operate at a wide range of angles of attack.

Following the recommendations given in chapter 3, a visual inspection of the pressure distribution over each spanwise section was conducted for each considered trial, before taking it into account in the determination of the rotational augmentation.

Also, it is important to state that only the **25%** and **35% spanwise sections** were considered, since one expects the rotational effects not to be significant at the other more outboard radial stations.

The table below shows the trial cases considered and their most important characteristics:

Trial Nr	Pitch (deg)	Wind Speed (m/s)	Data at 25% span	Data at 35% span
92	-2.3	9.97	Accepted	Rejected
94	-2.3	18.05	Accepted	Rejected
96	-2.3	13.42	Accepted	Rejected
97	-2.3	14.05	Accepted	Rejected
99	-2.3	15.44	Accepted	Rejected
100	-2.3	15.91	Accepted	Rejected
101	-2.3	6.91	Accepted	Accepted
104	-2.3	11.04	Accepted	Rejected
107	-2.3	16.92	Accepted	Rejected
108	-2.3	19.02	Accepted	Rejected
109	-2.3	19.89	Accepted	Rejected
110	-2.3	22.01	Accepted	Rejected
114	-5.3	14.91	Accepted	Rejected
116	-5.3	18.03	Accepted	Rejected
118	-5.3	23.97	Accepted	Rejected
131	-3.3	18.07	Accepted	Rejected
133	-0.3	18.11	Accepted	Rejected
135	-4.3	23.98	Accepted	Rejected
136	-2.3	23.98	Accepted	Rejected
137	-1.3	23.98	Accepted	Rejected
238	-2.3	29.98	Accepted	Accepted
239	-2.3	26.06	Accepted	Accepted
240	-2.3	28.05	Accepted	Accepted
241	0.7	29.97	Accepted	Accepted
242	-5.3	29.97	Accepted	Accepted
243	-4.3	29.96	Accepted	Accepted
244	-3.3	29.98	Accepted	Accepted
246	-0.3	29.98	Accepted	Rejected
247	1.7	29.98	Accepted	Rejected

Table 6.2.1: Trials Considered in the Rotational Augmentation Investigation

The table above shows that for a very significant number of trials the pressure data obtained at the 35% span is considered to be unacceptable, since, as mentioned previously, very strange pressure distributions were registered over a considerable portion of the airfoil. For this reason, unfortunately the experimental investigation of the rotational augmentation effect will **only** be carried out at the **25% spanwise position**.

6.3) Results

Following the procedure described above, the lift coefficient dependency with the angle of attack at the 25% span of the MEXICO rotor was obtained; for comparison, the figure below also includes the 2D airfoil data, from [25]:

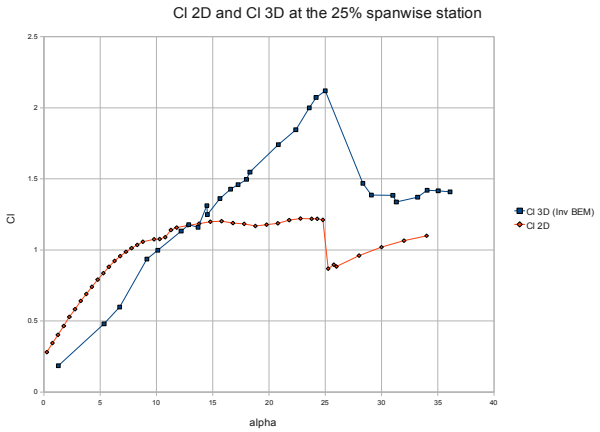

Figure 6.3 1: Cl2D and Cl3D obtained with the inverse BEM

Comparing the MEXICO data with the 2D curve one can clearly witness the rotational augmentation effect since the **maximum value of the lift coefficient** registered is **greater than 2**, and also because it takes place at an estimated angle of attack of 25 degrees.

One can also notice that at the lower angles of attack the values of the lift coefficient are underestimated with respect to the 2D data, or alternatively one can say that the angle of attack is overestimated; this could be explained by the fact that at lower wind speeds, and consequentially lower angles of attack, the axial induction factor may become large and the wind turbine may be heavily loaded, which means that expression (6.2.1) may not necessarily be verified. This fact could be overcome by introducing a turbulent wake correction in the BEM model. However the idea was to investigate the rotational augmentation, which occurs at high angles of attack, and so this discrepancy was not addressed further.

It is also interesting to dwell on the results obtained for the variation of the **tangential force coefficient** with the angle of attack; this quantity is defined similarly to (6.2.5), according to

$$C_{tg} = \frac{F_{Tg}}{0.5\,\rho\,c\,V_{eff}^2} \tag{6.3.1}$$

For comparison, the dependency of the **pitching moment coefficient**, C_m , with the angle of incidence, obtained in 2D conditions [25] is also shown in the plot below:

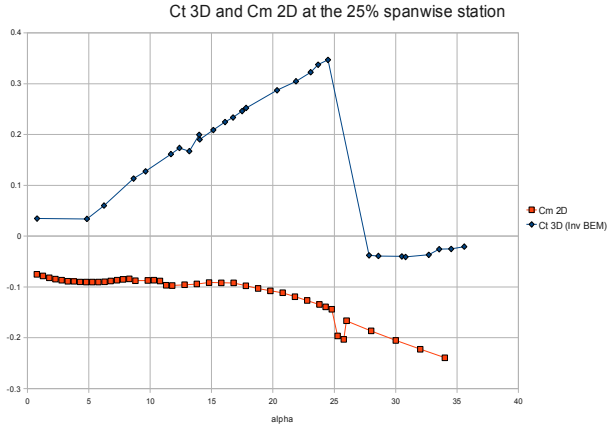

Figure 6.3 2: Cm2D and Ct3D obtained with the inverse BEM

Figures 6.3 1 and 6.3 2 show in the 2D case an abrupt load variation, at an **angle of attack of 25 degrees**; both the lift and the moment coefficient suddenly drop, which is indicative of **leading edge separation** occurrence.

More interestingly, analysing the angle of attack dependency of the **3D** force coefficients, and even though the rotational augmentation phenomenon is clearly visible, one can see that an **abrupt load variation** also takes place when the angle of incidence reaches **25 degrees**. Both the lift and the tangential force coefficient suddenly drop[8], hinting the occurrence of **leading edge separation**.

The observation that the angle of attack where leading edge separation occurs is unaffected by rotation for an inboard section of a rotating blade, despite the influence of rotational augmentation, is in no way to be taken as a general fact.

To be able to establish such a relation it would be necessary to test the hypothesis at different spanwise positions and with different airfoil sections. Unfortunately, as mentioned before, in the MEXICO only the 25% spanwise position is suitable for assessing the matter at hands; consequentially and also due to time constraints, it will not be addressed further.

Nevertheless, one can reason why such an event would take place by qualitatively considering the physics of the problem. As mentioned before, the rotational augmentation is brought upon by the spanwise flow component, which causes the pressure gradient over the upper surface of the airfoil to be less adverse. However, one can understand that this phenomenon will be more significant in the **aft region of the airfoil**, since the cross flow will be deflected by the Coriolis force and eventually be aligned with the local effective velocity. One can thus understand that this change in the pressure gradient acts to keep the flow attached further aft, or in other words that rotational effects delay stall by **postponing trailing edge separation**.

For thick airfoils, when occurring, **leading edge separation** usually takes place at much higher angles of attack than trailing edge separation. It is brought upon by the fact that the flow “cannot handle” the very adverse

[8] At high angles of attack, and as long as the flow remains attached, one expects significant suction in the leading edge area. This will have a positive contribution to the tangential force, according to the assumed convention. Consequentially, when the suction region ceases to exist, i.e. when leading edge separation occurs, the total tangential force is expected to decrease abruptly.

pressure gradient which is felt immediately downstream of the suction peak, characteristic of large incidence angles Consequentially flow separation takes place in chordwise positions close to the leading edge. In other words, this kind of separation is deeply related with the l**ocal flow conditions and airfoil geometry** present in the vicinity of the leading edge.

One should keep in mind that in wind turbine applications the flow can always be regarded as incompressible, and consequentially the information of the perturbations occurring in the aft region of the airfoil will be propagated upstream. This means that, in reality, trailing and leading edge separation are not completely independent. However, from the discussion above and minding the results obtained, one can argue that the two kinds of separation are **relatively distinct phenomena**. Accordingly, in this project it will be assumed that **leading edge separation always occurs at an angle of attack of 25 degrees**, in all MEXICO spanwise positions where the airfoil section is the DU91-W2-250.

6.4) Implemented Aerodynamic Coefficients

Lift Coefficient

Up to now the rotational augmentation present at the 25% spanwise station of the MEXICO rotor has been investigated, but one can understand that it is necessary to consider the rotational effects present in all inboard sections of the blade. Naturally, one expects a different amount of rotational augmentation to exist at different spanwise sections, and it is therefore essential to implement this radial dependency in the BEM code developed.

A number of modelling approaches, with a wide range of complexity, have been developed to predict the augmented force coefficients dependency of the angle of attack. In [41] an effort was conducted to compare the performance of six different stall delay models with experimental data from the NREL measurements, however a conclusion was not reached on which of the implemented approaches yielded the more accurate results.

According to [18], a simple correction from Snel yields quite good results for the augmented lift coefficient dependency with angle of attack; this approach was one of the methods considered in [41], and also since it performs at least as well as the other models considered in [41], it will be implemented in the current project. The correction for the augmented lift is expressed by:

$$C_{l,3D} = C_{l,2D} + 3\left(\frac{c}{r}\right)^2 \Delta C_l \tag{6.4.1}$$

where ΔC_l is the difference between the actual 2D lift coefficient and the potential value, which is given by:

$$C_{l,pot} = C_{l_0} + 2\pi\alpha \tag{6.4.2}$$

Where C_{l_0} represents the lift coefficient obtained when the angle of attack is zero. It is clear that if one uses expression 6.4.2 for very large angles of attack, it may yield unrealistically large lift coefficients, specially at the more inboard sections. To overcome this problem it is suggested in [41] to apply the correction up to an angle of attack of 30 degrees, after which the correction itself should be linearly decreased to 0 at an angle of attack of 90 degrees, resulting in a smoother transition in the application of the model. However, taking into account the discussion

presented previously on the leading edge separation occurrence, the lift coefficient augmentation correction will be applied up to an **angle of attack of 25 degrees**, after which the correction is linearly decreased to 0 at an angle of attack of 90 degrees.

The implemented lift coefficient angle of attack dependency for the inboard sections is shown in the graphic below, together with the 2D static data and the empirically determined lift coefficient values at the 25% spanwise section of the MEXICO rotor:

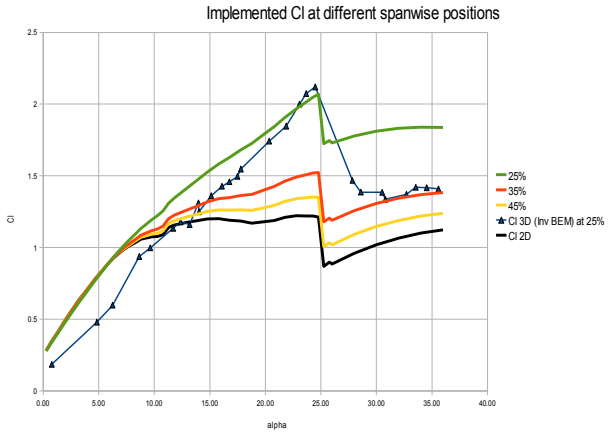

Figure 6.4 1: Implemented Cl dependency of angle of attack at different spanwise positions

As expected, the figure above shows that the more inboard the airfoil section is located, the more significant the rotational augmentation becomes, as the 3D lift coefficient grows further apart from the 2D values at the stations closer to the blade's root.

More interestingly, one can notice that **reasonable agreement** is found between the experimental data derived at the 25% spanwise position of the MEXICO rotor and the implemented correction, especially regarding the **maximum value of the lift coefficient**. For angles of attack beyond 25 degrees the agreement found is not so good, but since as mentioned before only data for the 25% spanwise section was available, no attempts were done to derive an expression for this portion of the lift coefficient curve, and the procedure recommended in [41] was followed.

It is also important to mention that the **correction** for the **rotational lift augmentation** was applied **only to a radial position of 1.125 m**, which corresponds to a relative radius of r/R=0.5. In the MEXICO rotor this radial position is located in the transition area between the DU91-W2-250 and the RISOE A1-21, and according to expression 6.4.2 the rotational augmentation at this station would, for the MEXICO blades, be given by:

$$C_{l,3D} = C_{l,2D} + 3\left(\frac{0.158}{1.115}\right)^2 \Delta C_l = C_{l,2D} + 0.06\,\Delta C_l$$

As such the expected rotational augmentation is very small for this, and more outboard, radial position. Consequentially, and also since it facilitates implementation, the application of the criterion mentioned above is justified.

Drag Coefficient

In [41] several modelling approaches of the rotational effects in the drag coefficient dependency with the angle of attack were considered and their performance compared with experimental data, but again there was not conclusive evidence that one of the tested model's performance was generally better.

In the present project it was chosen to use the simple model of Chaviaropoulos and Hansen [42], according to which the influence of the rotational effects in the drag coefficient is given by:

$$C_{d,3D} = C_{d,2D} + g_{C_d} \Delta C_d \tag{6.4.3}$$

where in this case ΔC_d is the difference between the 2D drag coefficient and the drag coefficient obtained when the angle of attack is zero. As for the scaling term in the equation above, it is given by

$$g_{C_d} = 2.2 \left(\frac{c}{r} \right) \cos^4(\theta_{tw})$$

where θ_{tw} represents the local twist angle. The twist comes into play because it is the angle between the rotation plane (and hence the Coriolis force) and the chord (onto which the favourable pressure gradient should be applied).

Minding expression 6.4.3 one can see that the **rotational correction acts to increase the drag** coefficient, when compared to the 2D case. This trend has been identified in experimental data [41], but however the physical mechanism that leads to an increased drag force in a rotating environment is not completely understood yet.

However, one can argue that the less adverse chordwise pressure gradient will have a stronger influence on the aft region of the airfoil section, since it is related with the spanwise flow component; this would mean that the decrease in the pressure over the aft region of the upper surface of the airfoil would have a considerable contribution to the drag. In other words, the pressure drag would be expected to increase because of the rotational effects. Especially at high angles of attack, the magnitude of the pressure drag is much larger than the viscous drag contribution, and so one can understand the trend imposed in equation 6.4.3.

Accordingly to what was done regarding the lift coefficient, the correction for the rotational effects on the drag coefficient was applied up to an **angle of attack of 25 degrees**, after which the correction itself is linearly decreased to 0 at an angle of attack of 90 degrees.

Also to maintain the coherence with the procedure taken for the lift coefficient, the drag correction was imposed for **spanwise positions** which had **relative radius smaller than 0.5** .

The implemented drag coefficient angle of attack dependency for the inboard sections is shown in below, along with the 2D static data and the empirically determined drag coefficient values at the 25% spanwise section of the MEXICO rotor:

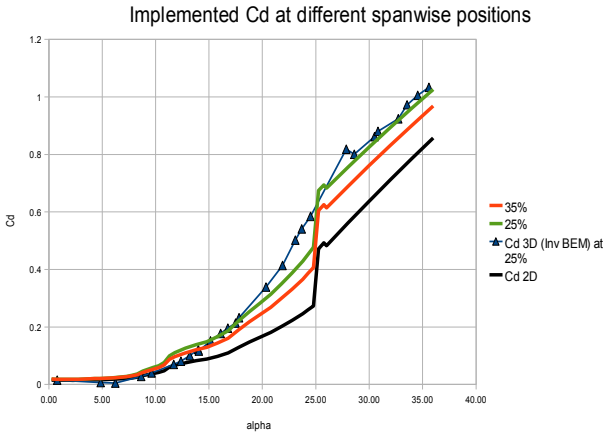

Figure 6.4 2: Implemented Cd dependency of angle of attack at different spanwise positions

Firstly, one should notice that there is a sudden increase of the drag coefficient values for an angle of attack of approximately 25 degrees, even though this is less noticeable in the empirically derived data. This occurrence is consistent with the assumption that leading edge separation takes place at such an incidence, since one would thus expect the suction area near the leading edge of the airfoil to abruptly decrease, thus increasing the drag coefficient.

Identically to what was seen for the lift coefficient, the more inboard the airfoil section is located the more significant the rotational augmentation will become, as the 3D drag coefficient grows further apart from the 2D values at the stations closer to the blade's root.

It can also be seen that the agreement found between the experimental data derived at the 25% spanwise position of the MEXICO rotor and the implemented correction is good. Introducing the rotational correction yields better agreement with empirical data then when 2D drag coefficient data is considered, and consequentially the application of the rotational correction mentioned above is justified. Unfortunately consistent MEXICO data was not available for other inboard spanwise sections, impeding other test cases to be carried out.

6.5) Conclusions and Recommendations

In the present section the influence of rotational augmentation on the aerodynamic coefficients was addressed, and it was possible to draw the following conclusions:

- The dependency of the experimental aerodynamic coefficients with angle of attack at the 25% spanwise station of the MEXICO rotor was determined; this was done by considering several axial flow data points and using an inverse BEM method. The MEXICO results from the 35% spanwise station were not taken into account since in most trials there was indication of pressure sensor malfunction.

- Results indicate that the angle of attack at which the leading edge separation occurs seems to be unaffected by rotational augmentation; accordingly it was assumed that this critical angle of attack remains constant for all rotationally augmented spanwise sections.
- Empirical corrected for the lift and drag 3D coefficients have been compared with results from the MEXICO, and reasonable to good agreement was found. These corrections should thus be implemented in the BEM model, up to a relative radius of 0.5.

7) Results of the BEM code including the Dynamic Stall model and rotational effects

Rotational augmentation of the static airfoil coefficients has been included in the BEM code, and the DS model has also been implemented in the BEM iteration loop. The objective of this chapter is thus to compare the results obtained with the complete model against the MEXICO data at yaw-misaligned configurations, when large wind tunnel speeds are imposed.

The chapter starts by assessing the convergence of the implemented model, and in section 7.2 the MEXICO data used for comparison is addressed. Section 7.3 shows the results obtained and discusses the trends observed, and finally the conclusions drawn in this chapter are stated in section 7.4.

7.1) Model Convergence

Because one wishes to test the implemented code's performance when DS phenomena are expected to occur, it was chosen to impose in all considered test cases a high wind speed, **U=24m/s,** and a relatively large yaw angle, **β= 30 deg**. Also, since the BEM model will subsequently be compared with MEXICO data, the rotational speed and pitch angle match the MEXICO's yawed flow data points' settings, i.e. **Ω=424 rpm** and **θ=-2.3 deg**.

Number of elements in the spanwise direction

Using an **azimuthal spacing** of **10 degrees**, the complete BEM code was run considering different number of elements in the spanwise direction. The results below show the variation of the normal force coefficient obtained at **all spanwise stations**, at an azimuthal position of 0 degrees. It was chosen to plot the azimuthal position of 0 deg since it displayed the larger dependency of the number of spanwise elements; results obtained for other azimuthal coordinates are included in appendix E.

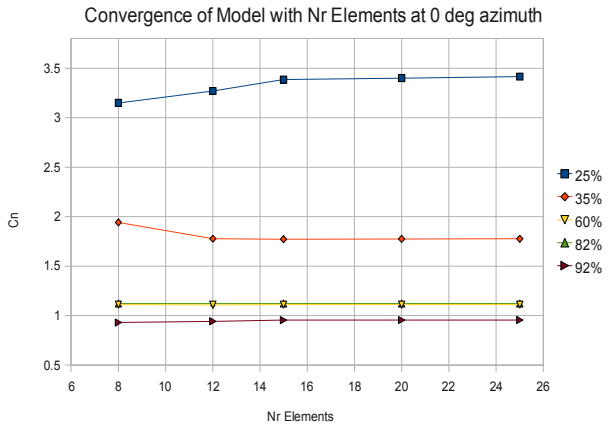

Figure 7.1 1: Cn variation with spanwise number of elements at 0 deg azimuth

Minding the figure above it is clear that, for the inboard spanwise stations, the number of elements considered has an influence on the normal force coefficient obtained. One can also see that increasing the **number of elements** in the spanwise direction beyond **15** does not yield a significant difference in the value of the force coefficient obtained.

For the other spanwise stations, the results obtained show that the number of elements considered does not have a significant influence on the normal force coefficient obtained.

Azimuthal Angular Increment

Using **15 elements in the spanwise direction**, the BEM code was run considering different azimuthal angular increments. The results below show the variation of the normal force coefficient obtained at **all spanwise stations**, at an azimuthal position of 120 degrees.

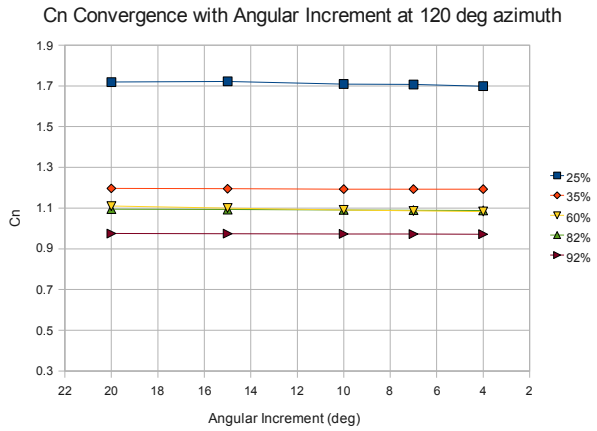

Figure 7.1 2: Cn variation with azimuthal increment at 120 deg azimuth

It was chosen to plot the azimuthal position of 120 degrees since it displayed the larger dependency of the azimuthal increment; results obtained for other azimuthal coordinates are included in appendix E.

Firstly one should notice that, for all spanwise stations, the angular increment considered does not have a

very significant influence on the normal force coefficient obtained.

The spanwise section with a greater dependency of the azimuthal discretization is again the most inboard station. Still, one can argue that decreasing the **azimuthal angular increment** beyond **10 degrees** does not yield a significant difference in the value of the force coefficient obtained.

Number of Revolutions

One can say that the DS model has "memory", in the sense that it requires the airfoil aerodynamic parameters' history to compute the instantaneous loads. However, these aerodynamic parameters (degree of separation, vortex lift, etc.) must be initially prescribed; since it is assumed that in the first time instant the flow is fully attached and no circulation has been shed, one can understand that some iteration time must be allowed before the model reaches a definite solution.

Considering an azimuthal angular increment of 10 degrees and 15 elements in the spanwise direction, the following evolution in time of the normal force coefficients was obtained for each spanwise section:

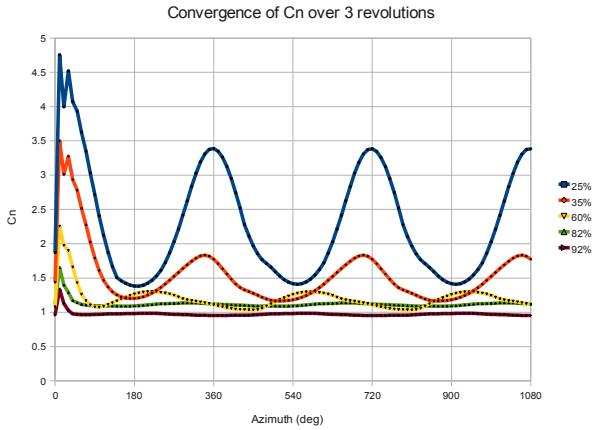

Figure 7.1 3: Cn variation with azimuth angle

From the figure above one can see that after one revolution (360 deg), the results obtained seem to no longer be influenced by the initial condition imposed; this is based on fact that, for all spanwise stations, the normal coefficient variation over the second revolution (from 360 to 720 deg) is indistinguishable from the curve corresponding to the third revolution (from 720 to 1080 deg).

7.2) Comparison with MEXICO data

The results obtained with the complete BEM code are now compared with the data from MEXICO trials. With the purpose of investigating the concrete influence of the Beddoes-Leishman method, the **results obtained without using the DS model are also shown**.

Keeping in mind the discussion of the previous section, it was chosen to run the model imposing an

azimuthal discretization of 10 degrees and **15 elements in the spanwise direction**. It should also be mentioned that the results displayed were obtained over the third revolution (from 720 to 1080 deg).

The comparison between the MEXICO data and the results of the model is done through the **normal force coefficient**, since this dimensionless quantity is of great importance to calculate the loads acting on the rotor's blades. Another reason to use C_n to assess the model's performance is that it directly available from the MEXICO measurements, since it does not depend on the angle of attack. The results display the azimuthal variation of the normal force coefficient quantity, as well the $C_n \ vs \ \alpha$ loops, where the angles of attack obtained with the BEM code were used also to plot the MEXICO data.

Before the results are presented, it is useful to remind the reader that the MEXICO blades were rotating clockwise, and that in the yawed flow trials the wind was blowing from the left hand side, when looking in line with the rotor's axis from the upwind side. Referring to figure 2.2 2 , this means that the blades were rotating in the positive direction of ψ, and that the yaw misalignment was also positive, $\beta>0$.

The advance/retreating blade effect present in this configuration will thus impose a minimum angle of attack at the vertically downward azimuthal position, $\psi = 180\, deg \Rightarrow \alpha_{min}$, and maximum incidence at the vertically upward angular coordinate, $\psi = 0\, deg \Rightarrow \alpha_{max}$. Since this effect will be dominant at the inboard stations when large wind speeds are considered, one comes the conclusion that the **upstroke** of the cycle, i.e. the period when the angle of attack is increasing, corresponds to **azimuthal positions from 180 to 360 deg**. By analogy, the **downstroke** of the cycle, i.e. the period when the angle of attack is decreasing, corresponds to **azimuthal positions from 0 to 180 deg**.

Considered MEXICO data

It was mentioned before that the MEXICO's pressure sensors at the 35% span often seemed to be malfunctioning, since very irregular pressure distributions have been obtained at relative chord positions from 40 to 70%. However, at high angles of attack one might expect small pressure differences between 40 and 70% relative chord positions, given the fact that significant trailing edge separation is most likely present.

Since experimental data also showed this trend, it was chosen to interpolate the value of the pressure between the sensors which were not malfunctioning; this allows the model's performance to be compared against MEXICO data also at the 35% spanwise station. The experimental pressure distribution obtained at this radial section for the relevant MEXICO data points is shown in appendix F.

Dynamic stall phenomena are expected to occur mostly at **inboard sections**, and consequentially emphasis is given at the 25 and 35% spanwise stations. Other radial sections will also be addressed. Naturally, the considered wind tunnel speeds will now be large, with the purpose of imposing large angles of attack on the airfoil sections. The MEXICO data points considered are shown in the table below, together with the spanwise sections analysed:

Trial	U (m/s)	β (deg)	θ (deg)	25% span	35% span	60% span	82% span
152	18	30	-2.3	yes	yes	no	no
153	24	30	-2.3	yes	yes	yes	yes
160	24	15	-2.3	yes	yes	no	no
167	24	45	-2.3	yes	yes	no	no

Table 7.2.1 - MEXICO data points and spanwise positions used to compare the model against

7.3) Results and Discussion

U=18 m/s

The results obtained at this wind tunnel speed are now displayed, with the purpose of assessing the model's performance when **little stall penetration** is present. The normal force coefficient variation is shown for the inboard spanwise sections, imposing a **yaw angle of 30 deg**:

25 % Spanwise section

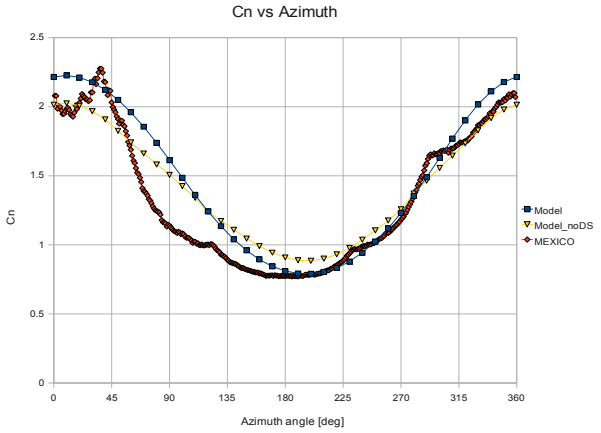

Figure 7.3 1: Cn variation with azimuth for U=18 m/s and β=30 deg at 25% span

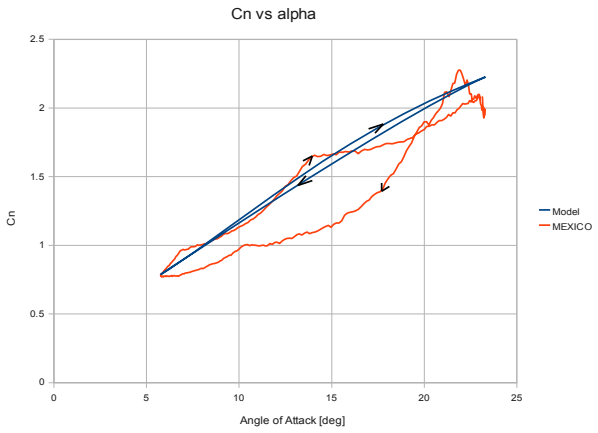

Figure 7.3 2: Cn variation with alpha for U=18 m/s and β=30 deg at 25% span

At this spanwise section good agreement is found between the predicted and experimental azimuthal variation of the normal force coefficient. It is not clear however that including the DS model improves the load prediction. As for the $C_n vs\ \alpha$ loop, the figure above shows that the predicted loading yields a somewhat narrower curve than what was measured in the MEXICO trial, even though both predicted and experimental curves are in the clockwise direction.

35 % Spanwise section

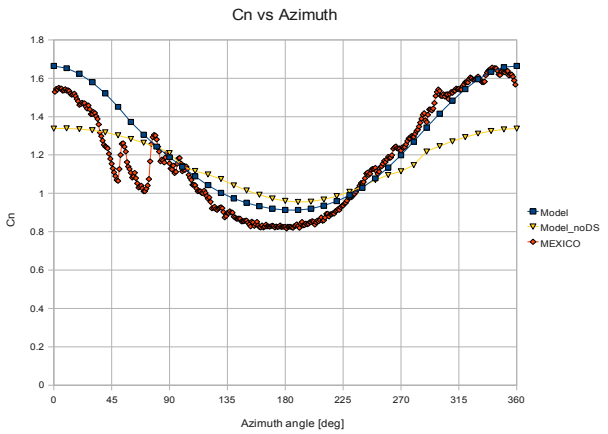

Figure 7.3 4: Cn variation with azimuth for U=18 m/s and β=30 deg at 35% span

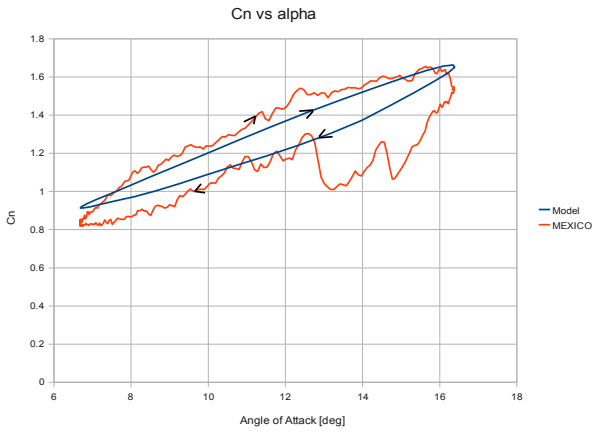

Figure 7.3 3: Cn variation with alpha for U=18 m/s and β=30 deg at 35% span

For this spanwise station reasonable to good agreement was found between the predicted and the experimental loading. Including the DS model clearly improves the load prediction capability, particularly at the 0 deg azimuthal position, where larger angles of attack are expected. As for the $C_n vs \alpha$ loop, reasonable to good agreement was also found, and one can see both predicted and experimental curves are in the clockwise direction.

U=24 m/s

By increasing the wind tunnel speed one expects **DS phenomena to play a more important role**. The normal force coefficient's variation is again shown for the inboard spanwise sections, imposing a **yaw angle of 30 deg**:

25 % Spanwise section

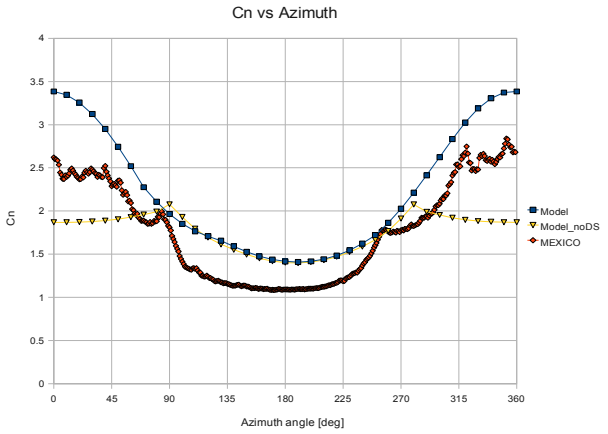

Figure 7.3 5: Cn variation with azimuth for U=24 m/s and β=30 deg at 25% span

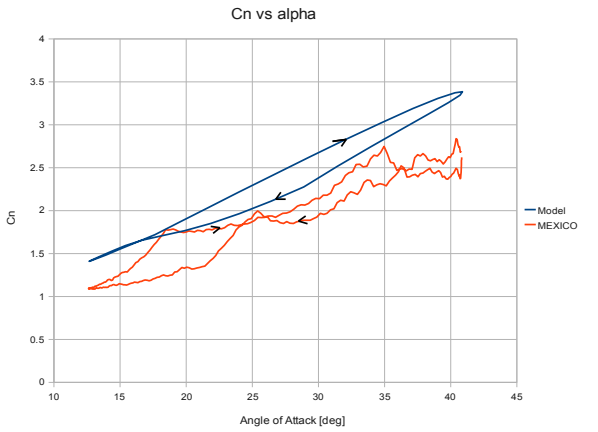

Figure 7.3 6: Cn variation with alpha for U=24 m/s and β=30 deg at 25% span

At this spanwise station one can clearly see that stall is present. Accordingly, when using the BEM code without the DS model, the agreement between calculations and measurements is not good. When including the DS model the load prediction capability is improved.

The magnitude of the normal force coefficient is somewhat overpredicted, even though the trend is well captured, which can also be seen in the $C_n vs\, \alpha$ loop.

35 % Spanwise section

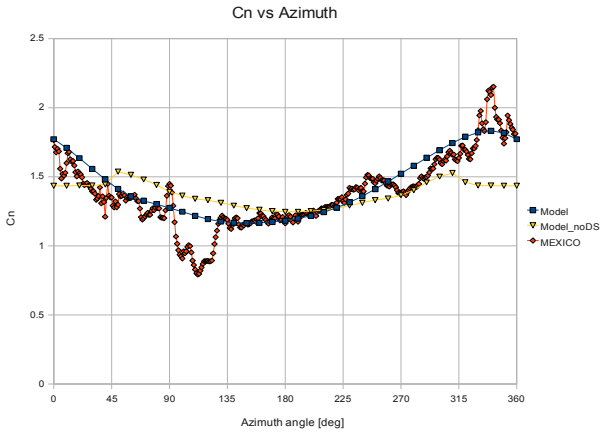

Figure 7.3 7: Cn variation with azimuth for U=24 m/s and β=30 deg at 35% span

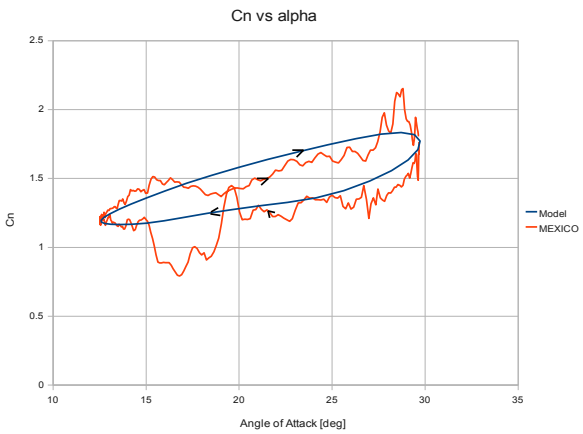

Figure 7.3 8: Cn variation with alpha for U=24 m/s and β=30 deg at 35% span

For this spanwise agreement good agreement was found between the predicted and the measured loading. Including the DS model clearly improves the results when compared to the static model. One can also notice that higher frequency components are present in the experimental results, which is coherent with what one may expect from a dynamically stalled airfoil.

Influence of the Yaw Error

The results obtained for the **yaw errors of 15 and 45 degrees** at the **inboard stations** will now be displayed. The **wind speed is set to 24 m/s** , since one expects more stall penetration at this velocity and also since the axial induction factor is expected to be smaller, meaning that uncertainties arising from the yaw BEM model itself are thus made less important.

β=15 deg

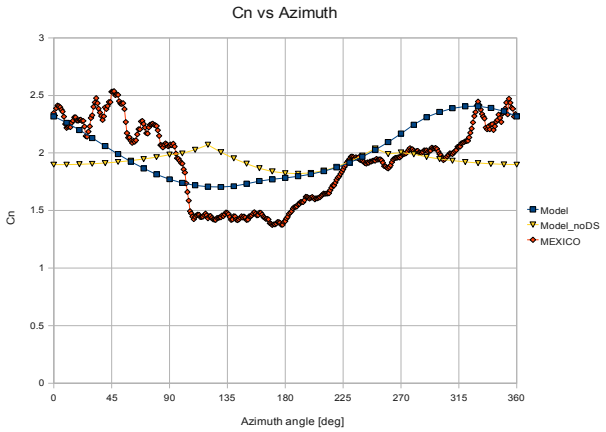

Figure 7.3 10: Cn variation with azimuth for U=24 m/s and β=15 deg at 25% span

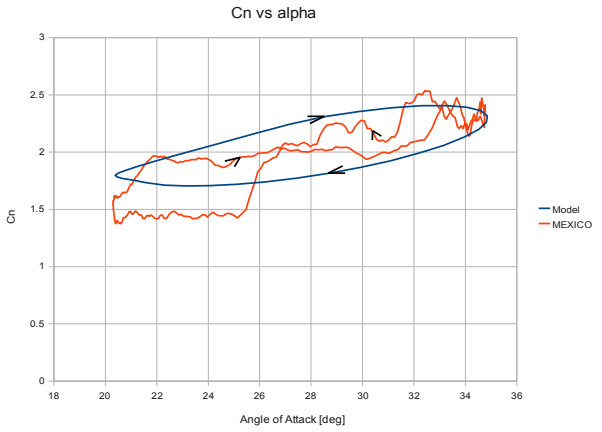

Figure 7.3 9: Cn variation with alpha for U=24 m/s and β=15 deg at 25% span

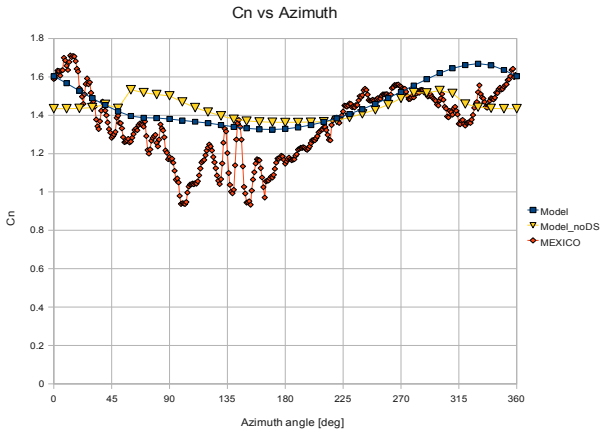

Figure 7.3 11: Cn variation with azimuth for U=24 m/s and β=15 deg at 35% span

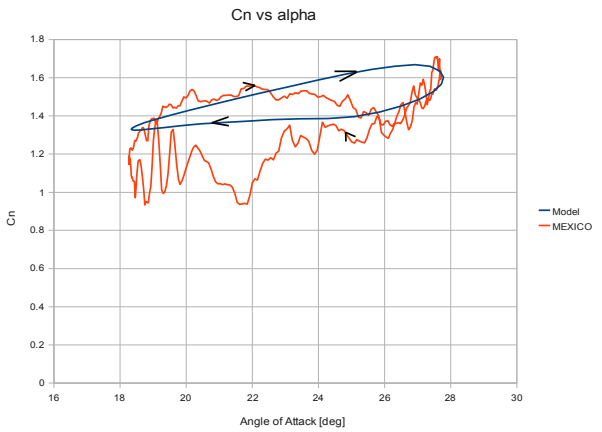

Figure 7.3 12: Cn variation with alpha for U=24 m/s and β=15 deg at 35% span

At this yaw-misalignment angle reasonable agreement was found between experiments and the BEM including the DS model. When the DS model is not used, the agreement seems to be somewhat poorer.

Minding the $C_n vs\ \alpha$ curves, one can see that the direction of the loops is well predicted. One can also notice that the loop obtained with the model at the 25% spanwise station is somewhat wider than for the 30º yaw misalignment.

β=45 deg

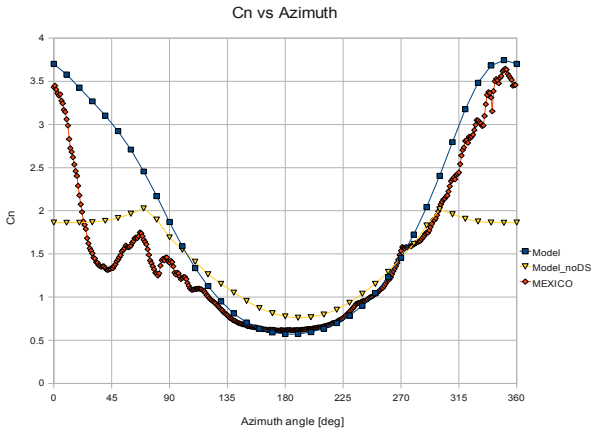

Figure 7.3 13: Cn variation with azimuth for U=24 m/s and β=45 deg at 25% span

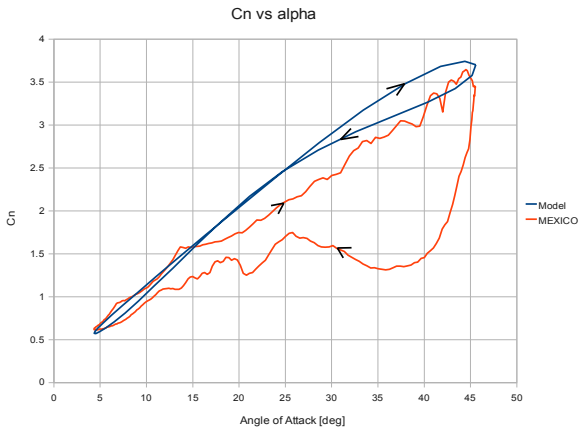

Figure 7.3 14: Cn variation with alpha for U=24 m/s and β=45 deg at 25% span

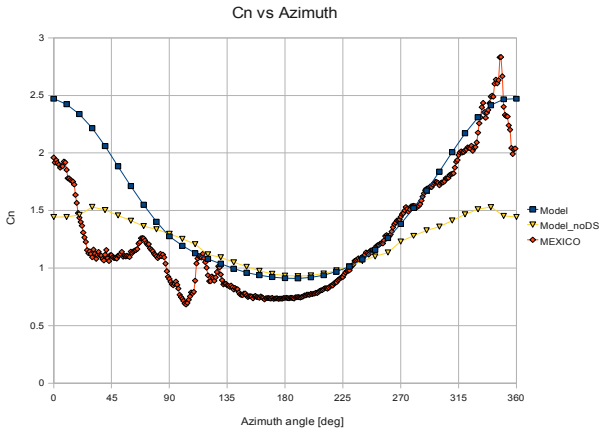

Figure 7.3 16: Cn variation with azimuth for U=24 m/s and β=45 deg at 35% span

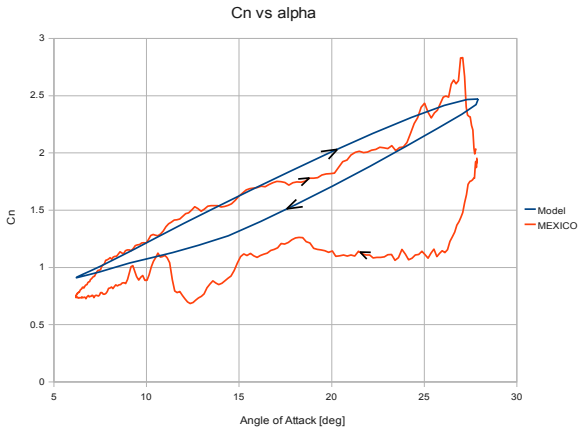

Figure 7.3 15: Cn variation with alpha for U=24 m/s and β=45 deg at 35% span

A yaw misalignment of 45 deg will impose a wider range of angles of attack of operation and consequentially (dynamic) stall will be necessarily present. Accordingly, using the BEM model without the DS model yields a poor agreement with the experimental data. When including the Beddoes-Leishman model good agreement was found between the predicted load magnitude and the measured results.

As for the $C_n vs \alpha$ loops, one can see that poor agreement is found between the modelled and experimental results, especially concerning the downstroke of the oscillation. The measured data show an abrupt decay of the normal force coefficient at the highest angle of attack, which is consistent with significant flow separation. However the implemented model does not capture this trend.

One should mention that in the upstroke of the motion the predicted loading agrees quite well with the MEXICO data, for both inboard spanwise sections.

Having the ***1P*** frequency as reference, the reduced frequency of excitation depends only on the radial position; however one can argue that the actual unsteadiness of the flow is characterized by the time derivative of the angle of attack.

If the yaw error is larger the angle of attack amplitude over a revolution will be larger, and accordingly the AOA time derivative will also increase. Since the DS model uses the AOA time derivative as input, it will effectively "see" the larger yaw error as an increased unsteadiness. This will mean that, over an oscillation, which in the present case corresponds to a blade revolution, the vortex lift component will decay more slowly, and will persist having a considerable contribution over the downstroke of the movement. This may explain why the $C_n vs\ \alpha$ loops are so narrow.

In appendix G the results obtained with the DS model in a 2D situation at very high reduced frequencies are shown (k>0.12). Each of the components of the normal force coefficient are represented, so that one can understand what the computational approach actually models.

Results at other Spanwise stations

At more outer spanwise stations the amplitude of the angle of attack oscillations over a revolution will necessarily be smaller, and the angles of attack will also be considerably smaller than at the 25 and 35% spanwise stations. Thus, one expects the dynamic stall model to be of less importance in predicting the loads at these sections. Still, the results obtained at the **60** and **82% spanwise sections** will now be shown, when considering a **wind speed of 24 m/s** and a **yaw error of 30 degrees**.

60 % Spanwise section

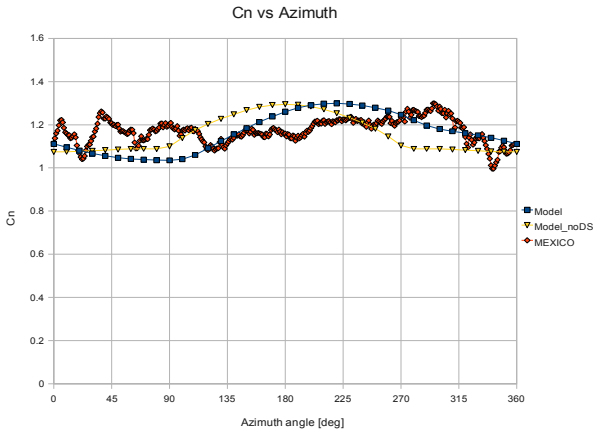

Figure 7.3 17: Cn variation with Azimuth for U=24 m/s and β=30 deg at 60% span

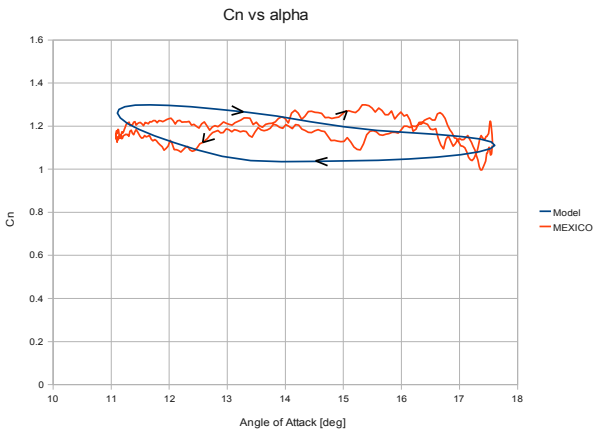

Figure 7.3 18: Cn variation with alpha for U=24 m/s and β=30 deg at 60% span

At this spanwise section reasonable to good agreement is found between the measured and predicted loads, both in terms of magnitude and regarding the $C_n vs\ \alpha$ loop. Minding the figures above one can also say that including the DS model slightly improves the results obtained.

82 % Spanwise section

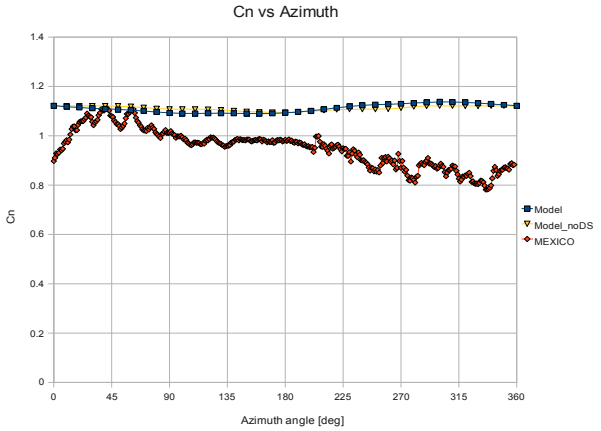

Figure 7.3 19: Cn variation with Azimuth for U=24 m/s and β=30 deg at 82% span

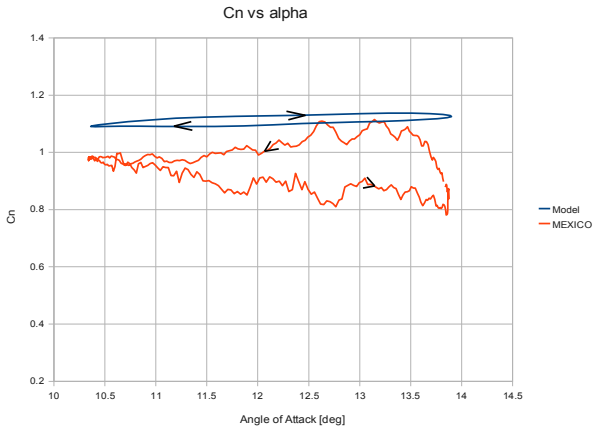

Figure 7.3 20: Cn variation with alpha for U=24 m/s and β=30 deg at 82% span

Minding the figures above it is clear that the DS model has very little influence on the results obtained with the BEM model; this is understandable since at this spanwise section each revolution imposes a small range of angles of attack and a low reduced frequency. Comparing the experimental results with the implemented model, it is possible to say that the normal force coefficient is somewhat overpredicted.

In the $C_n vs\, \alpha$ curves one can see that the predicted loops are in the opposite direction of experimental data.

Quantitative Analysis

With the objective of quantitatively assessing the performance of the implemented calculation method the **average relative error** in the **normal force coefficient** was computed for the BEM code including the DS model. The magnitude of the error was calculated by averaging the relative error of model results over a revolution and assuming the MEXICO data to be the exact solution, similarly to what was done in chapter 4.

The expression used to compute the average relative error in the normal force coefficient at each spanwise station and MEXICO trial is repeated here for convenience:

$$\varepsilon_{Cn,\,avg} = \frac{1}{360}\sum_{\psi=1}^{360} \frac{\left|C_{n,\,Model}(\psi) - C_{n,\,MEXICO}(\psi)\right|}{C_{n,\,MEXICO}(\psi)}$$

The results obtained for the considered trials are shown below, where the **relative error** in the normal coefficient averaged over the azimuth is **shown in percentage**. The average of the error obtained at each trial is displayed in the last row:

Trial	U (m/s)	β (deg)	25% span	35% span	60% span	82% span
152	18	30	12.1	8.1	12.3	10.3
153	24	30	25.4	7.6	6.5	17.9
160	24	15	12.3	11.1	9.9	14.0
167	24	45	25.1	24.0	14.5	6.4
Average	**-**	**-**	**18.7**	**12.7**	**11.6**	**12.2**

Table 7.3.1: Relative error in Cn averaged over a revolution

From the table one can see that the average error in the predicted normal force coefficient is approximately **12%** , except for the 25% spanwise station. It was mentioned before that the agreement found in the downstroke of the motion at the more inboard stations was not always satisfactory. Particularly at large yaw angles, the predicted C_n values substantially differ from the experimental data when considering azimuthal positions from 0 to 180 deg, which explains the relatively large average error in the normal force coefficient found at these stations.

However, the figures included before show good agreement between the predicted and experimental loading during the upstroke of the movement, even when large yaw misalignments are imposed. To quantify this trend, and also since the extreme loads occurring over a revolution are important in assessing the blade's robustness and fatigue resistance, the **relative error** in the **maximum normal force coefficient** over a revolution was computed, according to:

$$\varepsilon_{Cn,MAX} = \frac{\left| C_{n,MEXICO,MAX} - C_{n,Model,MAX} \right|}{C_{n,MEXICO,MAX}} \tag{7.3.1}$$

The results obtained for the considered trials are shown below, where the **relative error** in the maximum normal coefficient is **shown in percentage**. The average of the error obtained at each trial is displayed in the last row:

Trial	U (m/s)	β (deg)	25% span	35% span	60% span	82% span
152	18	30	2.0	0.2	9.9	5.9
153	24	30	19.1	15.0	0.1	2.2
160	24	15	5.0	2.4	14.9	1.1
167	24	45	2.5	12.8	13.5	4.2
Average	**-**	**-**	**7.2**	**7.6**	**9.6**	**3.4**

Table 7.3.2: Relative error in Maximum Cn over a revolution

The table shows that good agreement was obtained for the maximum normal force coefficient over a revolution, since the average error in the considered trial is below **10%.** Specifically regarding the inboard sections, where the DS model will have a greater influence, one can say that the implemented code is capable of predicting the load magnitude occurring over a revolution, with an average error of approximately **7%**.

7.4) General Remarks and Conclusions

Minding the results obtained and the discussion above, one can come to the following conclusions:

- The variation of the normal force coefficient with the azimuth angle was studied, with emphasis given at inboard spanwise stations. $C_n vs\ \alpha$ loops have also been plotted, using the angle of attack from the BEM code. Generally speaking reasonable to good agreement was found between the predicted loading and the MEXICO data.
- Including the DS model in the BEM code generally improves the load prediction capability when compared to the static BEM, especially when large angles of attack are imposed.
- Specifically when considering large yaw-misalignments the agreement found in the $C_n vs\ \alpha$ loops is poor; in the downstroke motion measurements seem to indicate that significant separation occurs, denoted by an abrupt decay in the normal force coefficent while the implemented model does not predict this trend. However, quite good agreement was found in the upstroke motion, and consequentially the amplitude of the loading over a revolution is well predicted.
- As for the other spanwise sections, reasonable to good agreement was also found between the predicted and experimental loads. However, over a revolution the imposed range of angles of attack will be smaller, and the reduced frequency will also be decreased, and consequentially including the DS brings only a slight improvement to the load predicting capability of the model at more outboard stations.
- The average error in the predicted loads over a revolution is approximately 12%, except for the 25% spanwise station. However, the predicted maximum normal force coefficient occurring over a revolution was within 10% of the measured values. Specifically considering the inboard stations, where the DS influence is larger, the accuracy obtained in predicting the maximum C_n was approximately 7%.
- In the $C_n vs\ \alpha$ loops the direction of motion was indicated with arrows, and results show that the implemented model is able to capture the trends displayed in the experimental results, except for the 82% spanwise section.

As a final remark, one should always bare in mind that the DS model is of a semi-empirical nature, and was developed for a 2D situation, with the data being taken from 2D static conditions. In the present case, the static data given as input to the dynamic stall model has a 3D dependency, due to the rotational augmentation, but one must have present that this $C_n(\alpha)$ characteristic was derived in steady conditions, from axial flow trials.

However, these two phenomena, rotational augmentation and dynamic stall, are intrinsically related, since they are part of the boundary layer flow around each profile; consequentially their influence on the total loading taking place in wind turbine's airfoil section is very complex to describe, and by superimposing their effects, as was done in the present implementation, one can only expect to approximate the actual loading to an engineering level.

8) Conclusions and Recommendations

8.1) Conclusions

The present thesis developed a BEM code for a yaw-misaligned turbine, which was validated using MEXICO data obtained at moderately high wind tunnel speeds. Posteriorly the Beddoes-Leishman DS model was adapted to the wind turbine framework and validated against 2D wind tunnel aerodynamic data from the OSU. Finally the DS model was implemented in the BEM code and the results of the complete model were compared with the MEXICO data obtained at large wind tunnel speeds. The MEXICO data had to be pre-processed in order to be used for validation.

The most important conclusions drawn in this assignment are now stated:

- Regarding the **MEXICO data**, often unusual pressure distributions have been found at the inboard stations. At the 25% spanwise station a pressure sensor consistently showed odd readings and consequentially it was not considered in the computation of the sectional forces. In some MEXICO data points the pressure distribution at the 35% station was also very atypical, indicating some sensor malfunction in the aft region of the airfoil section. For this reason, before any force calculation was performed at this spanwise section the pressure distribution obtained was visually inspected for each data point.
- As for the other spanwise sections, the pressure distributions found in the MEXICO data are coherent and yield smooth curves, and thus were considered reliable to compute aerodynamic forces from.

- **Two BEM methods** were implemented and tested against MEXICO data. Relatively high wind tunnel speeds were chosen to perform the validation, since little separation is expected to occur in such conditions. Comparing both BEM models it was clear that the 'Empirical BEM' yielded the best agreement with experimental data, and consequentially it was selected to implement the DS model.

- The **Beddoes-Leishman DS model** was successfully implemented and results were compared against unsteady 2D data experimental data; generally a good agreement was found.
- The DS model was adapted to consider thick airfoil sections by implementing different LE stall criteria. From the methods tested, the $C_{N,MAX}$ criterion clearly yields better agreement with measurements and consequentially it was selected for subsequent computations.
- 2D wind tunnel experimental data indicated that even when very thick airfoils are considered LE stall may occur. Consequentially it seems unrealistic to disregard LE separation in HAWT application profiles simply because the airfoils are thick.

- Regarding **rotational augmentation**, empirical corrections for the lift and drag 3D coefficients have been compared with results from the MEXICO using an inverse local BEM approach, and reasonable to good agreement was found. These corrections have thus been implemented in the BEM model, up to a relative radius of 0.5.
- Results indicate that the angle of attack at which the leading edge separation occurs seems to be unaffected by rotational augmentation; accordingly it was assumed that this critical angle of attack remains constant for all rotationally augmented spanwise sections.

- The **DS model was implemented in the BEM code**, and the predicted loads have been compared with the MEXICO data obtained at high wind tunnel speeds in yawed configuration. Generally speaking, reasonable to good agreement was found, and it was also clear that including the DS model improved the load predicting capability when compared to the BEM code using static aerodynamic airfoil coefficients.
- Particularly at large yaw angles, the model did not capture the experimental trend in the downstroke motion in a satisfactory way. This is thought to be related with the increased unsteadiness brought upon by large yaw misalignments which the DS model "sees" as an increased reduced frequency.
- Still, the loading during the upstroke of the motion was quite well predicted by the model. At the inboard stations, and even when large yaw error were considered, the maximum value of C_N over a revolution obtained with the model was within 8% of experimental results.

- As a **final remark** it should be noted that rotational augmentation and DS are complex phenomena which are intrinsically related, but their effects have been superimposed in the current model. Still, the results indicate that, even though the experimental trends were not always captured, the **magnitude of the loading amplitude** occurring over a revolution in a yawed configuration at high wind speeds was reasonably well predicted. This is important especially for blade fatigue calculations and is an encouraging result.

8.2) Recommendations

Throughout this research there were several topics that captured the attention of the author but which unfortunately there was no time to pursue further. The most important are now mentioned:

- Results from the MEXICO indicate that, for the 25% span, LE stall is not affected by rotational augmentation. Even though this phenomenon was to some degree justified in the current document and can be explained, further experimental validation is required to confirm this hypothesis.

- Naturally, it would also be very interesting to implement other DS model in the BEM code and assess their performance. This procedure could start by considering the 3 other approaches highlighted before.
- Regarding the DS model implemented in this assignment, one could think of different criteria to denote the LE separation occurrence. Since the criterion used seems to predict LE stall slightly sooner than experiments show, it could be worthwhile to take the critical C_N as the potential normal force coefficient one obtains when using the angle of attack at which the maximum C_N occurs.
- In yawed operation, the reduced frequency an airfoil section is working at is usually estimated using the 1P as excitation source. However one can argue that the local degree of unsteadiness is related with the time derivative of the angle of attack, which is related also with the yaw angle and wind speed magnitude. DS models could thus be validated experimentally for very high reduced frequencies, which might occur when large yaw misalignments are present.

9) References

[1] – Snel, H. and Schepers, J.G, *'Engineering models for dynamic inflow phenomena'*, Journal of Wind Engineering and Industrial Aerodynamics, 39, 1992, pp 267-281

[2] – Leishman, J. *'Principles of Helicopter Aerodynamics'*, Cambridge University Press, chap 9, 2006 .

[3] – Tan, C. and Carr, L. '*The AFDD Int. Dynamic Stall Workshop on Correlation of Dynamic Stall Models with 3-D Dynamic Stall Data'*, NASA TM-110375, USAATCOM TR-96-A-009, 1996.

[4] – Snel, H., Houwink, R., van Bussel, G., Bruining, A., *'Sectional Prediction of 3D Effects for Stalled Flow on Rotating Blades and Comparison with Measurements*', Proceedings of the European Community Wind Energy Conference, Lübeck-Travemünde, Germany, 8-12 March 1993, pp. 395-399

[5] – Rapin, M. and Ortun, B., *'3D rotational correction in ONERA Aeroelastic predictions of NREL wind Turbine'*, 45th AIAA Aerospace Sciences Meeting and Exhibit, 2007

[6] - Snel, H., Houwink, R., Bosschers, J., *'Sectional prediction of lift coefficient on rotating wind turbine blades in stall'*,ECN-C-93-052, 1994

[7] – Ekaterinis, J., Srinivasan, G. and McCroskey, W., *'Present Capabilities of Predicting Two-Dimensional Dynamic Stall'*, AGARD CP-552, 1994

[8] – Srinivnasan, G., Ekaterinas, J., and McCroskey, W.,*'Dynamic Stall of an Oscillating Wing Part 1: Evaluation of Turbulence Models'*, Paper 93-3403, AIAA 11th Applied Aerodynamics Conference, 1993

[9] – Carta, F., Casellini, L., Archidiacono, P., and Elman, H., *'Analytical Study of Helicopter Rotor Stall Flutter'*, 26th Annual Forum of the American Helicopter Society, 1970

[10] – Bielawa, R., *'Synthesized Unsteady Airfoil Data with Applications to Stall Flutter Calculations'*, 31st Annual Forum of the American Helicopter Society, 1975

[11] – Gormont, R., *'A Mathematical Model of Unsteady Aerodynamics and Radial Flow for Application to Helicopter Rotors'*, USAAVLABS TR 72-67, 1973

[12] – Beddoes, T., *'A Synthesis of Unsteady Aerodynamic Effects including stall Hysteresis'*, *Vertica* 1, pp. 113/123, 1976

[13] – Beddoes,T.S., *'Onset of Leading Edge Separation Effects Under Dynamic Conditions and Low Mach Number'*, Proceedings of the 34th Annual Forum of the American Helicopter Society, 1978

[14] – Gangwani, S., *'Synthesized Airfoil Data Method for Prediction of Dynamic Stall and Unsteady Airloads'*, *Vertica* 8, pp93-118, 1984

[15] – Johnson, W., *'Comparison of Three Methods for Calculation of Helicopter Rotor Blade Loading and Stresses due to Stall'*, NASA TN D-7833, 1974

[16] – Leishman, J. & Beddoes, T.,*'A semi-empirical model for dynamic stall'*, Journal of the American Helicopter Society, vol 34,1989.

[17] – Truong, V., *'Prediction of Helicopter Rotor Airloads Based on Physical Modelling of 3D Unsteady Aerodynamics'*, 22nd European Rotorcraft Forum, 1996

[18] – Burton,T., Sharpe,D., Jenkins,N. and Bossanyi,E., *'Wind Energy Handbook',* Wiley, 2001.

[19] – Larsen, J., Nielsen, S. and Krenk, S., *'Dynamic stall model for wind turbine airfoils'*, 23rd Journal of Fluids and Structures, 2007

[20] – Schepers, J.G., *'IEA Annex XX: Comparison between calculations and measurements on a wind turbine in yaw in the NASA-Ames windtunnel'*, ECN-E-07-072, 2007.

[21] - Snel, H., 'Lecture on Dynamic Stall Modelling', ECN, 7/06/2009

[22] - Øye, S., *'Dynamic stall simulated as time lag of separation'*, Technical report, Department of Fluid

Mechanics,Technical University of Denmark, 1991

[23] - Sheng, W., Galbraith, R. and Coton, F., *'A Modified Dynamic Stall Model for Low Mach Numbers'*, Journal of Solar Energy Engineering, 2008, Vol. 130, pp031013-1/031013-10

[24] – Boorsma,K. and Schepers,G., 'Description of experimental setup MEXICO measurements.pdf', http://mexnext.ecn.nl

[25] - Boorsma,K., 'Experiment Description MEXICO.xls',http://mexnext.ecn.nl

[26] – Pascal, L., '*Analysis of MEXICO Measurements'*, ECN_Wind Memo-09-010, January 2009.

[27] – Micallef, D. , 'Validation of Experimental Data Analysis.pdf', http://mexnext.ecn.nl

[28] - http://mexnext.ecn.nl

[29] – Boorsma, K., 'micfile2.xls' , http://mexnext.ecn.nl

[30] – Micallef, D., Kloosterman, M., Sant, T. and van Bussel, G, *'Comparison and Validation of BEM and Free Wake Unsteady Panel Model with the MEXICO Rotor Experiment'*, Proceedings of Euromech 508 Symposium held at the Universidad Politecnica de Madrid 20-22 October 2009

[31] – Schepers, J and Vermeer, L., *'Een Engineering model voor Scheefstand op basis van Windtunnelmetingen'*, ECN-CX--98-070

[32] – Micallef, D., Kloosterman, M., Ferreira, C., Sant, T. and van Bussel, G., *'Validating BEM, Direct and Inverse Free Wake Models with the MEXICO Experiment'*, December 2009, http://mexnext.ecn.nl,

[33] – Shen,W., Mikkelsen, R. and Sørensen, J., *'Tip Loss Correction for Wind Turbine Computations'*, Wind Energy 2005; 8:457-475

[34] – Fung, Y.C., *'An Introduction to the Theory of Aeroelasticity'*, Dover Phoenix Editions, 1993, pp407

[35] – Leishman, J., Beddoes, T., *'A generalised model for airfoil unsteady aerodynamic behaviour and dynamic stall using the indicial method'*, 42nd Annual Forum of the American Helicopter Society, Washington D.C., June 1986

[36] – Hoerner,S. and Borst,H.,*'Fluid Dynamic Lift'*, Hoerner Fluid Dynamics, 1985

[37] – ESDU, *'The low-speed stalling characteristics of aerodynamically smooth airfoils'*, ESDU TR66034, 1966

[38] – Timmer, W. and van Rooij, R., *'Some aspects of high angle-of-attack flow on airfoils for wind turbine application'*, European Wind Energy Conference and Exhibition, Copenhagen, July 2001

[39] – Mert, M., *'Optimization of Semi-Empirical Parameters in the FFA-Beddoes Dynamic Stall Model',* FFA TN 1999-37

[40] - http://wind.nrel.gov/OSU_data/data/

[41] – Breton,S., Coton,F. & Moe,G., '*A study on Rotational Effects and Different Stall Delay Models Using a Prescribed Wake Vortex Scheme and NREL Phase VI Experiment Data'*, Wind Energy 2008;11:459-482

[42] – Chaviaropoulos, P., & Hansen, M., *'Investigating three-dimensional and rotational effects on wind turbine blades by means of a quasi-3D Navier-Stokes solver'*,Journal of Fluids Engineering 2000; **122**:330-336.

[43] – Brederode,V., *'Fundamentos de Aerodinâmica Incompressível'*, Edição de Autor, IST, 1997

[44] - Schreck, S., Robinson, M., Hand, M. and Simms, D., *'Blade Dynamic Stall Kinematics for a Horizontal Axis Wind Turbine in Yawed Conditions'*, Journal of Solar Energy Engineering, 2001, Vol. 123, pp272/281

Appendices

Appendix A: Complete BEM code

```
%%%%%%   BEM code, with Empirical model for the axial induced velocities in
yaw, including the 3D corrections %%

addpath BL


close all
clear all

%input quantities on geometric conditions

Rt=2.25; %[m]
Rh=0.21; %[m]
omega=424.4*2*pi/60; %[rad/s]
U_inf=24; %[m/s]
density=1.225; %[kg/m3]
B=3;
N=8;
angular_increment=10;
pitch=-2.3; % in degrees
yaw=30;     % in degrees
tolerance = 0.0005;
k_visc=15.1e-6;
Nrev=3 ; % number of revolutions considered

DS=1;  % flag to activate the Dynamic Stall model
C3D=1; % flag to activate the 3D correction of the force coefficients
CTL=1; % flag to activate the Tip loss correction

% derived quantities

lbd=Rt*omega/(U_inf*cos(yaw*pi/180));
dt=angular_increment/(omega*180/pi);

%Derived quantities
element_length=(Rt-Rh)/N;
r=Rh+(Rt-Rh)/(2*N):element_length:Rt; % the actual radius of each element
section
r_real_mat=[r r r];                   % for the 3 blades
r_frac=(r-Rh)/(Rt-Rh);                % fraction of the tip radius
r_mat=[r_frac r_frac r_frac];         % for 3 blades, i.e. relative radius from
```

```
the hub
r_frac_real=(r)/(Rt);                  % actual fraction of the tip radius
r_mat_real=[r_frac_real r_frac_real r_frac_real]; % for 3 blades
span_MEX_a=[0.25 0.35 0.6 0.82 0.92]; % spanwise positions of the MEXICO,
divided by Rt

x_positions_for_interp=[0.21 0.23 0.235 0.3 0.45 0.675 0.9 1.025 1.125 1.225
1.35 1.475 1.575 1.675 1.8 2.025 2.165 2.193 2.222 2.25];
c_points=[0.195 0.195 0.09 0.09 0.24 0.207 0.178 0.166 0.158 0.15 0.142 0.134
0.129 0.123 0.116 0.102 0.092 0.082 0.056 0.011];
c=interp1(x_positions_for_interp,c_points,r,'cubic');
c_mat=[c c c];
c_MEX=interp1(x_positions_for_interp,c_points,span_MEX_a*Rt,'cubic');

twist_points=[16.4 16.4 16.4 16.4 16.4 12.1 8.3 7.1 6.1 5.5 4.8 4 3.7 3.2 2.6
1.5 0.7 0.469 0.231 0];
twist=interp1(x_positions_for_interp,twist_points,r,'cubic');
twist_mat=[twist twist twist];

ReMEX=(sqrt((omega*(span_MEX_a*(Rt))).*(omega*(span_MEX_a*(Rt)))+
(U_inf*cos(yaw*pi/180))^2)).*c_MEX/k_visc;



%%% setting up the azimuth angle, because it is a constant matrix

for j=1:1:1+Nrev*(360/angular_increment)
    for i=1:1:B*N
        az(i,j)=(j-1)*angular_increment;
        if i>N
            az(i,j)=120+(j-1)*angular_increment;
        end
        if i>2*N
            az(i,j)=240+(j-1)*angular_increment;
        end
        while az(i,j)>360
            az(i,j)=az(i,j)-360;
        end
    end
end


% initializing variables for the BL model
% these are the initial values that describe the state
variables=zeros(1,B*N,14);
variables(1,:,6)=1.2; %Cn
variables(1,:,5)=1;   % f parameter
variables(1,:,9)=1;   % f' parameter



%%% we iterate for the average axial induced velocity
```

```
for j=1:1:1+Nrev*(360/angular_increment)

    if j==1 % in the first iteration the value of the axial induction factor is
assumed
        a0_av=0.6-0.02*U_inf*cos(yaw*pi/180);  % from normal values
        a_av=a0_av*0.99;
        count_jota=0;
    else     % if it is not the first time instant, we simply take the
induction factor from the previous iteration
        a0_av=a(j-1);
        a_av=0.99*a(j-1);
    end

    if rem(j,16)==0 % to keep track of the iteration
        count_jota=j
    end


    while abs(a0_av-a_av)>tolerance

        for i=1:1:B*N

            Vax(i)=emp_model2(U_inf,yaw,a_av,r_mat(i),az(i,j));  % axial
velocity, from the empirical model
            Vtg(i)=r_real_mat(i)*omega-
U_inf*sin(yaw*pi/180)*cos(az(i,j)*pi/180); % tangential velocity, including
skewed inflow
            phi(i)=(180/pi)*atan(Vax(i)/Vtg(i));

            if Vax(i)<0 % these lines are included to prevent the iteration
from diverging at higher yaw errors
               phi(i)=0;
            end
            if Vtg(i)<0
                phi(i)=90;
            end

            alpha(i,j)=phi(i)-twist_mat(i)-pitch;

            Vtot(i)=sqrt(Vax(i)^2+Vtg(i)^2);

            %%%%% to compute the Cl,Cd we must choose the airfoil section %%%%

            airfoil_type_v(i)=2; % the transition between airfoils is measured
with tip radius fraction, from
            if r_mat(i)<0.4485   % the hub
                airfoil_type_v(i)=1;
            end
            if r_mat(i)>0.6691
                airfoil_type_v(i)=3;
            end
```

```
            airfoil_type=airfoil_type_v(i);

            %% getting the critical normal force coefficient
            Cn1(i)=getCnCrit(airfoil_type,r_mat(i),c_mat(i),twist_mat(i)
+pitch);

            %%% using 2D aerodynamic coefficients

            if airfoil_type==1
                twodimadd=DUW;
            elseif airfoil_type==2
                twodimadd=RISO;
            else
                twodimadd=NACA;
            end

            Cl_mat(i)=interp1(twodimadd(:,1),twodimadd(:,2),alpha(i,j),'cubic',
'extrap');
            Cd_mat(i)=interp1(twodimadd(:,1),twodimadd(:,3),alpha(i,j),'cubic',
'extrap');

            %%%

            %%% to compute the 3 dimensional aerodynamic coefficients

            if C3D==1

                Cl_mat(i)=get3DCl(airfoil_type,r_mat(i),c_mat(i),alpha(i,j));
                Cd_mat(i)=get3DCd(airfoil_type,r_mat(i),c_mat(i),twist_mat(i)
+pitch,alpha(i,j));
            end

            Cn_mat(i)=Cl_mat(i)*cos(alpha(i,j)*pi/180)+Cd_mat(i)*sin(alpha(i,j)
*pi/180); % computation of force normal to the airfoil


            %%% the dynamic stall is introduced

            if DS==1;
                if j>1
                    intermediate=BLnew(alpha(i,j),alpha(i,j-
1),Vtot(i),dt,c_mat(i),Cn1(i),airfoil_type,variables(j-
1,i,:),r_mat(i),twist_mat(i)+pitch);
                    Cn_mat(i)=intermediate(14);
                    for index=1:1:length(intermediate)
                        variables(j,i,index)=intermediate(index);
                    end
                end
            end
            Ctg_mat(i)=Cl_mat(i)*sin(alpha(i,j)*pi/180)-
Cd_mat(i)*cos(alpha(i,j)*pi/180); % computation of the forcel tang to the
airfoil
```

```
            %%% including the tip loss, from Shen et al., applied in the
            %%% normal and tangential coefficients

            if CTL==1;
                Cn_mat(i)=TipCorrection(Cn_mat(i),lbd,B,phi(i),Rt,r_mat_real(i)
);
                Ctg_mat(i)=TipCorrection(Ctg_mat(i),lbd,B,phi(i),Rt,r_mat_real(
i));
            end


            %the momentum balance is done with the corrected load
            %coefficients

            %Cx_mat(i)=Cl_mat(i)*cos(phi(i)*pi/180)+Cd_mat(i)*sin(phi(i)*pi/180
); % computation of force perpend to rotor plane

            Cx_mat(i)=Cn_mat(i)*cos((phi(i)-
alpha(i,j))*pi/180)+Cd_mat(i)*sin((phi(i)-alpha(i,j))*pi/180); % computation of
force perpend to rotor plane

            T_mat(i)=Cx_mat(i)*0.5*density*(Vax(i)^2+Vtg(i)^2)*c_mat(i)*element
_length;
            Nf_mat(i)=Cn_mat(i)*0.5*density*(Vax(i)^2+Vtg(i)^2)*c_mat(i)*elemen
t_length;
            Tf_mat(i)=Ctg_mat(i)*0.5*density*(Vax(i)^2+Vtg(i)^2)*c_mat(i)*eleme
nt_length;

        end

        T(j)=sum(T_mat);                % here we sum the contribution of all
the blades to the axial force
        Ct(j)=T(j)/(pi*(Rt^2)*0.5*density*(U_inf*cos(yaw*pi/180))^2);


        if Ct(j)>0.8889                 % we obtain 'a' from Ct, using the
Glauert correction for
            roots_a=roots([3 -5 4 -Ct(j)]);  % turbulent wake state
            a(j)=1;
            for r=1:1:3
                if abs(roots_a(r))<a(j)
                    a(j)=abs(roots_a(r));
                end
            end
        else
            a(j)=(1-(1-Ct(j))^0.5)/2; % otherwise
        end


        a0_av=a_av;                     % update the average induction factor
        a_av=0.9999*a_av+0.0001*a(j);
```

```
    end

    for k=1:1:length(span_MEX_a)      % interpolation of the forces at the
MEXICO span positions
        NfBEM(j,k)=(1/element_length)*interp1(r_mat_real(1:N),Nf_mat(1:N),span_
MEX_a(k),'cubic');
        CnBEM(j,k)=interp1(r_mat_real(1:N),Cn_mat(1:N),span_MEX_a(k),'cubic');
        if j>1
        %CnBEM2(j,k)=interp1(r_mat(1:N),Cn_mat2(1:N),span_MEX_a(k),'cubic');
        end
        TfBEM(j,k)=(1/element_length)*interp1(r_mat_real(1:N),Tf_mat(1:N),span_
MEX_a(k),'cubic');
        CtgBEM(j,k)=interp1(r_mat_real(1:N),Ctg_mat(1:N),span_MEX_a(k),'cubic')
;
        alphaMEX(j,k)=interp1(r_mat_real(1:N),alpha(1:N,j),span_MEX_a(k),'cubic
');
    end

end
%
span=1; % we choose the span to plot

grid on
hold on
axis ([0 360 -0.1 (max(CnBEM(:,span))+0.5)])
plot(az(1,1:1+360/angular_increment),CnBEM(((Nrev-
1)/Nrev)*length(CnBEM(:,1)):end,span),'r');

surf(CnBEM(((Nrev-1)/(Nrev))*length(CnBEM(:,1)):end,:));
```

Appendix B - DS model main code

```
%%% this function computes the normal force coefficient using the BL dynamic
stall
%%% model for a given aoa history

function [variables]=
BLnew(alfa,alfa_old,V,dt,chord,Cn1,airfoil,variables,radius,t_pitch)


%derived quantity
delta_s=V*dt/(chord/2); % semichords travelled in each time step

% steady data
[cn_alfa, alfa_t, f_t, cn0] = steady_t_e_sep(airfoil,chord,radius,t_pitch);
save f_coeff cn_alfa alfa_t f_t cn0

pachacha=[alfa_t f_t];

% variables needed from previous condition

X_old=variables(1);
Y_old=variables(2);
Dl_old=variables(3);
Df_old=variables(4);
f_prime_old=variables(5);
cn_old=variables(6);
cn_prime_old=variables(7);
tv=variables(8);
f_double_prime_old=variables(9);
cnv_old=variables(10);
cv_old=variables(11);
delta_alfa_old=variables(12);
D_imp_old=variables(13);



% if flag==1 % on the first time instant initial values are assigned
%     [X_old Y_old Dl_old Df_old f_prime_old cn_old cn_prime_old tv
f_double_prime_old cnv_old cnv cv_old delta_alfa_old
D_imp_old]=inicio1(cn_alfa,alpha_mean);
% else
%     load cenas1 % loading the values calculated in the previous iteration
% end

% geometry
c = chord; % chord length [m]

% Attached flow constants
```

```
%
A1 = 0.3;
A2 = 0.7;
b1 = 0.14;
b2 = 0.53;

etha = 0.95;   % recovery factor
cn_1 = Cn1;  % critical value for the leading edge pressure

% time-constants
Tp = 1.5; % peak pressure - cn lag
Tf = 5.0; % boundary layer - peak pressure lag
Tv =6.0; % vortex decay constant
Tv1 = 5.0; % trailing edge position, in semichords

delta_alfa=alfa-alfa_old;

[alfa_e, cn, cc, X_old, Y_old, D_imp_old,cn_i,cnc]=unsteady_attached(V, c,
alfa, dt, X_old, Y_old, alfa_old, A1, A2, b1, b2,
cn_alfa,cn0,delta_alfa,delta_alfa_old,D_imp_old);
[alfa_f, cn_prime, cn_f, cc_f, f_double_prime, Dl_old, Df_old,
f_prime_old,cn_old]=unst_t_e_sep(Dl_old, Df_old, f_prime_old, cn, cn_old, dt,
Tp, Tf, V, c, cn_alfa, alfa_e, etha, tv, Tv1,delta_s,cn0,cn_i);
[tv, f_double_prime_old]=leading_edge_sep(cn_prime, f_double_prime,
f_double_prime_old, cn_1, dt, tv, V, c);
[cnv,cnv_old,cv_old]=vortex_lift(cnc, dt, Tv, V, c, f_double_prime, cnv_old,
cv_old, tv, Tv1,delta_s);

delta_alfa_old=delta_alfa; % updating of the variable

cn_tot = cn_f + cnv;

save cenas1 X_old Y_old Dl_old Df_old f_prime_old cn_old cn_prime_old tv
f_double_prime_old cnv_old cv_old delta_alfa_old D_imp_old


variables=[X_old Y_old Dl_old Df_old f_prime_old cn_old cn_prime_old tv
f_double_prime_old cnv_old cv_old delta_alfa_old D_imp_old cn_tot cn cn_i cnc
cn_f];


end
```

Appendix C - Results obtained at other data points and spanwise stations

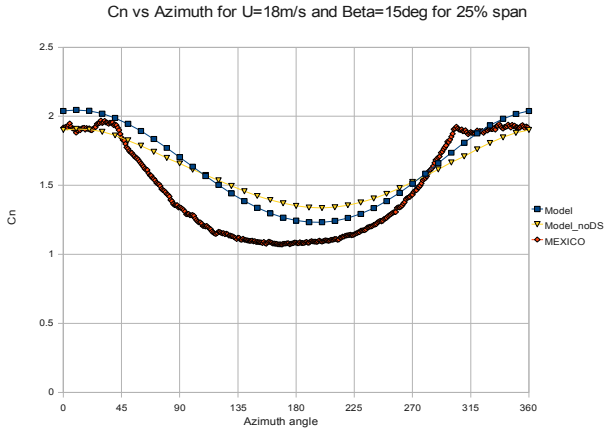

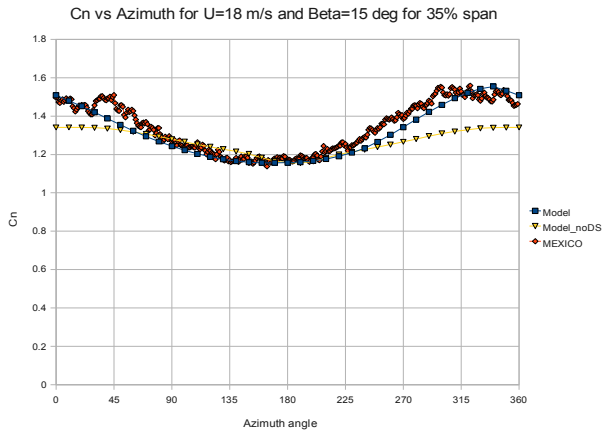

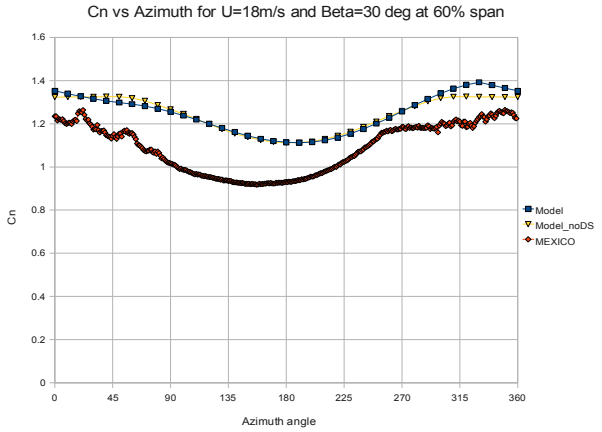

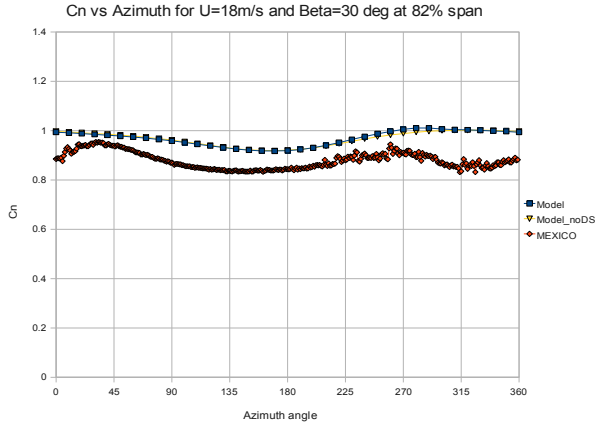

Appendix D - Results of validation cases of the 2D BL DS model

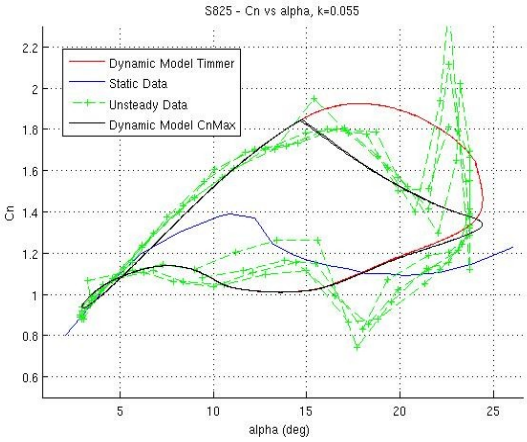

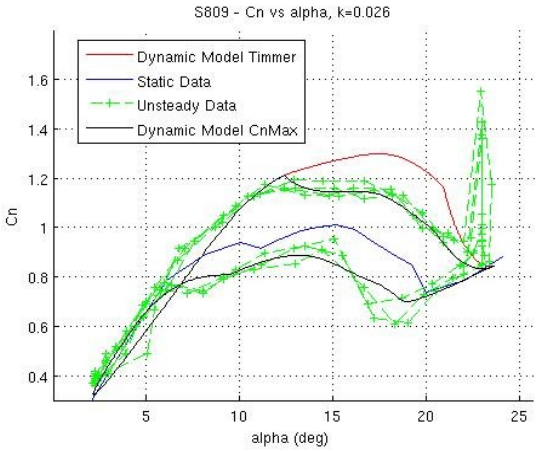

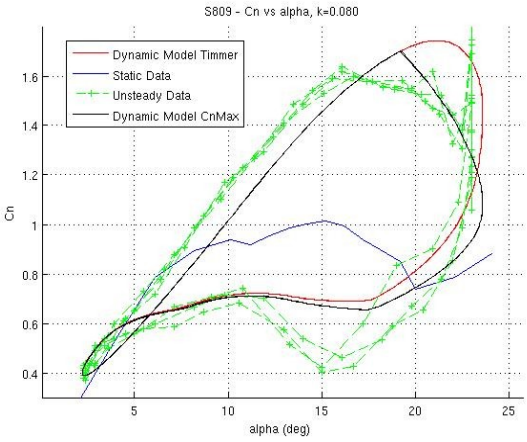

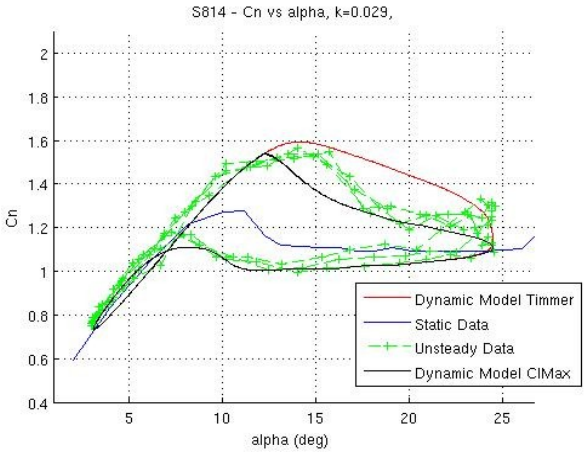

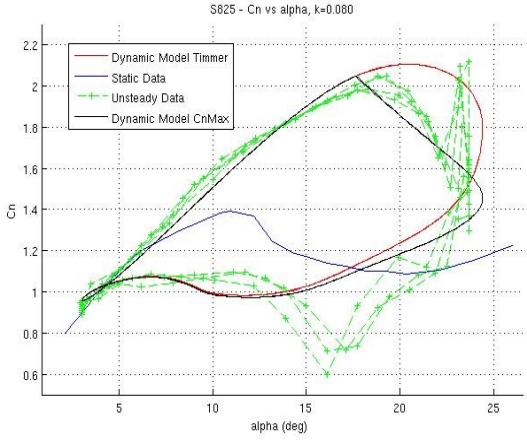

Appendix E - Convergence of BEM code including the DS model

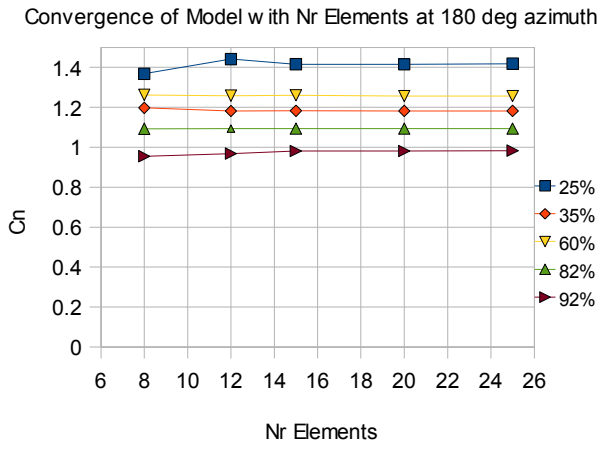

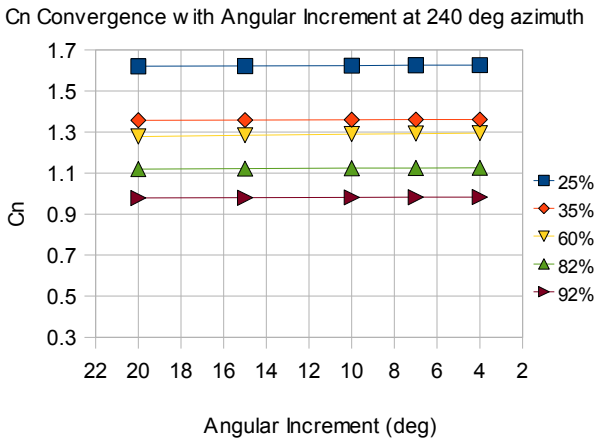

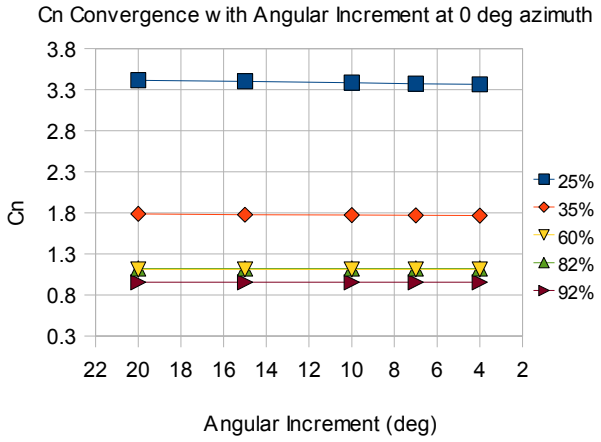

Appendix F - MEXICO Cp distributions at the 35% spanwise station

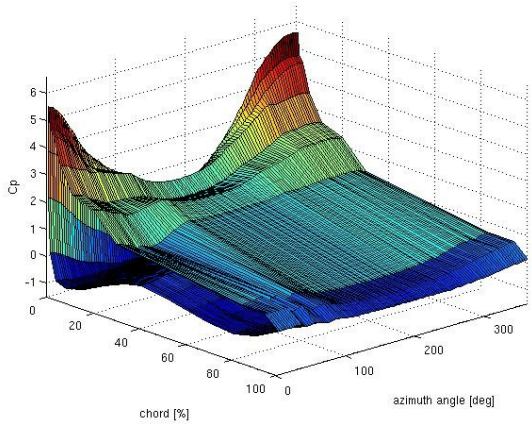

Cp variation at data point 152

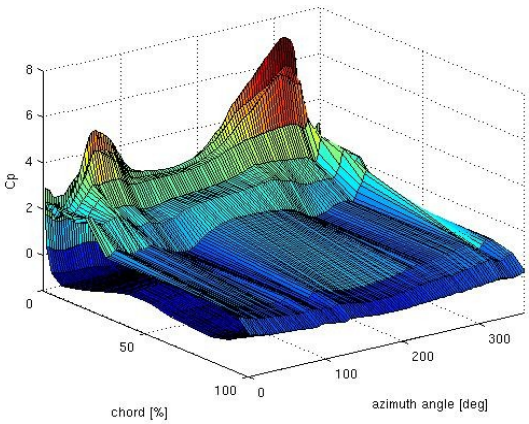

Cp variation at data point 153

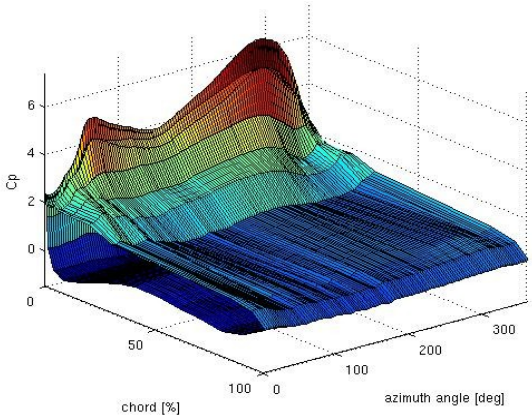

Cp variation at data point 160

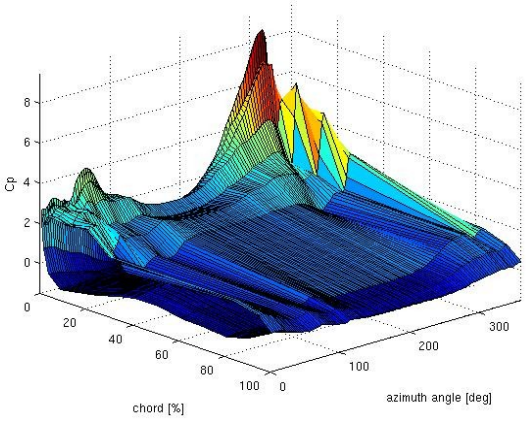

Cp variation at data point 167

Appendix G - DS model results at very high reduced frequencies